UNIVERSIDAD DE JAÉN

ESCUELA POLITÉCNICA SUPERIOR DE LINARES
DEPARTAMENTO DE INGENIERÍA DE TELECOMUNICACIÓN

TESIS DOCTORAL

DEVELOPMENT OF SIGNAL PROCESSING METHODS USING GROUND-PENETRATING RADAR TO EVALUATE THE QUALITY OF STONE MATERIALS

PRESENTADA POR:
VIOLETA MONTIEL ZAFRA

DIRIGIDA POR:
DR. D. NICOLÁS RUIZ REYES
DR. D. FRANCISCO JESÚS CAÑADAS QUESADA

JAÉN, 16 DE JUNIO DE 2017

ISBN 978-84-9159-120-7

This work was carried out under the supervision of

Dr. Nicolás Ruiz Reyes
Telecommunication Engineering Department
Higher Polytechnic School of Linares
University of Jaén

Dr. Francisco Jesús Cañadas Quesada
Telecommunication Engineering Department
Higher Polytechnic School of Linares
University of Jaén

A mi familia, en especial
a mi hermana Azahara
por su apoyo incondicional

Acknowledgements

This Thesis has been supported by Andalusian Business, Science and Innovation Council under Project P11-TIC-7278, being Nicolás Ruiz Reyes the main researcher of the project.

This dissertation would not have been possible without the guidance and help of several individuals who contributed and extended their valuable assistance. First of all, I would like to thank to Dr. Nicolás Ruiz Reyes for giving me the opportunity to take part in this project, his generosity and support and for sharing his knowledge and experience. I sincerely thank Dr. Francisco Jesús Cañadas Quesada for his technical guidance on signal processing and encouragement when required. I also thank him for his constructive suggestions when reviewing the articles and this thesis. I wish to express my special gratitude to Dr. Pedro Vera Candeas for the patience, time and expertise contributed to the enhancement of this dissertation. During these years, we held stimulating debates, which were a great source of inspiration to me.

I am also grateful to the members of the team of the project, specially to Dr. Javier Rey Arrans and Dr. Julián Martínez López for his encouragement and interest during my research. I would like to show my gratitude to the Telecommunication Engineering Department, for facilitating the access to its resources and infrastructures and for the support. Special thanks to Pedro Aguilar Aguilar for his kindness and his technical support when required. Also I thank Rocío Pérez de Prado and Julio Carabias Orti for sharing with me my first steps in teaching.

I would like to express my sincere thanks to my colleagues of the office Pablo, Francisco, Diego, Casto, Unai and Javi for making the everyday life enjoyable. I deeply thank Antonio for his continuous support and help during the final steps of this Thesis.

Finally, I would like to express my gratitude to Dr. Luigi Zanzi from the Politécnico di Milano for offer me an opportunity to work with his research group.

Thank you.

Violeta Montiel Zafra
June 2017

Agradecimientos

Esta Tesis ha sido posible gracias a la beca asociada al Proyecto de Excelencia de la Junta de Andalucía P11-TIC-7278, siendo el Dr. Nicolás Ruiz Reyes el investigador principal del proyecto.

Este trabajo no habría sido posible sin la guía y ayuda de varias personas que han contribuido a confeccionarlo y mejorarlo. Primero, quisiera agradecer al Dr. Nicolás Ruiz Reyes por darme la oportunidad de formar parte de este proyecto, por su generosidad y apoyo y por compartir su conocimiento y experiencia conmigo. Agradezco sinceramente al Dr. Francisco Jesús Cañadas Quesada por su conocimiento técnico en procesado de señal y su apoyo siempre que lo he necesitado. Le agradezco también sus sugerencias constructivas revisando los artículos y esta Tesis. Quisiera expresar mi agradecimiento más sincero al Dr. Pedro Vera Candeas por su paciencia, tiempo y experiencia que han contribuido más que significativamente a la mejora de este trabajo. Durante estos años hemos mantenido debates muy estimulantes que han sido una gran fuente de inspiración para mí.

Gracias también a los miembros del equipo del proyecto, especialmente al Dr. Javier Rey Arrans y al Dr. Julián Martínez López por su especial apoyo e interés durante mi investigación. Quisiera mostrar mi agradecimiento al Departamento de Ingeniería de Telecomunicación por facilitarme el acceso a sus recursos e infraestructuras y por el apoyo constante. Gracias a Pedro Aguilar Aguilar por su amabilidad y apoyo técnico cuando lo he necesitado. También quisiera agradecer a la Dra. Rocío Pérez de Prado y al Dr. Julio Carabias Orti por compartir conmigo mis primeros pasos en la docencia.

Quisiera expresar mis gracias más sinceras a mis compañeros de la sala Pablo, Francisco, Diego, Casto, Unai y Javi por hacer cada día de trabajo un día entretenido y divertido. Agradecer profundamente a Antonio por su apoyo continuo y su ayuda durante los últimos pasos de la consecución de

esta Tesis.

Finalmente, quisiera expresar mi agradecimiento al Dr. Luigi Zanzi del Politécnico de Milán por ofrecerme la oportunidad de trabajar en su grupo de investigación.

Gracias.

Violeta Montiel Zafra
Junio 2017

Abstract

In the last decades, quality control in natural stone materials has become a critical task to evaluate correctly the density of the discontinuities, to facilitate the exploitation, to minimize extraction and transport costs, to improve the cutting process, etc. Most of the anisotropies in stone materials come from their non-homogeneity, which can be classified as cavities, fractures, microfractures, karstification, etc.

Non-destructive evaluation (NDE) is a novel procedure used in Science and Technology industry to test material properties without causing any damage. In particular, Ground-Penetrating Radar (GPR) is a high resolution geophysical method which is originally designed to investigate the subsurface of the earth. Under the convenient conditions, this technique can provide accurate information of the nature of buried objects. Moreover, this technology has been employed to analyse the internal structure of ornamental rocks with promising results.

In this thesis, a set of novel signal processing methods applied to GPR are proposed. These methods are mainly focused on providing a more useful GPR information for the user in order to improve the evaluation and characterization of the internal state of a stone material. Specifically, the global system developed has three main contributions: characterisation of stone materials, detection and classification of defects and removal of the typical noise active in GPR images.

First of all, it is necessary to evaluate and characterize stone materials using GPR. Thus, a technique which highlights the defects inside the stone materials, both quarries and extracted blocks, is designed. For this purpose, a deconvolution method which has not yet been used in GPR images to our best knowledge is employed. Then, the defects are clearly emphasized and the probability of detection is increased. Besides, the stratification and mica

schist contents of massifs can be located. The proposed method is evaluated using different GPR antennas applied to real data. It is proved that GPR is a suitable tool for the diagnosis of stone materials that has been widely used in the field of non-destructive evaluation and testing applied to the extraction or cutting process in the stone industry.

Secondly, a novel GPR signal processing method is developed which automatically detects defects. Besides, it establishes a classification of such defects according to its spatial orientation (horizontal, vertical or diagonal). Moreover, 3D maps have been designed for showing more clearly the defects. This algorithm employs a deconvolution technique trained with a synthetic database, which search for possible spatial orientation defects. This method has been evaluated using synthetic and real databases, with promising results. Then, it can be used for determining the internal quality of a stone block. Besides, the classification of fractures can be useful for the cutting process of the extracted blocks, since during this process vertical and diagonal fractures are critical for the breaking of the slabs and the cutting speed can be adjusted accordingly.

Thirdly, we propose a novel, efficient and fast technique to remove background noise present in GPR images. This noise reduces the resolution of these images and masks possible anisotropies inside the evaluated material. This method is based on exploiting the repetitive pattern shown by the horizontal noise in the direction of the movement of the antenna. It has been trained using synthetic GPR profiles, and it has been evaluated with synthetic and real data. The novel technique outperforms other classic background noise removal methods.

Summarizing, the proposed methods can be considered useful and interesting to be applied in the stone industry because they can improve different processes such as, evaluation of the internal quality of stone blocks, reduction of cutting and transport costs or minimization of the amount of waste products.

Keywords: Ground-Penetrating Radar, GPR, Non-destructive Evaluation, NDE, Non-destructive Testing, NDT, Processing, Deconvolution, Migration, SI-PLCA, Background, Horizontal noise, non-neighboring.

Resumen

En las últimas décadas, la calidad de control en materiales pétreos se ha convertido en una tarea crítica, de forma que se hace necesario evaluar correctamente la densidad de las discontinuidades, para facilitar su explotación, para minimizar costes de extracción y de logística, para mejorar el proceso de corte, etc. La mayoría de anisotropías en piedra parten de su inhomogeneidad, que pueden ser clasificadas como cavidades, fracturas, microfracturas, karstificación, etc.

La Evaluación No Destructiva es un procedimiento novedoso en la industria de la Ciencia y Tecnología para testear las propiedades de un material sin causar daño en él. En particular, el Georradar es una técnica geofísica de alta resolución, originalmente diseñada para investigar la profundidad de la tierra. Bajo unas condiciones determinadas, esta técnica puede ofrecer información de la naturaleza de objetos enterrados. Además, esta tecnología ha sido usada para analizar la estructura interna de piedras ornamentales con resultados prometedores.

En esta Tesis se propone un conjunto de métodos novedosos de procesado de señal aplicados al georradar. Estos métodos están enfocados en ofrecer una información al usuario más útil, para mejorar la evaluación y caracterización del estado interno de un material pétreo. Concretamente, el sistema total desarrollado presenta tres principales contribuciones: caracterización de materiales pétreos, detección y clasificación de defectos y eliminado del ruido normalmente activo en imágenes del georradar.

Primero, es necesario evaluar y caracterizar materiales pétreos usando georradar. Entonces, se ha diseñado una técnica que resalta los defectos dentro de materiales pétreos, tanto canteras como bloques extraídos. Para este propósito se usa un método de deconvolución, que no ha sido aún usado en imágenes de georradar para nuestro conocimiento. Entonces, los defectos

se enfatizan claramente y la probabilidad de detección aumenta. Además, la estratificación y los micaesquistos pueden ser claramente localizados. El método propuesto se evalúa usando diferentes antenas aplicadas a datos reales. Se ha probado que el georradar es una herramienta realmente útil para la diagnosis de materiales pétreos que ha sido ampliamente usado en el campo de la evaluación no destructiva aplicada a la extracción o al proceso de corte en la industria de la piedra.

Posteriormente, un método novedoso de procesado de señal ha sido diseñado, que automáticamente detecta defectos. Además, establece una clasificación de los defectos de acuerdo a su orientación espacial (horizontal, vertical o diagonal). También se han diseñado unos mapas 3D para mostrar más claramente los defectos. Este algoritmo usa una técnica de deconvolución que ha sido entrenada con una base de datos sintética, que busca defectos con las posibles orientaciones espaciales. Este método ha sido evaluado usando bases de datos reales y sintéticas, con resultados prometedores. Entonces, este método se puede usar para determinar la calidad interna dde un bloque de piedra. Además, la clasificación de fracturas puede ser útil para el proceso de corte de bloques extraídos, ya que durante dicho proceso las fracturas verticales y diagonales son críticas en la rotura de las tablas extraídas, así que la velocidad de corte puede ser ajustada convenientemente.

Por otra parte, proponemos una técnica novedosa, eficiente y rápida para eliminar el ruido de fondo presente en las imágenes de georradar. Este ruido reduce la resolución en estas imágenes y enmascara las posibles anisotropías dentro del material a evaluar. Este método está basado en la búsqueda de patrones repetitivos típicos en el ruido horizontal en la dirección del movimiento de la antena. Ha sido además entrenado usando perfiles sintéticos de georradar, y ha sido evaluado con datos sintéticos y reales. La técnica supera los resultados de otras técnicas clásicas de eliminado de ruido de fondo.

Para concluir, los métodos propuestos pueden considerarse útiles e interesantes para poder ser aplicados a la industria de la piedra, ya que pueden mejorar diferentes procesos como la evaluación de la calidad interna de bloques de piedra, reducción de costes de corte y transporte y minimizado la cantidad de residuos.

Keywords: Georradar, Evaluación No Destructiva, Procesado, Deconvolución, Migración, SI-PLCA, Fondo, Ruido horizontal.

List of Acronyms

ACC	Accuracy
AGC	Automatic Gain Control
ATS	Average Trace Subtraction
BMS	Background Matrix Subtraction
CMP	Common Mid-Point
DTVM	Directional Total Variation Minimisation
EM	Electromagnetic
EUC	Euclidean Distance
FA	False Alarm
FDTD	Finite-Difference Time-Domain
FFT	Fast Fourier Transform
GPR	Ground-Penetrating Radar
HR	Hit Rate
HT	Hilbert Transform
ICA	Independent Component Analysis
NDE	Non-destructive Evaluation
NDT	Non-destructive Technique
PCA	Principal Component Analysis
PLCA	Probabilistic Latent Component Analysis
RMS	Root Mean Square
RRME	Root Mean Square Error
SI-PLCA	Shift Invariant Probabilistic Latent Component Analysis
SIMCA	SIMulated Correlation Algorithm
SVD	Singular Value Decomposition
SSI	Subsurface Imaging
TV	Total Variation

List of Symbols

Symbol	Units	Definition
$\bar{E}$	$[V/m]$	Electric field strength vector
$\bar{H}$	$[A/m]$	Magnetic field intensity vector
$\bar{D}$	$[C/m^2]$	Electric displacement vector
$\bar{B}$	$[T]$	Magnetic flux density vector
$\bar{J}$	$[A/m^2]$	Electric current density vector
q	$[C/m^3]$	Electric charge density
ϵ	$[F/m]$	Permittivity
μ	$[H/m]$	Permeability
ϵ_r	-	Relative permittivity
μ_r	-	Relative permeability
σ	$[S/m]$	Conductivity
v	$[m/s]$	Velocity of propagation
ω	$[rad/s]$	Angular frequency
β	$[rad/m]$	Phase coefficient
α	$[Neper/m]$	Attenuation coefficient
η	$[\Omega]$	Intrinsic impedance
r	-	Reflection coefficient
ϕ	$[^\circ]$	Angle

Symbol	Units	Definition
d	$[m]$	Distance to the target
t	$[s]$	Two-way travel time to the target
λ	$[m]$	Wavelength
f_c	$[Hz]$	Frequency
R	-	Bandwidth to center frequency ratio
B	$[Hz]$	Bandwidth
Δv	$[m]$	Vertical resolution
Δh	$[m]$	Horizontal resolution
Δx	$[m]$	Sampling interval
v_{rms}	$[m/s]$	RMS velocity
k	$[m^{-1}]$	Temporal wavenumber
k_x	$[m^{-1}]$	Spatial x wavenumber
k_z	$[m^{-1}]$	Spatial z wavenumber

List of Constants

Symbol	Value	Definition
ϵ_0	$8.85x10^{-12}F/m$	Electric permittivity of free space
μ_0	$1.26x10^{-6}H/m$	Magnetic permeability of free space
c	$3x10^{8}m/s$	Speed of light

List of Figures

List of Tables

Contents

List of Included Publications

This thesis is a compound thesis consisting of the following publications, which are preceded by an introductory overview of the research field and a summary of the contributions. The publications will be referred in the text with [P1], [P2] and [P3].

- **[P1] Rey J., Martínez J., Vera P., Ruiz N., Cañadas F., Montiel V.**, "Ground-penetrating radar method used for the characterisation of ornamental stone quarries", in *Construction and Building Materials*, vol. 77, pp. 439-447, 2015.

- **[P2] Montiel V., Cañadas F., Vera P., Ruiz N., Rey J., Martínez J.**, "Detection and classification of internal defects in limestone blocks based on a deconvolution technique with SI-PLCA applied to GPR signals", *Research in Nondestructive Evaluation*. Status: under review.

- **[P3] Montiel V., Cañadas F., Vera P., Ruiz N., Rey J., Martínez J.**, "A novel method to remove GPR background noise based on the similarity of non-neighboring regions", *Journal of Applied Geophysics*. Status: under review.

Chapter 1

Introduction

1.1 Context and motivation

Subsurface imaging (SSI) is the imaging of an object buried below the surface of a medium [94]. Non-destructive Testing (NDT) or Non-Destructive Evaluation (NDE) is the process of inspecting, testing, or evaluating materials in order to search for discontinuities, or differences in certain characteristics without destroying the functionality of the component under study. In this manner, the material has not suffered any damage when the test is completed. Destructive testing implies damages suffered by the material. As a result, several samples are often necessary to inspect in order to determine its properties.

Like other type of products, quality control in natural stone is a critical task, since evaluation of massive stone quality and homogeneity could lead to primary waste reduction and improving overall sustainability. [37]. This material can present structural discontinuities, such as fractures, cavities, etc., or studying its layers could be interesting. Determining the structure of a quarry could reduce extraction costs, since it could facilitate the planning of the advance of its exploitation, minimizing the use of explosives. Besides, the size or position of the extracted standard-sized blocks could be adequately selected. In addition, the early detection of internal defects of stone blocks can reduce cutting and transport costs, amount of waste products and can optimize the production of slabs or smaller blocks. Specifically, the probability of occurrence of a defect inside an extracted block is really high in limestones. Based on information, a cutting protocol of the

extracted blocks can be established, or to consolidate the block by means of resins (or other components) or maybe to establish injection points, thus improving the performance of the entire process.

Nowadays, NDT, as an upcoming technology, is used in several processes in order to assess the quality of product or to estimate the properties of stone. Several authors have proposed numerous NDT methods in order to evaluate stone products. Bodare [15] separated the NDT methods into two major categories, depending on the type of wave: seismic and electric methods.

On the one hand, seismic methods can be divided, in turn, as ultrasonic and impact-echo methods. First, ultrasonic methods have been widely used to analyse the internal structure of stone products [17] [121] [71] [21] [93] [96] [14]. While it is true that the resulting resolution is really high and both big and small defects with excellent precision can be detected, ultrasonic techniques use sophisticated procedures (each transducer should be positioned along the material), and real measurements require rather time consuming [72]. Then, impact-echo methods have been widely used mainly to analyze concrete structures, but it has been also used to evaluate stone [92]. The main drawback of this method is that it can only provide information about the general quality of the material, without detailing the number, size, shape or spatial orientation of the possible defects.

On the other hand, electric methods are divided into radar, resistive and electromagnetic methods. Radar techniques are undoubtedly the most used for these tests. In particular, Ground-Penetrating Radar (GPR), as a suitable diagnosis tool, is widely employed in the investigation of stone properties and fracturing [104] [40] [105] [57] [58] [82] [26] [34] [47] [8] [43] [116], due to the fact that the dielectric properties of stone materials allows this technique to perform well.

GPR has become one of the most common used NDT methods for the assessment of natural stone. Under favorable conditions, this technique allows not only accurately identify targets, but characterize the environment, discriminate materials, detect inhomogeneities, etc., without any damage of the medium to test. In addition to its resolution (both lateral and vertical), GPR becomes a promising prospecting method due to its quick and easy operation. GPR antennas do not need to be in contact with the surface of the material to test, which enable a simple measure, and with an affordable cost. Finally, the reflection amplitudes and the travel times are compacted into

a high-resolution image, known as radargram, where the different objects are shown. In geological applications, this technique is used to analyse the structure of the stone at depths of 30-60 m. In other high resolution applications, high frequency antennas are able to offer a better noise control, as well as to provide a high quality image, with a depth of 5-10 m.

However, the challenge of GPR processing is to get an accurate radargram analysis method, since this technique presents some limitations which need to be solved: the obtained radargrams are not a realistic picture of the medium and its interpretation is not intuitive. Then, the final user must interpret the image based on his own experience, so the analysis is subjective. The beamwidth of the antenna, the wavelength of the radiation and the dimensions of the target will cause that the final image will not correspond to reality. In general, most stone materials present high attenuation, which makes the penetration of the waves more difficult. Moreover, the signal to clutter ratio of the radargram is the key to target detection [23], where clutter is a typical background noise present in almost all of these radargrams. In this context, the noise energy of the clutter masks the real targets existing inside the stone. Currently, there are several background removal methods as will be detailed in Chapter 2, in Section 2.3.2 whose main goal is to remove this type of noise.

The main objective of any signal processing method applied to GPR is to provide a reconstructed radargram which can be easily interpreted by the user, removing any possible noise and also to automatically classify the target. Moreover, 3D GPR maps can contribute to a better understanding of the internal structure of a stone product, showing the depth, shape and the spatial localization of the detected fractures. There are different commercial programs (e.g. ReflexW [87]) which correlate the radargrams and offer a 3D vision of a material, but a classification of the defects cannot be done to our best knowledge. Several authors have also investigated in 3D GPR modelling as will be shown later (in Section 2.4 of the Chapter 2).

This thesis applies GPR to evaluate the quality of stone materials. In particular, different signal processing methods are proposed to enhance the probability of detection of fractures, to automatically detect and classify the defects and to remove background noise. Then, the three methods compose a general system to remove noise, to detect and to classify fractures in stone materials.

For the first purpose, GPR is used to probe the texture of different types of stone materials, as well as to detect anisotropies. A deconvolution technique is used for searching for activations of a GPR typical pulse in the radargram. Then, it enhances the energy related to the encountered defects inside real GPR data, increasing the probability of detection of the anisotropies. The performance is evaluated over quarries and extracted blocks, proving that GPR together with a deconvolution technique is useful for the evaluation of the general quality of stone materials as well as for the determination of their texture and composition.

Subsequently, GPR is applied to automatically detect and classify fractures according to their spatial orientations. Then, a deconvolution technique is used with a synthetic training database, which is composed of possible defects with vertical, horizontal and diagonal orientations. Later, the proposed method is objectively evaluated using a synthetic testing database. Besides, real blocks data is used for the creation of 3D maps, one per orientation, which show their internal structure. The proposed method outperforms the detection and classification performance compared to state-of-art methods. Besides, the results have shown that GPR can be used as a classification tool for discarding blocks directly at the quarry or to optimize the cutting process.

Finally, a background removal method is developed in order to remove the horizontal noise, which often masks the real anisotropies present in the GPR image. Since this noise is propagated in the direction of the movement of the GPR antenna, the method identifies the repeating regions to remove them. There is an optimization procedure using a synthetic training database. Then, experimental results over a test database, with synthetic and real data, prove that the proposed method obtains better results compared to the classic background removal techniques.

The database is also composed with synthetic and real data and the results are compared with classic background methods, obtaining promising results.

1.2 Scope of the Thesis

This thesis is focused on developing novel signal processing methods using GPR data in order to evaluate the quality of stone materials by means of

characterization, detection and classification of defects detected. In this Thesis, we explore two application scenarios: stone quarries and extracted blocks.

The main objectives of the present thesis are:

- To characterize stone quarries, by using a deconvolution technique in order to probe the texture and to enhance the anisotropies detection.
- To create a method for detecting fractures and a 2D and 3D models for classification fractures according to their spatial orientation in stone blocks, by using a deconvolution technique.
- To remove GPR background noise present in most radargrams, which is based on the non-local similarity of 2D regions over the distance in order to identify repetitive regions of the same depth.

1.3 Scientific Contributions

Main scientific contributions of this thesis comprise:

[P1] Ground-penetrating radar method used for the characterisation of ornamental stone quarries

As mentioned before, evaluating the extension and the potential of a stone quarry can produce remarkable benefits in terms of reducing costs, risks and environmental impact as well as increasing the productivity. Then, this paper uses GPR to predict the texture and the anisotropies in stone for ornamental use. The proposed scheme consists of two stages: data acquisition and processing and radargram enhancement. First, data is acquired in a real limestone quarry and in commercial extracted blocks using different GPR antennas and a variety of pre-processing tools is applied. Then, the anisotropies are highlighted using a Shift-Invariant Probabilistic Latent Component Analysis (SI-PLCA). This algorithm separates the anisotropies from noise, by searching for activations of the typical GPR pulse across the two dimensions of the image. GPR is founded as a suitable tool for the diagnosis of stone materials and SI-PLCA is a good approach to highlight the relevant information. Besides, in this work it is observed that the GPR response is better for horizontal than for vertical fractures, so this result suggests that a classification of defects can be desirable.

[P2] Detection and classification of internal defects in limestone blocks based on a deconvolution technique with SI-PLCA applied to GPR signals

It is well known that analysing the structure of stone blocks before performing the cutting process can improve the productivity. In this work, a novel approach to improve the detection and to classify defects according to their spatial orientation in damaged stone blocks is presented. For this purpose, SI-PLCA algorithm is used. First, the method is based on training fractures with a variety of orientations, such as vertical, horizontal an diagonals. Thus, SI-PLCA provides information about the activation of each pattern at each position of the block. Then, it is possible to know the number of defects in a block, as well as its importance and spatial orientation. Besides, a 3D map provides information about the fractures for each orientation pattern. Then, this type of classification is a novel result to our best knowledge in GPR signal processing. For the experiments, a synthetic and a real databases are employed and the results are objectively compared with state-of-art methods, with promising detection and classification results. Besides, the novel method obtains a suitable detection when the fracture is vertical, which is the most critical spatial orientation during the cutting process, as indicated in [P1] objectives.

[P3] A novel method to remove GPR background noise based on the similarity of non-neighboring regions

One of the major challenges in the research related to GPR image is the improvement of its quality. Due to interferences of the horizontal background noise, the resolution quality is decreased and the true anisotropies cannot be detected. In order to remove this type of noise, this study proposes a novel, fast and robust background removal. It is based on observing the repetitive pattern shown by the noise in the direction of the movement of the antenna. Then, for a certain region, other repetitive ones at the same depth are searched. The method assumes that regions composed of horizontal background noise show higher similarity between them, whereas regions mainly composed of anisotropies present lower similarity. Besides, an optimization procedure for the selection of the parameters of the method needs to be applied. Experimental results show a promising performance compared to classic background removal techniques.

1.4 Thesis structure

The rest of the thesis is organized as follows. Chapter 2 presents the state of art of the use of GPR for quality control purposes. Chapter 3 includes the methodology, where the stone specimens and the experimental work are described. Databases and metrics for evaluation are included here. Chapter 4 is focused on the evaluation of the proposed methods for characterisation of stone quarries, for detection and classification of defects in stone blocks, and finally for removal of background noise active in GPR data. Besides, future work is included. Finally, the articles published during this thesis are included in the appendix.

Chapter 2

State of the art

The potential of GPR for analysing the internal structure of stone materials has been addressed. As explained in Chapter 1, GPR is widely used for prospecting stone materials due to its dielectric properties, both quarries and, less frequently, for extracted blocks.

In order to obtain a fast evaluation of the material, it is often that classic activities use the raw GPR radargrams without any post-processing over quarries or blocks. In some studies, it is common to simply use pre-processing methods, which are present in most commercial software ([87] [84]). However, in other recent cases, several signal processing algorithms are applied to the GPR radargrams in order to remove noise and to reconstruct the real image. Besides, numerous specific signal processing methods have been created, in order to improve the detection of discontinuities or even to do a classification of the detected targets. Moreover, new algorithms have been developed for removing the background noise present in most radargrams. Finally, 3D visualization methods have been developed by several authors, since this type of reconstruction clearly shows the internal spatial structure of a material.

In this Chapter, the state of the art related to GPR is presented. First, it is necessary to explain briefly the mathematical and physical background that supports GPR, including the propagation of the waves trough the material, the well-known Maxwell equations and the electromagnetic (EM) parameters of the medium. The equations related to each operating parameter of the GPR system are presented. Besides, the EM properties of the stone material are detailed. Finally, a complete review of the most referenced and

recent published techniques are presented, separating the works related to the use of GPR over stone materials (both quarries and blocks), the general signal processing which most authors apply to their data and the 3D reconstruction methods.

2.1 Physical and mathematical background related to EM waves and GPR

In this section, a brief review of the GPR fundamentals is presented. For this purpose, it is necessary to explain how the emitted waves are propagated trough the material. Moreover, as this Thesis is focused on stone materials, a review of the properties of these materials is depicted. To conclude this Chapter, an overview of the GPR principles is presented.

2.1.1 Propagation of electromagnetic waves in dielectric materials

The propagation of the EM waves along a medium was originally described by Maxwell [62], which summarized the work of prior researches in a more compacted form (equations 2.1 and 2.2).

$$\bar{\nabla} \times \bar{E} = -\frac{\partial \bar{B}}{\partial t} \tag{2.1}$$

$$\bar{\nabla} \times \bar{H} = \bar{J} + \frac{\partial \bar{D}}{\partial t} \tag{2.2}$$

$$\bar{\nabla} \bullet \bar{D} = q \tag{2.3}$$

$$\bar{\nabla} \bullet \bar{B} = 0 \tag{2.4}$$

where $\bar{E}$ is the electric field strength vector, $\bar{H}$ is the magnetic field intensity vector, $\bar{D}$ is electric displacement vector, $\bar{B}$ is the magnetic flux density vector, $\bar{J}$ is the electric current density vector and finally q is the electric charge density.

These four relations represent the properties and the dependence between electric and magnetic fields. In other words, the Maxwell's equations

establish that electric currents generate magnetic fields, and vice versa. Then, these relations introduce the property parameters (or EM parameters) of permittivity ϵ, magnetic permeability μ and conductivity σ. The material's response to EM fields are described by the following constitutive relationships (equations 2.5 2.6 2.7).

$$\bar{J} = \tilde{\sigma}\bar{E} \tag{2.5}$$

$$\bar{D} = \tilde{\epsilon}\bar{E} \tag{2.6}$$

$$\bar{B} = \tilde{\mu}\bar{H} \tag{2.7}$$

where $\tilde{\sigma}$, $\tilde{\epsilon}$ and $\tilde{\mu}$ are tensor quantities related to conductivity, permittivity and magnetic permeability respectively.

Permittivity describes the capability of a material to store and release energy from an electric field. The higher the permittivity parameter, the more energy is absorbed by the medium or, in other words, the slower the wave travels through the medium. The relative permittivity is defined by $\epsilon_r = \epsilon/\epsilon_0$, where ϵ_0 is the electric permittivity of free space. The wet materials will slow down the EM wave, since the water presence causes that the permittivity increases.

Magnetic permeability indicates the capability of a material to store and release energy from a magnetic field. It is related to the magnetic polarization of a material. Then, when a material present a high permeability, it will interfere with the magnetic part of the wave. The relative permeability of a material is $\mu_r = \mu/\mu_0$, where μ_0 is the magnetic permeability of free space. For non-ferromagnetic materials it is assumed that this value is equal to 1.

Conductivity is the ability of a material to conduct electric current. This parameter affects to the penetration of the waves through the medium. Materials which present high conductivity conduct the electric part of the wave, and so the attenuation increases. Then, a low conductivity would be desirable. When the material is resistive (low conductivity), such as dry sand, ice or dry concrete, the wave stays intact longer and continues travelling through the material. However, if the material is conductive, such as salt water or wet concrete, the EM wave is absorbed.

Table 2.1 shows the conductivity and relative permittivity of several materials. As can be observed, wet materials present higher relative permittivity than dry mediums (and so the wave reduces its velocity). Besides, the conductivity is lower in materials such as dry concretes, limestones and sands, but it is higher in materials such as sea water.

Material	**Conductivity**	**Relative Permittivity**
Air	0	1
Asphalt dry	$10^{-2} : 10^{-1}$	2–4
Asphalt wet	$10^{-3} : 10^{-1}$	6–12
Clay dry	$10^{-1} : 10^{-0}$	2–6
Clay wet	$10^{-1} : 10^{-0}$	5–40
Coal dry	$10^{-3} : 10^{-2}$	3.5
Coal wet	$10^{-3} : 10^{-1}$	8
Concrete dry	$10^{-3} : 10^{-2}$	4–10
Concrete wet	$10^{-2} : 10^{-1}$	10–20
Freshwater	$10^{-6} : 10^{-2}$	81
Freshwater ice	$10^{-4} : 10^{-3}$	4
Granite dry	$10^{-8} : 10^{-6}$	5
Granite wet	$10^{-3} : 10^{-2}$	7
Limestone dry	$10^{-8} : 10^{-6}$	7
Limestone wet	$10^{-2} : 10^{-1}$	8
Permafrost	$10^{-5} : 10^{-2}$	4–8
Rock salt dry	$10^{-4} : 10^{-2}$	4–7
Sand dry	$10^{-7} : 10^{-3}$	2–6
Sand wet	$10^{-3} : 10^{-2}$	10–30
Sandstone dry	$10^{-6} : 10^{-5}$	2–5
Sandstone wet	$10^{-4} : 10^{-2}$	5–10
Sea water	10^{2}	81
Sea water ice	$10^{-2} : 10^{-1}$	4–8
Shale dry	$10^{-3} : 10^{-2}$	4–9
Shale saturated	$10^{-3} : 10^{-1}$	9–16
Snow firm	$10^{-6} : 10^{-5}$	6–12
Soil clay dry	$10^{-2} : 10^{-1}$	4–10
Soil clay wet	$10^{-3} : 10^{-0}$	10–30
Soil loamy dry	$10^{-4} : 10^{-3}$	4–10
Soil loamy wet	$10^{-2} : 10^{-1}$	10–30
Soil sandy dry	$10^{-4} : 10^{-2}$	4–10
Soil sandy wet	$10^{-2} : 10^{-1}$	10–30

Table 2.1: Typical range of EM parameters of various materials measured at 100 MHz [23].

In most common of applications, the key parameters are the permittivity and the conductivity, whereas variations of the permeability parameter are not significant [45]. Besides, as GPR operates best with low electrical loss materials, if conductivity is equal to 0, the working depth will be greater.

The dielectric properties are critical GPR parameters, since they will

control the velocity of the EM waves through the material, and they will affect the horizontal and vertical resolutions. Then, a GPR survey can correctly be planned knowing these values previously mentioned, as well as the resulting radargrams will be properly interpreted.

The velocity of propagation v of the EM wave is defined by equation 2.8.

$$v = \frac{\omega}{\beta} \tag{2.8}$$

where ω is the angular frequency ($\omega = 2\pi f$) and β is the phase parameter.

The attenuation coefficient α is expressed in equation 2.9, whereas the phase parameter β is defined according to the equation 2.10.

$$\alpha = \omega\sqrt{\mu\epsilon}\left(\frac{1}{2}\left[\sqrt{1+\left(\frac{\sigma}{\omega\epsilon}\right)^{1/2}}\right]-1\right)^{1/2} \tag{2.9}$$

$$\beta = \omega\sqrt{\mu\epsilon}\left(\frac{1}{2}\left[\sqrt{1+\left(\frac{\sigma}{\omega\epsilon}\right)^{1/2}}\right]+1\right)^{1/2} \tag{2.10}$$

There is a simplifying assumption which is made for low-loss materials [45]. In this case, the attenuation is approximated as the equation 2.11 and the velocity of propagation can be approximated as the equation 2.12.

$$\alpha = \frac{\sigma}{2}\sqrt{\frac{\mu}{\epsilon}} \tag{2.11}$$

$$v = \frac{c}{\sqrt{\epsilon_r}} \tag{2.12}$$

where c is the velocity of light in free space, defined by equation 2.13.

$$c = \frac{1}{\sqrt{\mu_0\epsilon_0}} \tag{2.13}$$

Then, the conductivity has a large effect on attenuation [54] and the velocity is dependent on the permittivity of the material.

Finally, the intrinsic impedance η is defined according to equation 2.14.

$$\eta = \sqrt{\frac{\mu}{\epsilon}} \tag{2.14}$$

Besides, when an EM wave arrives at an interface between two materials

with different intrinsic impedance, part of the wave is reflected back to the source, whereas the other part is refracted [56]. The reflected signal is described by the reflection coefficient r (2.16).

$$r = \frac{\eta_2 - \eta_1}{\eta_2 + \eta_1} \tag{2.15}$$

where η_1 and η_2 are the impedances of the mediums 1 and 2 respectively. Then, when the material is low-lossy, the expression can be simplified as described in equation 2.16.

$$r = \frac{\sqrt{\epsilon_{r2}} - \sqrt{\epsilon_{r1}}}{\sqrt{\epsilon_{r2}} + \sqrt{\epsilon_{r1}}} \tag{2.16}$$

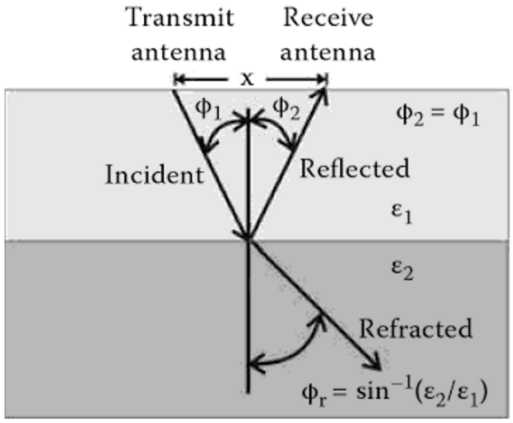

Figure 2.1: Incident, reflected and refracted waves from a layer with contrasting permittivities [4]

A typical example can be observed in Fig. 2.1. Then, when $\epsilon_{r2} > \epsilon_{r1}$, r has a positive value. This situation can be found in an air-filled void existing in a dielectric material [23]. Besides, the relationship between the velocities and the angles of the waves can be expressed in equation 2.17.

$$\frac{v_1}{v_2} = \frac{sin(\phi_1)}{sin(\phi_2)} \tag{2.17}$$

These characteristics related to stone products have been investigated by several authors [98] [118] [70] [119] [101] [111]. However, in most practical situations the EM parameters will be unknown, so the determination of these properties remains largely experimental. Besides, stone is a complex

medium which is composed of many materials in varying proportion, so within different types of stone the dielectric parameters will vary [23].

Then, it can be concluded that, for the type of products this Thesis is focused on, the permittivity varies between 7 and 9. In real cases, it is also possible to estimate this value using processing software, by manual fitting an hyperbola.

2.1.2 Ground-Penetrating Radar

GPR is a non-destructive evaluation technique which uses radio waves to inspect dielectric materials (Fig. 2.2).

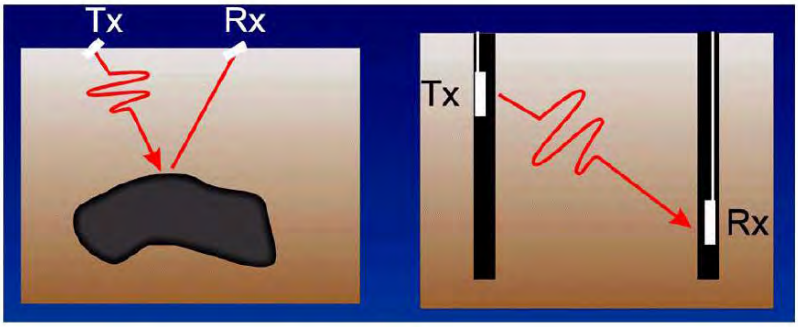

Figure 2.2: GPR basic scheme [6].

Originally, this method was applied to natural geologic materials. However, today it is used extensively for a variety of applications in many fields, such as environmental [79], forensic [25], archaeological investigations [12], building construction [74] [99] [9], landmine detection [39], pipes or cable detection [80], sedimentology [67] and it is able to analyze numerous materials, such as concrete [42], wood [91], rock [124], soil [31], etc.

Basic Principles

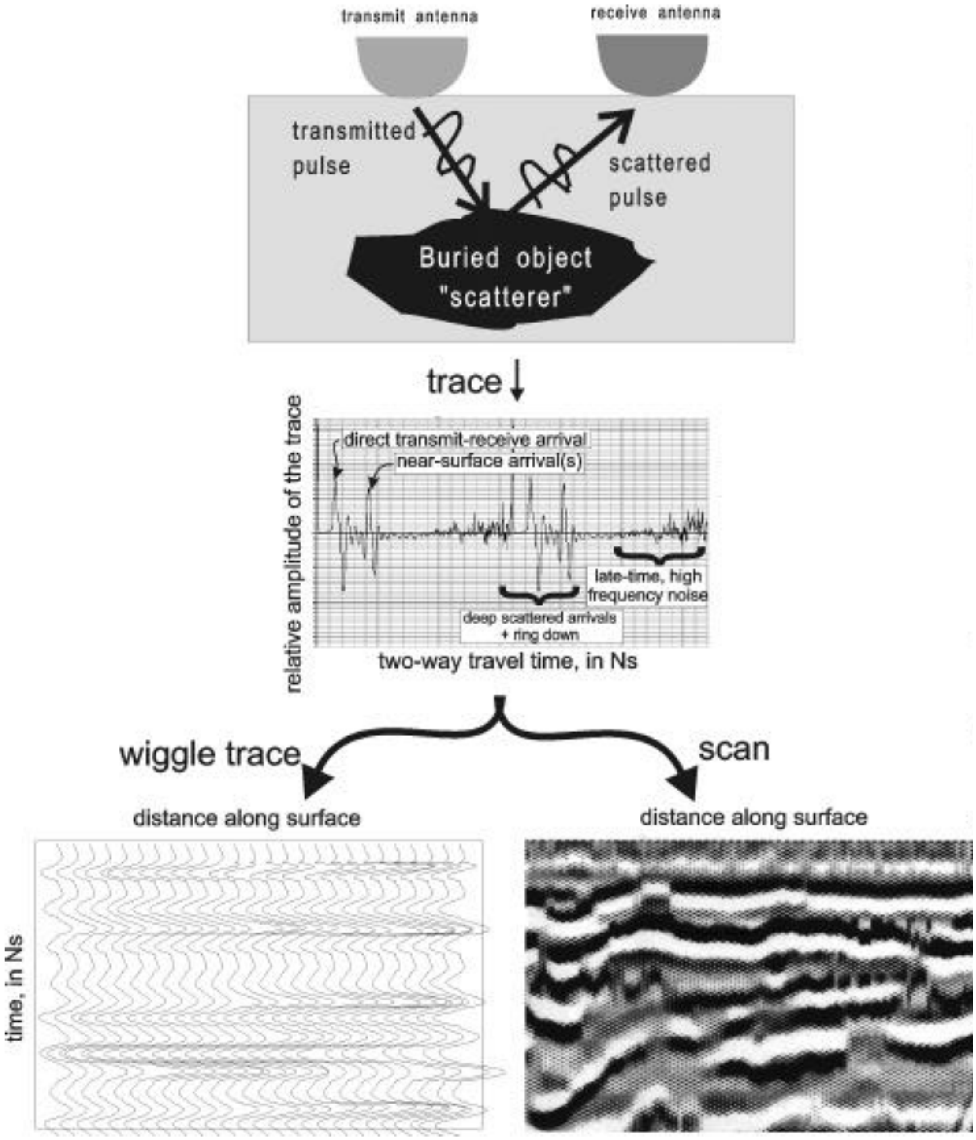

Figure 2.3: GPR typical reflection schematic [22]

The most common use of GPR employs a display unit, that provides a display of the recorded data, a data collection unit and an emitting and a receiver antennas, which are moved along the surface of a material, in order to detect reflections of any type of target. Most commercial GPRs are shielded bistatic radar, that is, they have an emitting and a receiver

antennas. These bistatic antennas can separate its position for common mid-point (CMP) surveys, in order to determine the velocity of the wave through the material. On the other hand, shielded antennas are used to reduce interference from external sources which can produce EM radiation, being more robust than unshielded antennas.

The fundamentals of GPR are based on the study of the propagation of polarized high-frequency EM waves (25 MHz - 4 GHz), while an antenna moves across the surface, emitting short EM pulses. In Fig. 2.3 a basic example of a typical reflection schematic is shown. In the top plot the emitting and the receiving antenna are placed at the top of a material, which is composed of a material and a buried object, and they present different dielectric properties. The EM wave is radiated by the emitting antenna and travels through the medium, with a velocity which is dependent on the permittivity of the material. When the wave hits a medium with different dielectric properties, it is reflected or scattered back to the surface, and then the receiving antenna records it for later interpretation. Besides, part of the wave energy continues to travel downward (refracted wave). The process is repeated until the EM wave is completely attenuated. Moreover, the greater the contrast between the two materials, the stronger the reflected signal. In the middle top of Fig. 2.3, the recorded trace is shown. This signal is known as A-scan or trace, where the only variable is the time, directly related to the depth of the EM wave through the medium. Then, as GPR antenna is moved along the distance, a set of traces constitute a B-scan, also referred as radargram, which is shown in the bottom-right top of Fig. 2.3. This typical image uses different colors to represent the amplitude of each point.

In Fig. 2.4 a whole scans description is exposed, where in the top plot an A-scan is showed, in the middle plot a B-scan or radargram, as a collection of A-scans, is presented, and, finally, in the bottom plot a C-scan is displayed, where the spatial thee-dimensional data can be used to reconstruct a 3D image. Then, A-scan, B-scan and C-scan provide 1D, 2D and 3D data respectively. It is common to work with B-scans, and to apply processing to A-scans.

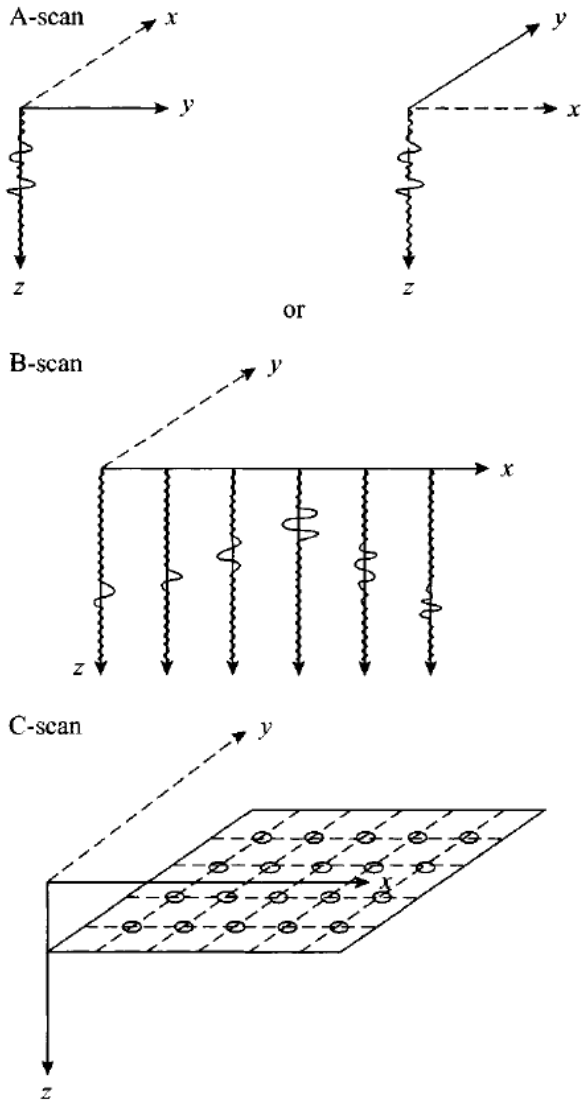

Figure 2.4: Scans description [22]

GPR operating parameters

A GPR survey is planed considering the expected subsurface material properties, the nature and the depth of the targets and possible limitations [125]. Then, the performance of GPR will be dependent of the frequency and the selected operating parameters.

One important factor is the time window, which is the period during which each A-scan is measured by the receiving antenna, and it needs to

be accurately adjusted to penetrate the desired depth, depending on the velocity of the wave through the material.

Moreover, the relationship between the velocity of the wave and the material properties is the fundamental basis of GPR. Since the velocity of two mediums differs when they present different dielectric parameters, when a wave travels through these two materials, the travel times will be different. Knowing the velocity value, for an homogeneus medium, the depth or thickness can be measured from 2.18.

$$d = \frac{vt}{2} \tag{2.18}$$

where t denotes the two-way travel time between the surface and the target and d is the resulting distance to the target. Thus, time window can be approximately adjusted using this relation. However, estimating the velocity of the wave through a real material is not trivial. In most trial situations, the relative permittivity will be unknown and the velocity of propagation needs to be measured in situ [23].

On the other hand, wavelength λ is given by the relation between the velocity of the wave v and the selected frequency as indicated in equation 2.19.

$$\lambda = \frac{v}{f_c} \tag{2.19}$$

where f_c is the nominal frequency.

There is a direct relationship between the frequency of the transmitted wave and the resolution. Besides, there is an inverse relationship between frequency and penetration depth. Then, high frequency antennas are used for searching of small and/or shallow targets, whereas low frequency antennas are employed for detecting big and/or deep targets. Moreover, the medium and the target properties should be taken into account when selecting the transmitted frequency. Table 2.2 summarizes how the GPR parameters and the EM properties affect a GPR survey.

Then, the choice of the nominal frequency f_c is based on the trade-off between desired depth and resolution [24] [89], as well as on the EM properties of the medium. The higher the nominal frequency, the less the wave is able to penetrate the material. Besides, the conductivity, as explained in Section 2.1.1, is proportional to the attenuation. Then, materials which present high

GPR Parameter	Permittivity low high	Conductivity low high	Frequency low high	Remark
Velocity	fast slow			Velocity is high in materials such as dry sand, and slow in water-saturated materials.
Attenuation		low high		Signal attenuation is influenced strongly by electrical conductivity at high frequencies.
Penetration		long short		The lower the attenuation, the greater the penetration distance.
Wavelength			long short	Short wavelengths are normally used for concrete structures; long wavelengths are applied to mapping geological layers.
Resolution			low high	The shorter wavelength, the higher resolution of subsurface targets.

Table 2.2: Relationship between EM parameters, operating parameters and the selected frequency [125].

conductivity suffer a high attenuation, so the penetration decreases.

Moreover, GPR signals are characterized by the bandwidth to centre frequency ratio R (equation 2.20) [45].

$$R = \frac{B}{f_c} \tag{2.20}$$

The goal is to maximize the bandwidth B and minimize f_c. Since $R \approx 1$ in most commercial GPRs, they are usually characterized by the center frequency.

In addition, resolution is a fundamental term which is related to the ability to distinguish two targets from one another [88], as can be seen in Fig. 2.5. The vertical resolution Δv (in depth) is considered as defined in equation 2.21.

$$\Delta v = \lambda/4 \tag{2.21}$$

This resolution is independent on the distance between the antenna and the target in a real world. The lateral resolution Δh (in distance) will be related to the properties of the radar wave, the EM parameters of the medium and the distance between the antenna and the target. Then, it can be calculated as defined in equation 2.22 [45].

$$\Delta h = \sqrt{r\lambda/2} \tag{2.22}$$

where r is the separation between the GPR antenna and the target. Some authors have investigated vertical and horizontal resolution in real cases [78]. Thus, the detection of any target by the GPR will become difficult, if it is very small compared to the wavelength, if it present dielectric properties very similar to the medium or if the distance between the target and the antenna is very small.

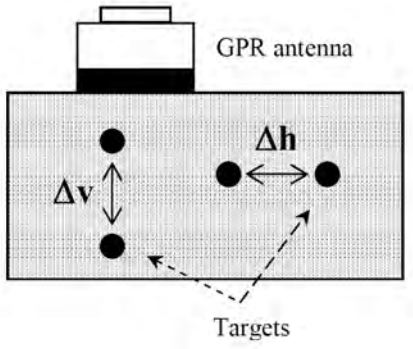

Figure 2.5: Resolution scheme [88].

Besides, data acquisition system should satisfy the Nyquist sampling criteria, in order to avoid aliasing. For a given sinusoid frequency f, the sampling interval (or step size, in distance) Δx must obey $\Delta x \leq v/2f$. It is common to use values that are half as large, so the sampling interval will be $\Delta x \leq v/4f$. For GPR signals with a bandwidth to nominal frequency ratio equal to unity, this is translated to $\Delta x \leq \lambda/3$ [45]. Then, it is recommended to select a value lower than satisfy $\Delta x \leq \lambda/6$. Besides, if the selected sampling interval is very small, it is necessary a slow speed of the movement of the antenna.

Clutter

Clutter is a noise which affects the GPR radargrams and it can be defined as signals that are unrelated to the target but are present in the same time window, with similar spectral properties. The reasons of this noise are diverse and they can be caused by reflections between the emitting antenna and the surface, interferences between the emitting and receiving antenna, which is called as cross-talk or by scattered signals of other objects [23]. This effect is usually presented as horizontal straps and it is common that the target energy of interest is masked by it. In general, clutter noise is

more significant at short range and decreases at longer times. A radargram which presents clutter can be seen in Fig. 2.6, where horizontal straps in the samples 40-60 in depth. This noise presents high energy and masks the real anomalies in the radargram (at a depth of 400 and 600 samples on the right). Moreover, the example presented in Fig. 2.7 clearly shows that the clutter influence increases with increasing frequency.

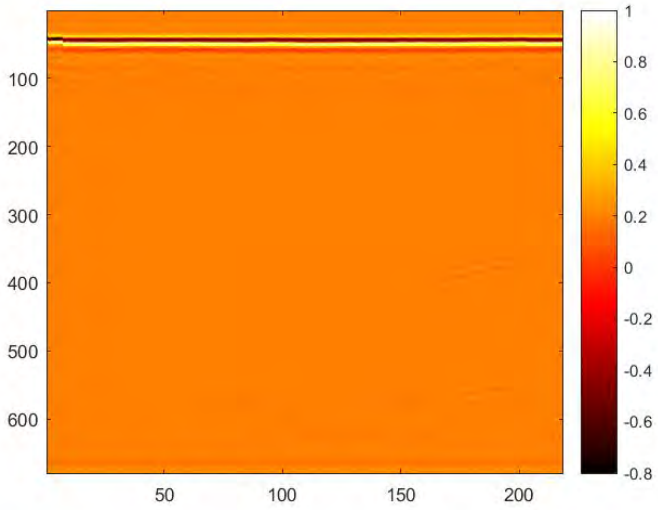

Figure 2.6: Example of a radargram with clutter.

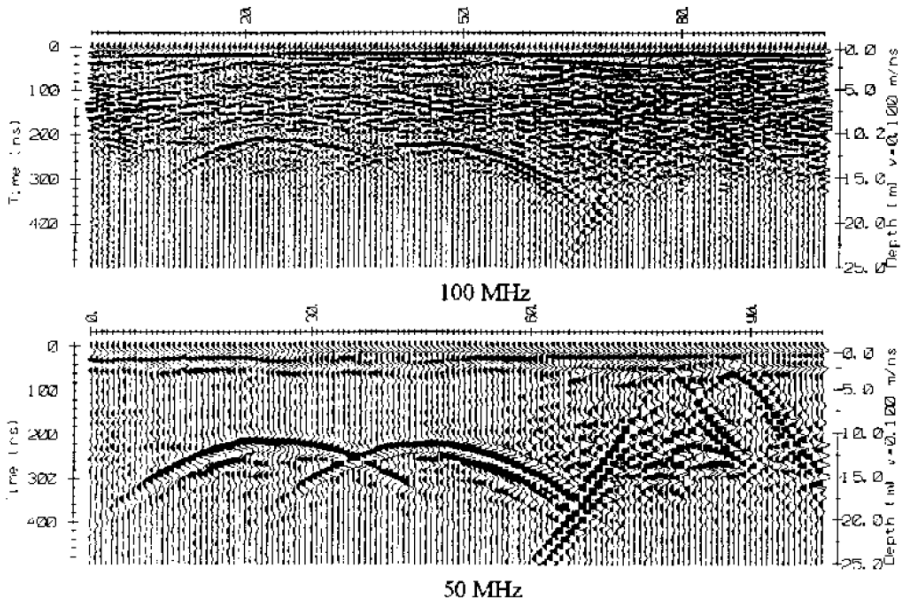

Figure 2.7: Example of the clutter frequency concept. At 100 MHz the clutter is clearly visible, whereas at 50 MHz much of the clutter is suppressed [6].

Methods which suppress the clutter effects are known as Background removal techniques. An exhaustive review of state-of-art background removal methods is presented in the Section 2.3.2 in this Chapter.

Advantages and disadvantages of GPR

The most important advantage of GPR is its non-destructive nature [16]. Moreover, it presents the capability of detecting targets from several centimeters to hundred of meters, with the appropriate antenna and configuration (according to the survey design). Besides, this technique is really fast of using and with low cost, allowing an on-site evaluation of the current situation. The antennas of a GPR do not need to be in contact with the surface of the earth [23]. Finally, it is able to detect many types of materials beneath the subsurface, responding to both metallic and non-metallic objects [22].

However, one important limitation of GPR is that the antenna emits the signal in a 3D cone, so the receiving antenna can record data from reflections which can be originated from anywhere around this cone. Then,

when a reflection is recorded, the radargram is not a picture directly beneath the survey point and this can lead to problems with the interpretation of the depth and shape of the detected targets. Moreover, the performance of GPR is limited to the environment and with some types of material the emitted EM wave is rapidly attenuated. The selection of the operating parameters will be dependent on the material to study and the nature, depth and environment of the target to find. Finally, this technique is really sensitive to unwanted signals caused by the system, other EM transmissions or other factors [16].

2.2 The use of GPR in the stone industry

Determining the internal structure of a quarry can reduce extraction costs as well as improve its exploitation. Besides, once the stone blocks are extracted, the detection of possible defects can reduce transport and cutting costs and can improve the production of slabs. Then, the publications related to this paper [P1], [P2] and [P3] analyse stone quarries and blocks quality. Thus, this section briefly reviews the use of GPR to assess the quality of stone materials, specifically, quarries and stone blocks. Besides, a review of methods to evaluate stone materials is included.

2.2.1 GPR applied to evaluate the quality related to quarries

GPR has been used in numerous works [104] [55] [113] [40] [63] [105] [29] [81] [73] [58] [7] [82] [47] [34] [60] [68] [48] in order to inspect the quality of stone quarries.

Sigurdsson [104] conducted one of the first studies over quarries, performing lithographic characterisations in limestone quarries. Kong and By [55] discussed the advantages of using GPR with several applications, including the analysis of a granite quarry. This work proved the utility of this technique for detecting cracks in stone materials. Tillard and Dubois [113] used GPR for analysing granitic and limestone quarries in order to determine the wave propagation velocity. Besides, the author outlined the utility of this technique for distinguish the depth or thickness of the multiple beds inside the same quarry, in order to detect two kinds of limestone. GPR was also applied by Grandjean and Gourry [40] for detection of fracture zones in a marble quarry in Greece. To carry out this study, the authors employed

frequencies of 900 and 300 MHz, obtaining suitable results and concluding that the resolution and penetration reached with these antennas were reasonably good. Meschede et. al [63] also used GPR with a 300 MHz antenna to investigate a limestone quarry, with promising results. Sigurdsson and Overgaard [105] conducted studies in limestone quarries, where zones and textural variations could be differentiated. Derovert and Abraham [29] combined GPR and seismic imaging to investigate a gypsum quarry using a 500 MHz antenna. Pipan et. al [81] employed GPR for analysing the bedding planes and fractures in limestone in Italy, using antennas of 50, 100, 200 and 250 MHz and applying pre-processing techniques. Moreover, GPR was used by Orlando [73] for doing a semi-quantitative evaluation of massive rock quality. Lualdi and Zanzi [58] developed a method to explore the potential of GPR applied to a limestone quarry in Italy, using antennas of 50 and 250 MHz. The results were compared with the geological structures. This work proved that GPR can be used to evaluate the extension and the potential of a quarry and to prevent extraction activities in non-profitable areas, since the limestone layers are clearly detected (Fig. 2.8). Apel and Dezelic [7] used a 1500 MHz antenna for mapping a quarries, differentiating the dolomite and limestone rocks. In [82] Porsani et. al introduced a method for detecting fractures, joints and massive blocks in an ornamental granite quarry in Brazil using antennas of 25, 50 and 100 MHz were employed. These frequencies are able to distinguish fractures and to localize massive blocks, information which can serve as a guide for planning the advance of the quarry. Kadioglu [47] used the technique for determining changes in layer thickness and fractures or air- or moisture-filled cavities in a marble quarry in Turkey. This study is performed using a 250 MHz antenna. Moreover, Forte et. al [34] applied this technique to perform a general evaluation of limestone characteristics. Luodes [60] established a characterization of different natural stone assessment and their material properties using GPR. This technique is applied to granite, schist, soapstone and marble. The GPR measurements clearly show the fracturing of the rock (Fig. 2.9)). Results indicated the difficulty in detecting vertical and sub-vertical fractures due to their small reflections Nielsen et. al [68] developed a 3D vision of a limestone quarry to illuminate the architecture and growth patterns of carbonate mounds. Finally, Kana et. al [48] employed GPR for analysing a limestone quarry in order to characterize the filling material and the aperture of the

fractures.

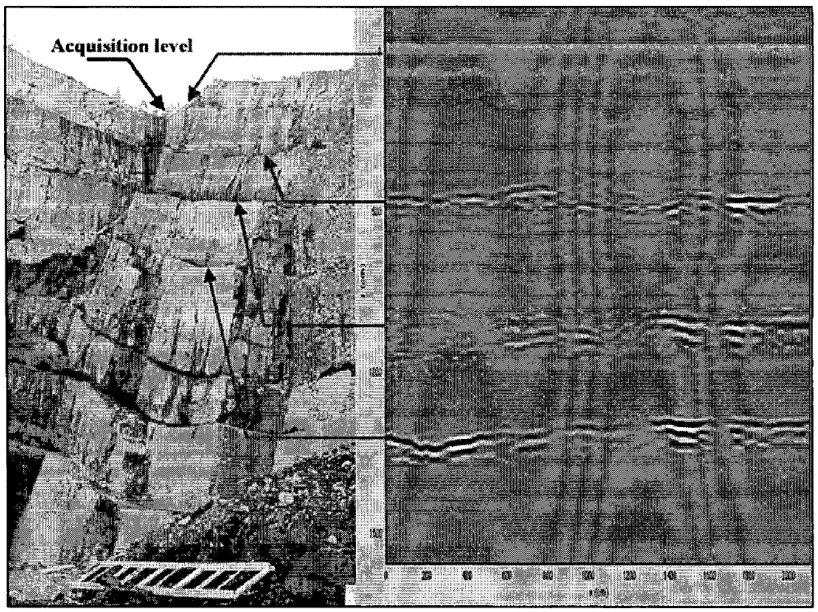

Figure 2.8: The structure of a quarry and a 250 MHz radargram, where the layers are clearly highlighted [58].

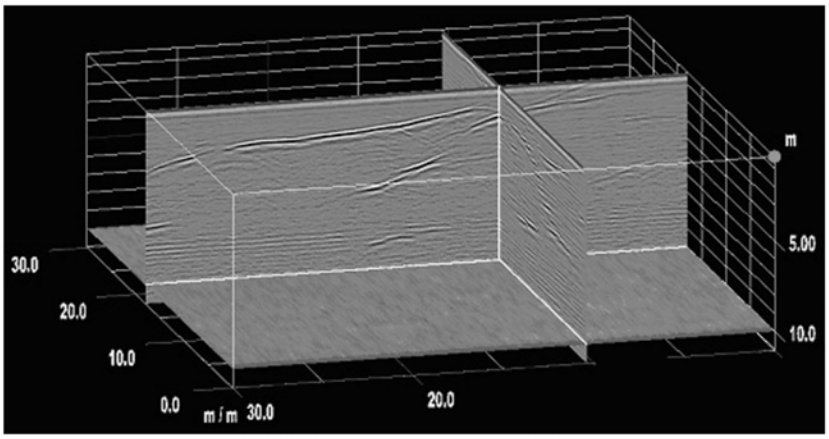

Figure 2.9: A schematic presentation of two GPR radargram which show the propagation of the fractures in a quarry [60].

Summarizing, the previous works suggest that GPR can be an effective and fast tool to evaluate the general quality of a stone quarry, detecting its layers and fractures. Besides, antennas of 100-250 MHz provide a good resolution with the necessary depth.

2.2.2 GPR applied to evaluate the quality related to stone blocks

The use of GPR for analysing the quality of extracted stone blocks is not as extensive as of quarries studies.

In the following, a short revision of GPR studies applied to blocks [58] [95] [8] [10] [11] is presented.

Lualdi and Zanzi [58] developed a method to evaluate the volume of extracted stone blocks and to detect the areas affected by fractures using a 250 MHz antenna. The geometry of the detected fractures can be seen in Fig. 2.10. This work proves the utility of GPR for increasing the productivity and optimizing the cutting of the blocks. Sambuelli [95] used GPR for detecting thin fractures in marble blocks, in order to optimize their cutting, using a 2 GHz antenna. The author analyzed the amplitude and phase of the reflections to differentiate the fracture filling. Arosio et. al [8] established a method of quality control applied to stone blocks, in order to detect internal defects, using a 2 GHz GPR system and employing a simple data processing. Fig. 2.11 shows the utility of GPR for locating fractures inside stone blocks. Finally, Arosio et. al [10] [11] addressed a fracture characterization with GPR, using deterministic deconvolution, applied to small block samples. The fracture parameters which are characterized are related to the thickness and the filling material, by processing the amplitude and phase spectra of the thin bed reflection. The results suggest that GPR can be a fast and effective tool to analyse the fracture parameters.

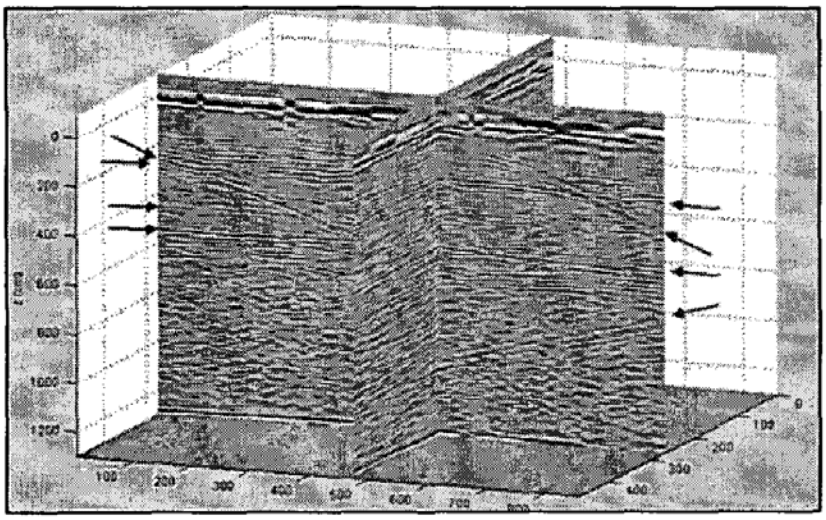

Figure 2.10: Cross sections of a stone block, where the horizontal and dipping fractures are marked by arrows [58].

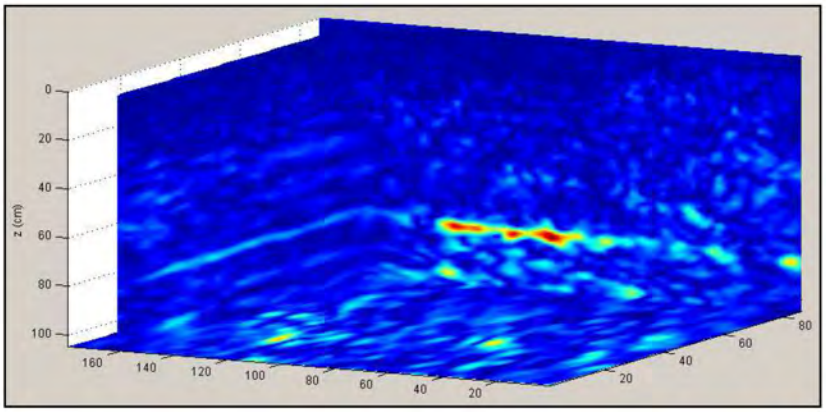

Figure 2.11: 3D map of a thin discontinuity present on a marble block [8].

This short review of works related to the use of GPR applied to block evaluation proves that GPR can be a suitable method to analyze the internal structure of stone blocks. Besides, the selected frequencies can be higher than the antennas employed in the quarry analysis, so the resolution can be improved.

2.2.3 GPR applied to general stone assessment

Hereafter, a brief review of studies conducted by several authors to assess stone materials is presented here.

Toshioka et. al [116] carried out measurements of vertical rock walls in order to design a mapping crack distribution. Roch et. al [90] conducted a study on the assessment of rock-fall hazards using a 100 MHz antenna, proving the potential of GPR for rock analysis. Theune et. al [112] used a 50 MHz GPR antenna for discovering highly fractured rocks. Deparis et. al [27] designed a fracture characterization method of unstable cliffs using a 100 MHz antenna, with a penetration of 25 m. Dorn et. al [32] performed a fracture reconstruction using 100 and 250 MHz GPR antennas applied to a granitic rock aquifer. Longoni et. al [56] designed a method to evaluate the characterization of a fractured rock mass using GPR. The proposed method integrates diverse techniques used to define the rock mass fracture pattern: joint orientation, spacing, and persistence. An example of its performance can be observed in Fig. 2.12. Finally, Forte et. al [35] used a 3D dataset to construct a tool to characterize sediments and rock masses.

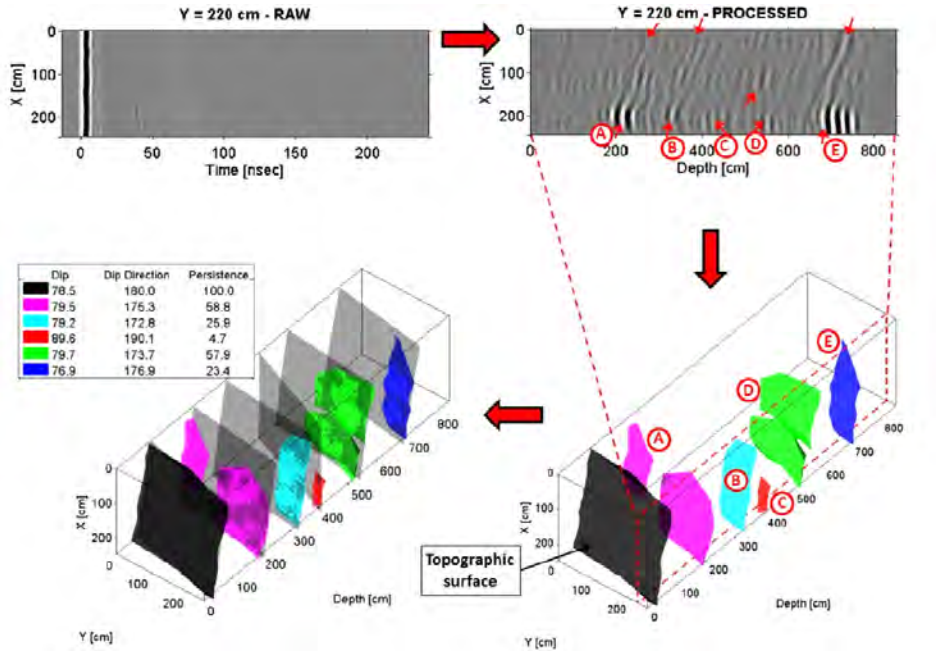

Figure 2.12: Example of the method proposed by Longoni et. al: raw radargram (top left), processed radargram with the discontinuities (top right), interpolated discontinuities (bottom left) and fitting planes (bottom right) [56].

2.3 Signal Processing applied to GPR

The goal of applying signal processing methods to GPR is to achieve a more reliable radargram that provides an user's opinion without ambiguity. As a result, it is compulsory to remove any noise and clutter existing in the radargram. Some processing methods are applied to each A-scan, since each trace can present its own properties that must be treated separately. However, there are other techniques which are used for B-scans or even for C-scans.

2.3.1 Pre-processing

A pre-processing method is a routine which is applied over each trace of the radargram to correct anomalies from the recording. The most common used methods [16] [29] [36] [39] [40] [50] to pre-process a raw radargram (Fig. 2.13.(a)) are described as follows.

- **DC Removal**: this technique consists on deleting the constant component of the trace, in case there is one. Then, the method slides a window from the beginning to the end of the A-scan, subtracting the mean or the median within it from the centre value of such window. This component does not indicate any useful information, so it should be removed. An example is shown in Fig. 2.13.(b).

- **Background Removal**: it is the subtraction of the mean determined in a selected window, in order to remove clutter, which usually blocks up the desired signal. After applying this technique, the real anomalies of the radargram can be detected, as can be observed in Fig. 2.13.(c). In this radargram, the clutter at 25 m of depth is almost completely removed.

- **Gain**: this step is necessary in order to equalize the amplitude of the emitted wave, which suffers a significant attenuation along the medium. Automatic Gain Control (AGC) is usually selected to do this equalization, where, for each position of a running window, the average amplitude is calculated, and then the signal value in the selected point (which is usually the beginning of such window) is divided by this coefficient. Other types of gains include constant gain, exponential gain compensation. In all cases, the selection of the size of the window and the maximum gain allowed are crucial to get the best possible result. A clear example is shown in Fig. 2.13.(d), where it can be observed that the energy at the end of the radargram is now equalized.

- **Filtering**: finally, the unwanted frequencies, due to system or human-induced noise, should be removed. Besides, there are many types of filters, from simple Band-Pass to sophisticated domain and transform filters. It is usually common to use Band-Pass filters, selecting the half part and the double of the nominal frequency as the upper and lower cut-off frequency points respectively. This final step is shown in Fig. 2.13.(e).

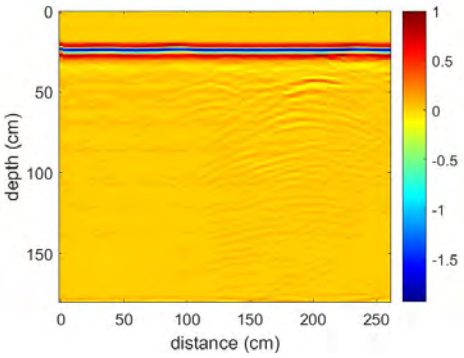

(a) Raw radargram

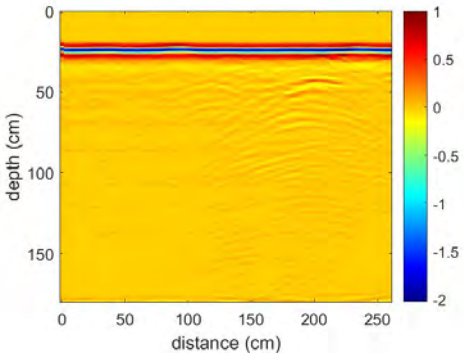

(b) Radargram after applying DC removal

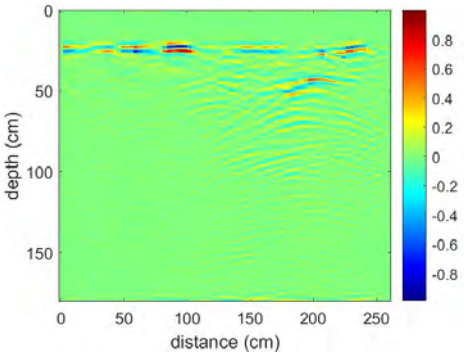

(c) Radargram after applying Background removal

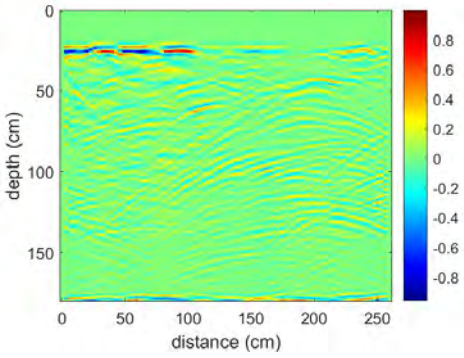

(d) Radargram after applying Gain

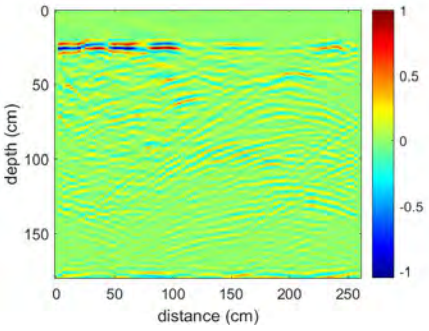

(e) Radargram after applying Filtering

Figure 2.13: An example of a radargram after applying each of the pre-processing methods above mentioned.

2.3.2 Background Removal

Background removal is the procedure of subtracting from the total field the part of clutter (or background noise), which has been introduced in Section 2.1.2.

One of the most reference algorithm to remove the background noise present in the radargrams is the average trace subtraction (ATS) [108] [45] [69]. This method only takes the mean of several traces within a window and removes it from each trace. ATS assumes that this noise is constant. For this reason, it is not robust when evaluating rapid variations of the noise. Then, ATS could degrade the true anisotropies present in the radargram. Besides, other used estimator is the median trace. Moreover, by using a median filter, the algorithm can be made adaptive.

Moreover, Singular Value Decomposition (SVD) is a commonly used background method [19] [16], known algorithm for *diagonalisation* of rectangular matrices. Using this technique decomposed the data into eigenimages and quantify how much a decomposed eigenimage correlates with the original dataset. If the data is severely contaminated by background noise, this noise can be regarded as a component which is the most correlated with the data. However, the components that can be extracted with this technique are always orthogonal, and they cannot be easily interpreted.

A reference technique is the Principal Component Analysis (PCA) [122] [16] [2] [103]. This algorithm can be performed via several approaches, such as eigenvalue decomposition of covariance matrix or SVD. In this case, PCA decomposes measured data into two orthogonal matrices that provide information about the main components present in a dataset. Besides, it provides a third matrix where the diagonal elements indicate the amount of information of each principal component. This decomposition can be done in one dimension (1DPCA) or two dimensions (2DPCA). Problems related to orthogonality have an impact on PCA.

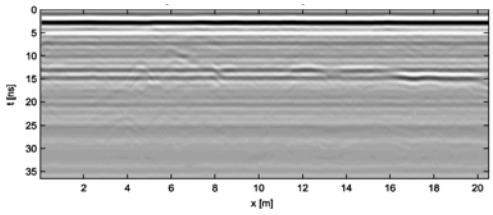

(a) Raw radargram

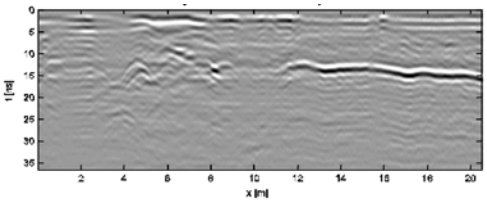

(b) Radargram after applying ATS using mean estimator.

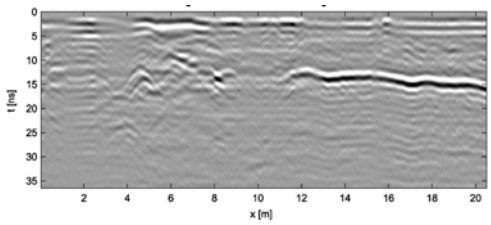

(c) Radargram after applying ATS using median estimator.

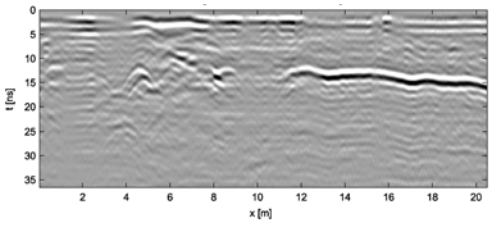

(d) Radargram after applying median filter.

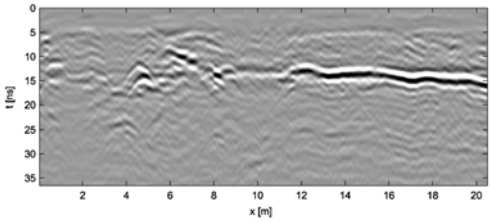

(e) Radargram after applying PCA.

Figure 2.14: An example of a radargram after applying background removal techniques [115].

Fig. 2.14 shows the most used background methods [115], where the comparison based on visual inspection suggests that in this example the more efficient method is PCA.

Other approaches have been developed to improve the removal of the horizontal noise, such as Independent Component Analysis (ICA) [128], filtering [127] [59] [49] [83] [130], likelihood processing [65], deterministic deconvolution [123], wavelet domain [1], [44], parametric system identification [28] and eigenimage processing [51] [50].

Recently, some authors have published novel background removal methods [85] [86]. For instance, a new method was developed by Rashed M. [85] known as Background Matrix Subtraction (BMS). This technique calculates the complete background matrix, with windowing, sample exclusion, weight-

ing and iteration. Specifically, at each depth of a vertical GPR section, it applies a 1D window and calculates an alpha-trimmed mean. Subsequently, it excludes any sample within this window which has a different sign from this mean. The samples are weighted according to their closeness to the alpha-trimmed mean and normalized. Then, this window is slid horizontally and vertically to conform a background noise matrix and the whole process is iterated until all the residuals are removed.

Besides, a Directional Total Variation Minimisation (DTVM) was proposed by Rashed E. [86], which reduces the global variation of the signal while preserving a close match to the original form. This method is based on the concept of total variation (TV) minimisation, which is a commonly used approach for image restoration. Then, its main goal is to extract the clutter from the acquired data by forcing the TV regularisation term over the horizontal direction.

Nevertheless, most algorithms have been designed to remove a purely horizontal noise, with no possible variation in its amplitude or sign. Thus, they have a suitable performance only with constant noise.

2.3.3 Migration

It is well-known that the interpretation of a radargram is subjective and it is strictly dependent on the experience and training of the final user. Migration is the term used by geophysicists to describe the process of focusing the radargrams to more closely resemble the physical target dimensions [38]. It has been a basic tool for interpreters since at least the 1940s [97].

Due to the beamwidth of the antenna [120], targets appear as hyperbolas. Migration, based on spatial deconvolution, re-locates the apparent positions of the reflections (known as dipping reflectors) to their true positions [76] and collapses diffractions [126] resulting in a migrated radargram. This process increases spatial resolution, since a migrated image can offer an idea of the shape and the dimensions of the target [23], increasing target detectability and reducing the effect of the beamwidth.

Migration requires the true medium velocity. If an incorrect velocity model is selected, the migrated section could be misleading. With a higher migration velocity than the real medium velocity, the diffraction curve is inverted more and more, and the image is overmigrated (taking the shape of a smile [129]). Rather, with lower velocities, the radargram is undermigrated

(the resulting shape can be distinguished as a frown).

Although numerous methods have been proposed in the literature, the most reference approaches are based on Kirchoff anf F-K methods [126].

- **Kirchhoff**

  In Fig. 2.15.(a) the physical principles of migration are described using the well-known harbor example [126]. There is a storm barrier at z_3 from the beach and a gap in the barrier. Now, a calm breeze comes from the ocean as a plane incident wave, and the wavefront is parallel to the storm barrier. Then, walking along the beach, a different wavefront is seen. Thus, the gap acts as a secondary source and generates the semicircular wavefront along the beach. The experiment can be translated to a recorded time section (Fig. 2.15.(b)). The gap is known as a point aperture or Huygens' secondary source, which responds to a plane incident wave and generates a semicircular wavefront in the (x, z) plane. Thus, the response in the (x, t) plane is the diffraction hyperbola.

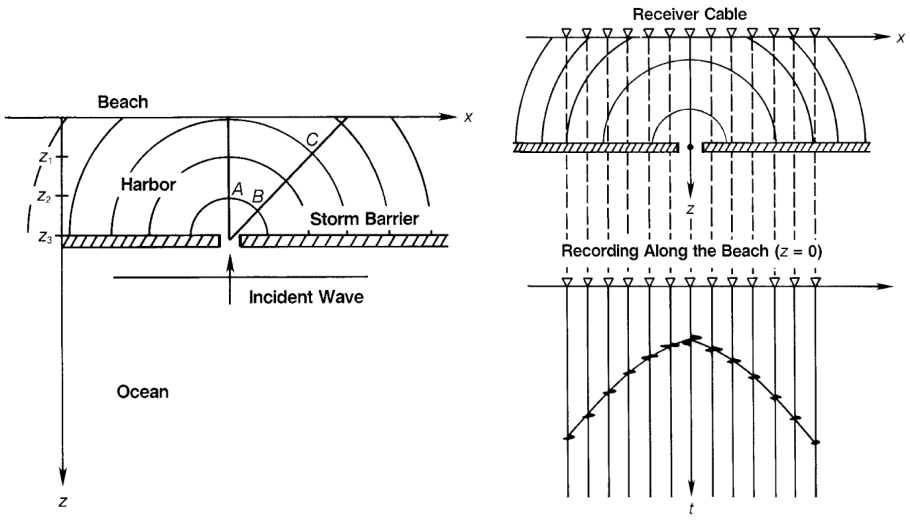

(a) (b)

Figure 2.15: The harbor example shows that the gap acts as a Huygens' secondary source (a) and the waves generated by Huygens' secondary source have a hyperbolic traveltime trajectory (b) [126].

Kirchhoff technique is based on the diffraction summation method, which is a summation of amplitudes along the hyperbolic trajectory. The curvature of the hyperbola is dependent on the velocity function. The process is based on the semicircle (the diffraction curve) superposition, mapping the amplitude at a sample in the (x, t) plane onto a semicircle in the (x, z) plane. The migrated section will consist on the superposition of multiple semicircles.

An example can be analysed in Fig. 2.16 [126], where a raw section is shown in Fig 2.16.(a). The apex of the hyperbola A corresponds to time t_0. Then, the amplitude on point B is mapped onto apex A (Fig 2.16.(b)), following the hyperbolic traveltime equation 2.23.

$$t_x^2 = t_0^2 + 4x^2/v_{rms}^2 \tag{2.23}$$

where v_{rms} is the root mean square (RMS) velocity at A in t_0.

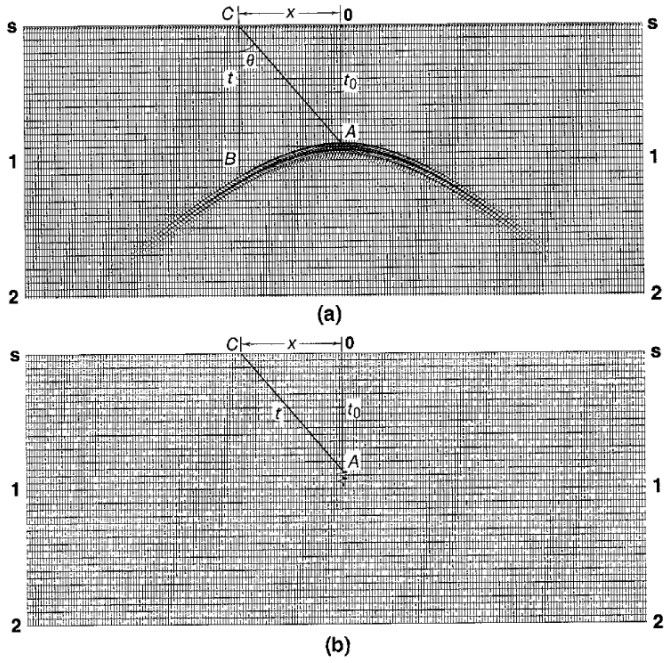

Figure 2.16: Kirchhoff Migration. (a) Raw radargram, where a target appears as the characteristic hyperbola. (b) Radargram after Kirchhoff [126].

Besides, it is necessary to consider several factors which are associated

with the amplitude and phase of the waveform along the hyperbola. Firstly, considering the example in Fig. 2.15(a), the wave amplitude at location A on the z-axis is stronger than the amplitude at B, which is at an oblique angle from the z-axis. Then, this angle dependence of amplitudes should be corrected, which is known as the obliquity factor. Secondly, the wave amplitudes suffer a spherical divergence. The wave energy decays as $1/r_{sw}^2$, where r_{sw} is the distance from the source to the wavefront, while amplitudes decay as $1/r_{sw}$. Thus, all of the amplitudes should be scaled by this spherical spreading factor. Finally, the wavelet shaping factor, which is an inherent property of Huygens' secondary source waveform should restore the phase and the amplitude of the hyperbolic paths. When the diffraction summation method which has been explained incorporates the obliquity, the spherical spreading and the wavelet shaping factors, it is called Kirchhoff method.

In practice, the choice of the aperture width and the maximum dip is critical to preserve dipping events and to decrease computational cost. In Fig. 2.17 a diffraction hyperbola and the resulting migrations using four aperture widths are shown. When the selected aperture is small, the migration is less capable in collapsing the hyperbola. Besides, velocity errors can occur as explained before, as can be observed in Fig. 2.18. When the selected velocity is lower than the medium velocity, undermigration appears (Fig. 2.18(a)), whereas if the velocity is higher than the real medium velocity it causes overmigration of the diffraction hyperbola (Fig. 2.18(b)).

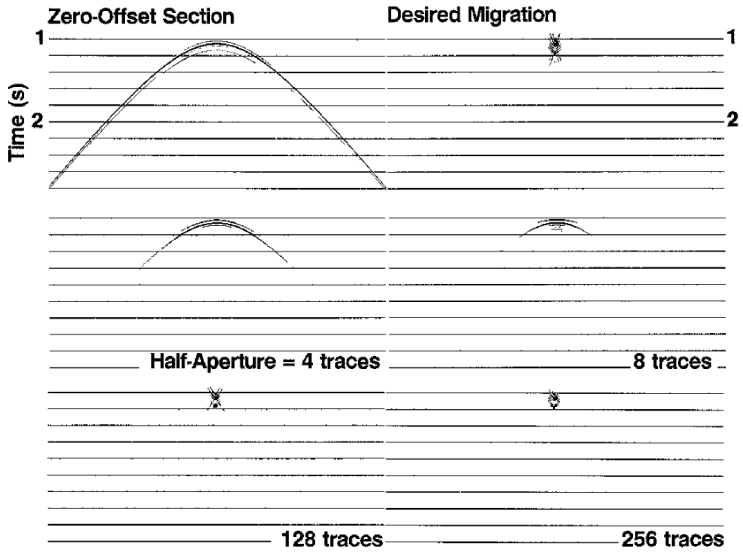

Figure 2.17: Test examples of aperture widths in Kirchhoff migration [126].

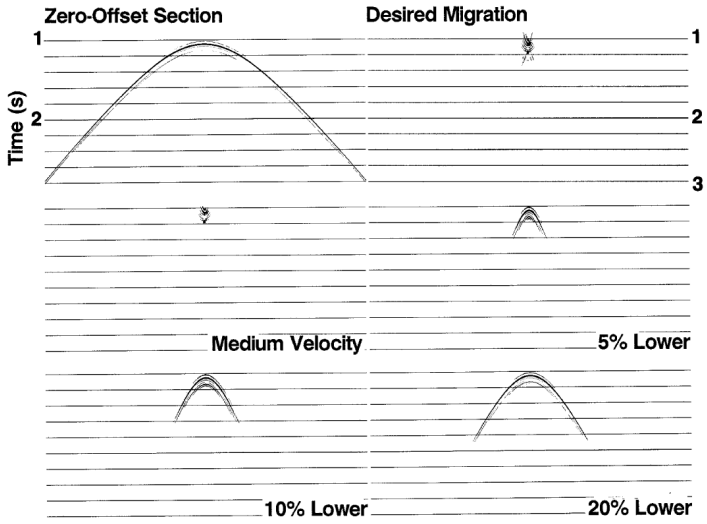

(a) Example of Kirchhoff migration using a lower velocity than the medium velocity

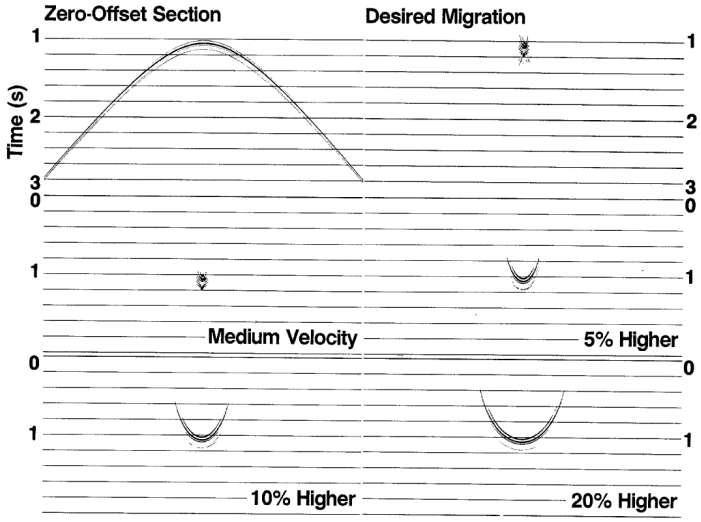

(b) Example of Kirchhoff migration using a higher velocity than the medium velocity

Figure 2.18: Test examples of velocity errors in Kirchhoff migration [126].

- **F-K (Stolt)**
  Stolt [109] [110] incorporated the Fourier Transform in migration. This method includes the frequency-wavenumber $(\omega - k)$ range. Originally, this method was based on a constant velocity assumption.

A F-K migration example [126] is represented in Fig. 2.19, where velocity is assumed to be 1. A pre-migrated target is shown in Fig. 2.19.(a) by the radial line $0B$, where the vertical axis is the frequency axis ω. Then, F-K migration maps lines of constant frequency (AB) are changed to circles (AB') in the new plane (k_z, k_x). Then, mapping is completed, and the dipping event $0B$ has been mapped to $0B'$ after migration (Fig.2.19.(b)).

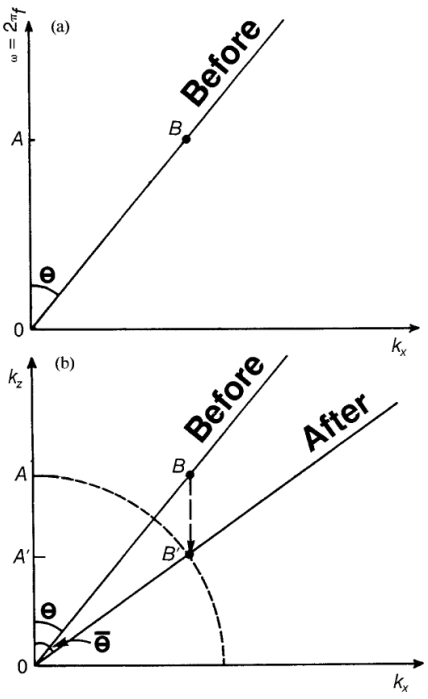

Figure 2.19: F-K Migration. (a) A dipping reflector is represented by $0B$ in the (f, k) plane. (b) After migration, the radial line $0B$ has been mapped to $0B'$ [126].

Now the diffraction hyperbola is examined, using the example shown in Fig. 2.20, which is collapsed to the apex after the F-K migration. This hyperbola is composed of a series of dipping segments, such as A, B, C, D and E, where A is the apex and E is the steepest dip along the asymptotes. Then, in the (f, k) space, the A segment is mapped along the frequency axis, the other segments are mapped along radial lines, increasingly away from the frequency axis. The last segment E is mapped along the radial line, which represents the boundary between

the propagation and the evanescent region (located at or greater than 90 degrees from the vertical).

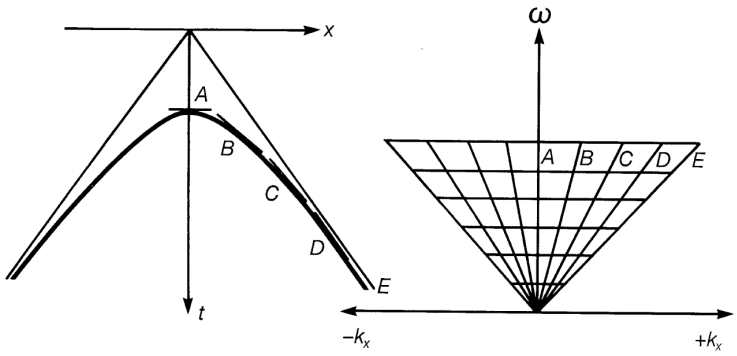

Figure 2.20: The diffraction hyperbola in the (x, t) plane is mapped onto a triangular area in the (f, k) plane [126].

If the medium velocity is constant, F-K migration can be expressed as a direct mapping from temporal frequency to vertical wavenumber, as observed in Fig. 2.19. However, Stolt extended his method to handle velocity variations.

Due to the fact that it is Fourier based, it is the fastest known migration method [13]. However, velocity errors can also cause under- or overmigrated radargrams (all the examples for the Kirchhoff migration presented in Fig. 2.18 can also be considered for the F-K method), together with problems related to the maximum dip selected.

2.3.4 Pattern recognition

Therefore, more emphasis should be now placed on classification of patterns in radargrams, in order to discriminate different buried objects or anisotropies of a material. Then, some authors [3] [33] [114] [77] have designed pattern recognition algorithms applied to these GPR images.

Al-Nuaimy et. al [3] proposed a system for automatically detect buried objects with GPR. The diagram of the processing steps is shown in Fig. 2.21. First, the radargram is pre-processed applying background removal, path loss compensation and low-pass filtering. Then, pattern recognition is used to discriminate the buried targets and the unwanted signals. Thus, a neural network classification is applied.

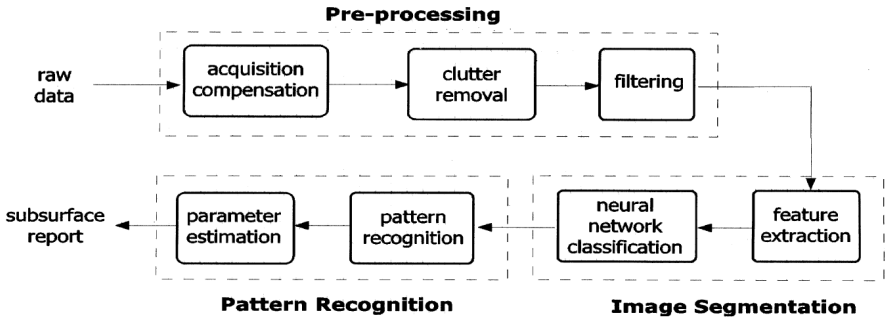

Figure 2.21: Flow diagram of the proposed method by Al-Nuaimy [3].

Falorni et. al [33] conducted a processing method to extract hyperbolic patterns inside the radargrams. Ting-jun et. al [114] also performed a model to extract hyperbolic signatures in GPR.

Sezgin [102] developed a 2D template matching method for establishing a discrimination of buried objects, following the flow diagram of the Fig. 2.22. First, starting from the B-scan image, a background subtraction is applied and then, the radargram is normalized to positive values between 0 and 255. Then, as image should be binarized, the author applies a thresholding using the Minimum Error Thresholding [53]. Subsequently, a morphological process is used, applying an skelonization process. The whole process is applied to the templates and to the B-scan images. Finally, the author calculates the correlation between the templates and the radargrams using the Euclidean distance measure. The evaluation is performed using radargrams of buried metallic objects, with promising classification results.

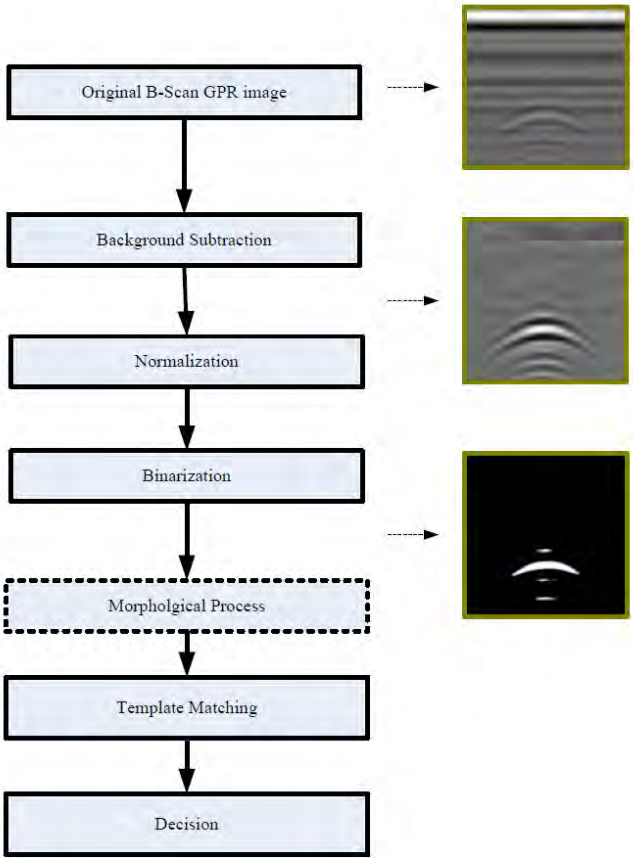

Figure 2.22: Flow diagram of the proposed method by Sezgin [102].

In addition, Pasolli et. al [77] introduced a pattern recognition system to classify buried objects (Fig. 2.23). After a pre-processing step, the radargram is thresholded. Then, the system automatically detects the objects by means of a search of linear or hyperbolic patterns. These templates are formulated using a genetic optimization framework, where the apex and the curvature are modelled. Finally, a support vector machine approach classifies the object. The performance of the proposed method is evaluated using a synthetic database varying the number of buried objects (their position, size, shape and material).

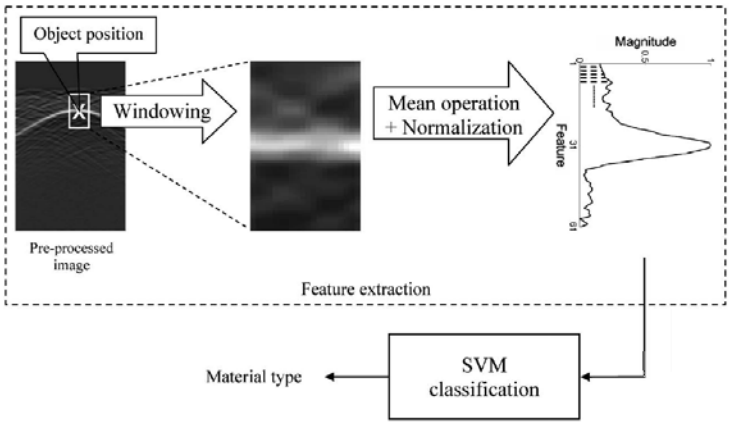

Figure 2.23: Flow diagram of the proposed method by Pasolli et. al [102].

2.4 3D modelling in GPR

A 3D model of a stone product can offer a better understanding of its internal structure, offering a vision of the depth, shape and the spatial orientations of the detected fractures. However, the diffusion of 3D radar investigations is limited. One of the main problems is related to the acquisition technique: the grid of measurement data as well as the selected frequency will affect the accuracy of the model. Other relevant issue is the selected 3D processing software.

In this section, a review of authors [40] [60] [47] [68] [100] [57] who have used GPR to create 3D models is presented.

Grandjean and Gourry [40] developed a 3D fracture mapping. To obtain this type of representation, the author proposed the correlation of the fractures from each profile with the nearest one. Luodes [60] established a measurement grid on a quarry in two directions, offering an schematic 3D visualization, where the propagation of the fractures is showed in Fig. 2.24. Later, Kadioglu [47] presented a simple 3D visualization to determine changes in layer thickness and discontinuities. For this purpose, parallel 2D profiles are measured and displayed in a 3D grid. Nielsen et. al [68] collected a 3D GPR dataset over a limestone quarry using a 100 MHz antenna mounting the different profiles along the positions. Sengondan et. al [100] created a 3D reconstruction for the location of foundations in demolished buildings, comparing its results with the output of ReflexW software [87]. For this

purpose, the author used a simulated correlation algorithm (SIMCA) which is based on a comparison between the trace that would be returned by an ideal point reflector and the actual trace. Lualdi and Zanzi [57] carried out a GPR survey to create a 3D reconstruction for a cultural heritage application, improving the acquisition of the data to ensure the quality of the results. The authors stated that the 3D reconstruction is successful particularly in the detection of the hidden structure of timber floors or roofs. Besides, the system should ensure a correct antenna position and orientation, covering a regular grid of measuring points.

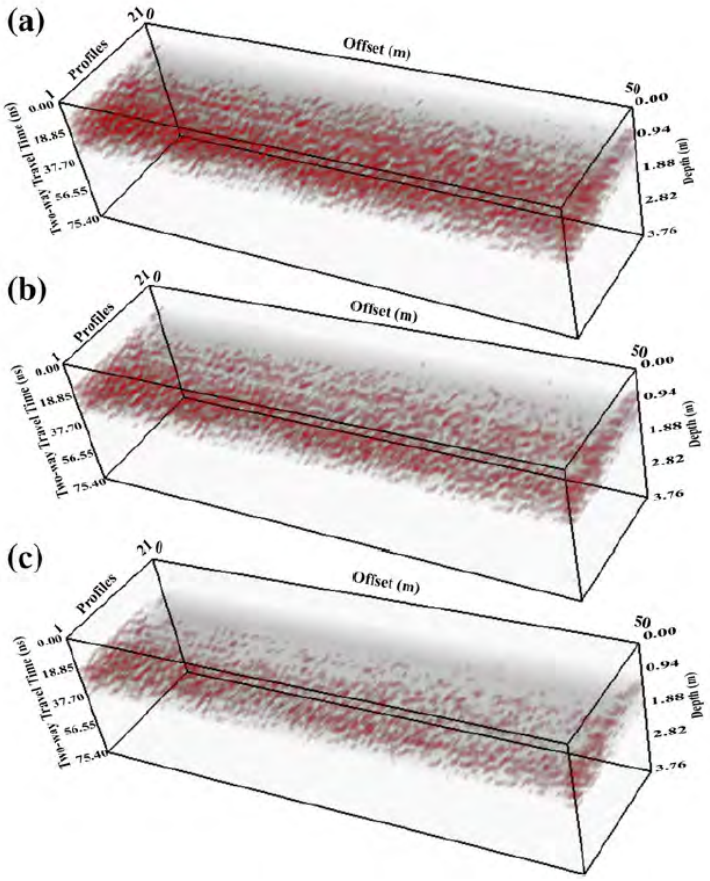

Figure 2.24: 3D data volume which highlights the fractures at different depths ((a), (b) and (c)) [47].

Chapter 3

Methodology

This chapter describes the methodology used for each publication presented in this Thesis. First, the experimental work, with synthetic and real data, is detailed. Then, the setup, the involved materials, the databases and the metrics are described for each publication.

3.1 Experimental work description

The acquisition system, for both synthetic and real data, is completely described for each of the associated publications.

3.1.1 Simulation software

When a a signal processing method is proposed, a synthetic database is essential for training, as well as for evaluating its performance.

Several simulations have been conducted using the modelling software ReflexW [87] [84] in [P2] and [P3]. This widely used commercial package [30] applies the Finite-Difference Time-Domain (FDTD) method to simulate EM waves. This interactive software is used to define layer boundaries, while the EM parameters are defined along such boundaries. These parameters are entered within a table. Besides, a random-layer option can be used in order to specify statistic parameters for a random perturbation of the physical parameters of the layers, using different spatial distributions.

The objective is to set a configuration similar as a real GPR system, and with conditions similar to a real scenario. This simulated data has been used for designing the method and to test the results as argued before.

Moreover, as explained in Section 2.1 in Chapter 2, the EM parameters should be adjusted to the real properties of this type of stone.

3.1.2 Equipment for real acquisition data

In this Section, the real acquisition system for [P1], [P2] and [P3] is described.

A MALAGS Pro-Ex model RAMAC [61] GPR system has been employed to conduct every survey. The configuration has been modified in according to the selected antenna, the material and the desired depth to evaluate.

For quarries studies, antennas of 100, 250 and 800 MHz were used. Results indicated that the use of 250 MHz antenna is an optimal choice in order to analyze quarries due to its good resolution and accurate depth. Focusing on the analysis applied to extracted stone blocks, an antenna of frequency equal to 800 MHz is selected, due to its resolution and because the reached depth covers the size of the studied blocks.

3.2 Characterization of ornamental stone

The following description is related to publication [P1]. This work is only focused to real data.

3.2.1 Setup

Since real data of different depths need to be evaluated, three different antennas will be used, taking into account that for quarries, which present a higher depth, it was necessary to use low frequency antennas, whereas for blocks, which have a lower depth, the highest frequency antenna has been employed.

The operating parameters were selected, as indicated in Table 3.1.

Operating Parameter	**Value**
Antenna nominal frequencies	100, 250 and 800 MHz
Sampling interval	0.03 m
Sampling frequencies	1100, 2610 and 7964 MHz
Time windows	410, 185 and 47 ns

Table 3.1: Setup of the real data acquisition related to publication [P1]

For each antenna nominal frequency a particular sampling frequency (about ten times the nominal frequency) and a certain time window are selected. It is considered that the depth decreases as the nominal frequency increases. Besides, the velocity (about 100 mm/ns) has been experimentally estimated. Finally, the sampling interval has been calculated in order to satisfy the Nyquist criteria.

3.2.2 Material

The study is focused on white-coloured marble quarries, known commercially as *White Macael*. Besides, two types of carbonated lithologies have been employed: a clear limestone known as *Crema Marfil* (*White Ivory*) and a highly porous red limestone, known as *Red Travertino*. The last lithology has been selected because the anisotropies cause problems in the exploitation of the quarry and in the cutting process.

The *White Macael* quarry face presents two differentiated zones: a marble unit and a mica schits unit. Besides, it has a sub-vertical cavity.

The three blocks (*Macael Marble*, *Crema Marfil* and *Red Travertino*) present no defects.

3.2.3 Database

On the one hand, several profiles have been obtained at the *White Macael* quarry faces using the 100, 250 and 800 MHz antennas.

On the other hand, GPR has been applied to extracted blocks of the three types (*White Macael*, *White Ivory* and *Red Travertino*) using the 800 MHz antenna.

Note that several signal pre-processing methods, e.g., filtering and gain, has been applied in the tests using the software RadExplorer [84].

3.3 Detection and Classification of fractures

The following description is related to publication [P2]. Synthetic and real data acquisition is presented.

3.3.1 Setup

Simulated data

These synthetic radargrams are used for training and for the evaluation of the proposed algorithm. Besides, two databases, one for synthetic data and other for real data, are created, in order to check the results.

Since the blocks present a depth which is covered by the 800 MHz antenna, this frequency is selected for the analysis, since it provides the highest possible resolution with our equipment, and it is necessary to simulate with similar characteristics to the real measurements. In Table 3.2 the selected parameters are shown.

Operating Parameter	**Value**
Antenna nominal frequency	800 MHz
Sampling interval	0.005 m
Sampling frequency	62.5 GHz
Permittivity of stone	8
Permittivity of air	1
Time window	35 ns

Table 3.2: Setup of the simulation related to publication [P2]

The selected time window has been calculated according to the velocity (about 106 mm/ns) and the depth of the simulated profile. The permittivity of the stone is selected in accordance with the real material which is analyzed. The sampling interval satisfies the Nyquist criteria. The sampling frequency is automatically selected by the ReflexW software. Finally, the time window is enough to cover the whole depth of the simulated block.

Real data

In this case, only a 800 MHz antenna has been employed, since it is the highest frequency of our equipment, covering the necessary depth with the highest resolution. The survey design is described in Table 3.3.

Since the two measured blocks present different dimensions the time window has been adjusted to covering their corresponding depths. Besides, the sampling interval satisfies the Nyquist theorem. The sampling frequency is selected as ten times the nominal frequency.

Operating Parameter	Value
Antenna nominal frequency	800 MHz
Sampling interval	0.026 m
Sampling frequency	8 GHz
Time windows	36 ns / 39 ns

Table 3.3: Setup of the real data acquisition related to publication [P2]

3.3.2 Material

Simulated data

The objective of this simulation is to design profiles as closely to reality as possible with ReflexW. For this reason, the selected permittivity is 8. However, we can affirm, as mentioned in Section 2.1.1 in Chapter 2, that the value of permittivity of limestone varies between 7 and 9, with a normal distribution. Then, the part of stone of each profile is simulated as a layer with a random value between these limits. Then, the air-filled fracture, which presents different sizes, has been included, with a permittivity of 1.

Real data

With regard to real measurements, the studies that have been conducted in [P2] are focused on blocks of cream-coloured massive limestone, known as *Crema Marfil* (*White Ivory*), exploited in the Sierra de El Coto, next to the town of Pinoso (Alicante, Spain).

Specifically, two blocks of different quality are tested. On one side, a top-quality block with dimensions of 160x300x140 cm is analysed. This block has an apparently good quality. The cutting process resulted in forty-six tables, and the report indicated that only four tables presented some minor problems (horizontal and diagonal filled fractures which did not cause breakage).

On the other side, a second-quality block, with visible fractures, with dimensions of 120x260x160 cm is tested. It presented some visible fractures. After the cutting process, which resulted in fifty-three tables, several slabs presented major problems. Specifically, three tables suffered from an important vertical break, so they were completely broken in half. The intermediate tables had vertical fractures, but they did not cause breakage. Finally, the last table had a horizontal fracture, which caused the breakage of the slab.

3.3.3 Databases

Simulated data

First, a database for training has been created. It is composed of four simulated models that represent four different spatial orientations of a fracture: horizontal, vertical and diagonal fractures with tilt angles of 45° and -45°. The fractures of the simulated block have a length of 0.2 m and a width of 0.002 x 0.2 m, where the term length is referred to the larger linear dimension regardless of its spatial orientation, and the term width refers to the smaller dimension. Once the simulation is performed, using the parameters described in Section 3.3.1, the resulting radargrams are used for the training of the algorithm.

Then, in Fig. 3.2, the resulting radargrams are shown. The difference between the B-scans indicates that a classification of the defects can be done. Besides, as can be observed, the positions of the diagonals fractures suffer a lateral shift. This is due to the geometry of the zero-offset acquisitions. When increasing the inclination of the diagonal, the lateral shift increases too.

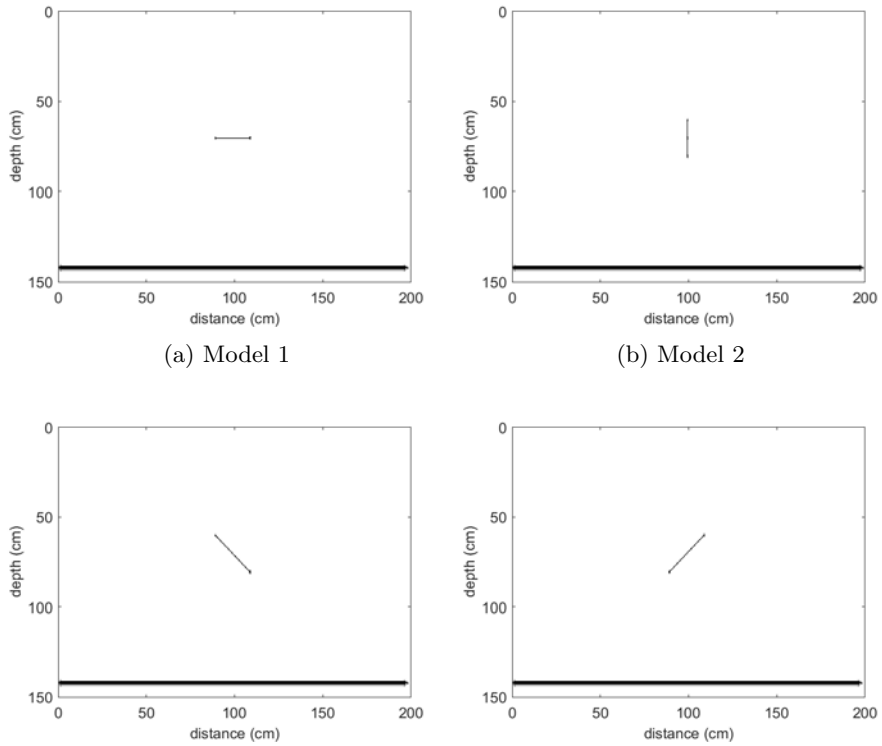

(a) Model 1 (b) Model 2

(c) Model 3 (d) Model 4

Figure 3.1: The four models that constitute the training database of publication [P2]. In this case, white colour represents a permittivity value of 8 (the stone part of the block) whereas the black colour is related to the air, so the permittivity is 1.

In Fig. 3.1, the four created fractures are displayed. They have been modelled using ReflexW as explained before.

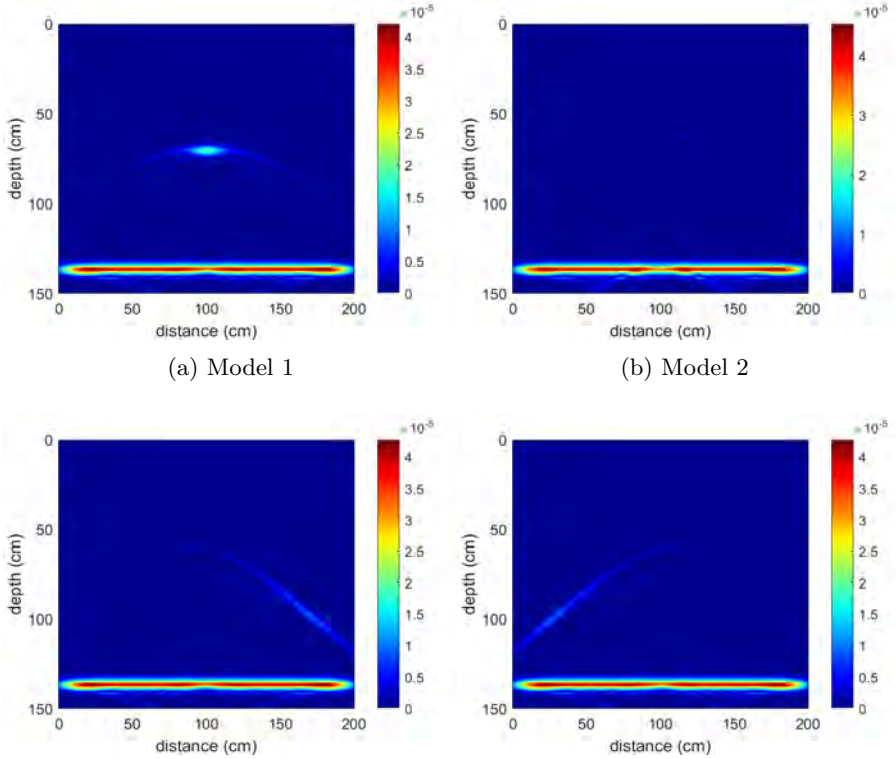

(a) Model 1 (b) Model 2

(c) Model 3 (d) Model 4

Figure 3.2: The four radargrams related to the four models of the database of publication [P2] shown in Fig. 3.1. As can be observed, each resulting radargram comprises only non-negative values.

Secondly, a new database for evaluation is composed of a total of 41 profiles of stone, with the above-mentioned characteristics (a random value of permittivity between 7 and 9). The last one (File 41) is a profile with no defects. This database is described in Table 3.4. In each of them, an air-filled fracture has been included, with different spatial orientation (from 0° to 90°), width and length. Then, this model has been processed, in the same way as a real GPR captures the data, and each radargram is extracted. Besides, radargrams from other 40 profiles, with the same characteristics but with a fixed permittivity of 8 have also been obtained.

Real data

According to the two blocks described in Section 3.3.2, the extracted database is now detailed. A report provided by the factory charged with cutting the

File	Width (cm)	Length (cm)	Orientation (°)
1	1	10	0
2	1	20	0
3	1	30	0
4	1	40	0
5	1	50	0
6	0,02	30	0
7	0,05	30	0
8	0,08	30	0
9	2	30	0
10	3	30	0
11	1	10	45
12	1	20	45
13	1	30	45
14	1	40	45
15	1	50	45
16	0,02	30	45
17	0,05	30	45
18	0,08	30	45
19	2	30	45
20	3	30	45
21	1	10	90
22	1	20	90
23	1	30	90
24	1	40	90
25	1	50	90
26	0,02	30	90
27	0,05	30	90
28	0,08	30	90
29	2	30	90
30	3	30	90
31	1	30	5
32	1	30	10
33	1	30	20
34	1	30	30
35	1	30	40
36	1	30	50
37	1	30	60
38	1	30	70
39	1	30	80
40	1	30	85
41	-	-	-

Table 3.4: Detailed information about length, width and orientation of each file of the database related to publication [P2].

block shows the number of breaks of each table, with pictures of the problems encountered, which enriches the database.

First, for the top-quality block, a total of 15 profiles of 10 cm, covering its top face, were taken. Secondly, for the second-quality block, 11 profiles of 10 cm had been measured along the top face of the block. Standard pre-processing, using the software RadExplorer, has been applied in both blocks. Specifically, DC removal, background removal, AGC and band-pass filtering have been used.

3.3.4 Metrics

The metrics that have been used to assess the performance of the methods are detailed here. On the one hand, we use the model which has been simulated; and on the other hand, the resulting migrated radargram.

The next three metrics [46] have been calculated for each file of the database, where N_D^{corr} and N_N^{corr} are the total number of pixels with defects and the total number of pixels with no defects that are correctly classified from the reconstructed radargram, respectively; $N_D^{notcorr}$ and $N_N^{notcorr}$ are the total number of pixels with defects and the total number of pixels with no defects erroneously classified from the reconstructed radargram, respectively; and $N_D = N_D^{corr} + N_D^{notcorr}$ and $N_N = N_N^{corr} + N_N^{notcorr}$ are the total number of pixels with defects and the total number of pixels with no defects from the model, respectively.

- Accuracy (ACC): percentage of correctly classified pixels. This value will not be significant, due to number of pixels of stone is truly bigger than the number of pixel related to defect in the radargram, so ACC will always be a high value in this application.

$$ACC = \frac{N_D^{corr} + N_N^{corr}}{N_D + N_N} \times 100 \tag{3.1}$$

- Hit rate (HR): percentage of pixels with defects that have been correctly classified. This will be the most relevant value, since a HR bigger than 0 will indicate that the profile has a defect, and the detection will be activated.

$$HR = \frac{N_D^{corr}}{N_D} \times 100 \tag{3.2}$$

- False alarm (FA): percentage of pixels with no defects that are erroneously classified. This metric will be a relevant value, because it useless a method with high values of HR with high values of FA. It is mandatory that the method will get the minimum FA value possible.

$$FA = \frac{N_N^{notcorr}}{N_N} \times 100 \tag{3.3}$$

3.4 GPR Background removal

In this Section, the acquisition system of [P3] is described.

3.4.1 Setup

Simulated data

This database can be divided into two different sub-databases: one for development of the method and one for evaluate its performance.

An 800 MHz antenna is used for creating the database. In Table 3.5 the selected parameters are selected.

Operating Parameter	**Value**
Antenna nominal frequency	800 MHz
Sampling interval	0.005 m
Sampling frequency	62.5 GHz
Permittivities	1-8
Time window	35 ns

Table 3.5: Setup of the simulation related to publication [P3]

The selected time window has been calculated according to the velocity (about 106 mm/ns) and the depth of the simulated profile. Besides, the permittivity value varies between 1 and 8. Moreover, the sampling interval satisfies the Nyquist criteria. The sampling frequency is selected by ReflexW.

Real data

In order to evaluate the method, it is necessary to check its performance with data of several antennas. For this reason, data measured with different frequencies is used. Table 3.6 shows the operating parameters.

Operating Parameter	Value
Antenna nominal frequencies	1.6 GHz / 250 MHz / 800 MHz
Sampling intervals	0.004 m / 0.007 m / 0.004 m
Sampling frequencies	16.4 GHz / 2.54 GHz / 7.96 GHz
Time windows	46 ns / 120 ns / 36 ns

Table 3.6: Setup of the real data acquisition related to publication [P3]

Since two blocks, with different dimensions, are measured, the time window has been adjusted to covering their whole depths. Besides, when changing the antenna nominal frequency, the sampling frequency (about ten times the nominal frequency) and the sampling interval (satisfying the Nyquist criteria) should be readjusted.

3.4.2 Material

Simulated data

The created profiles model a block of stone with a dimension 1.5x2 m, using, as mentioned above, different relative permittivity as shown in Fig. 3.3. Then, radargrams are obtained to create the database. The relative permitivitties vary from 1 to 8.

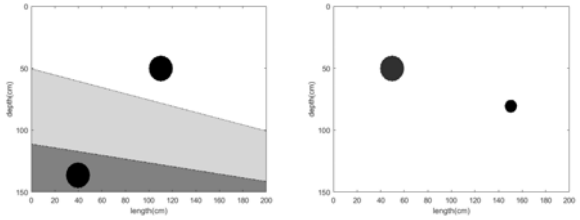

(a) Model 1

(b) Model 2

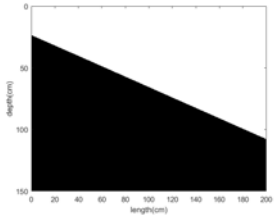

(c) Model 3

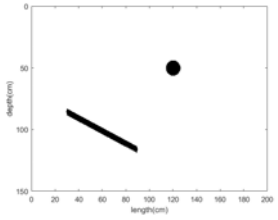

(d) Model 4

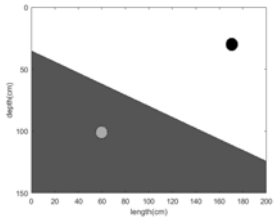

(e) Model 5

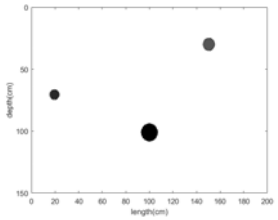

(f) Model 6

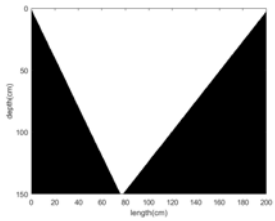

(g) Model 7

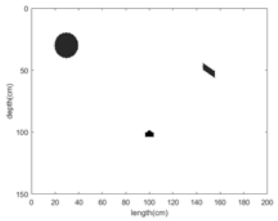

(h) Model 8

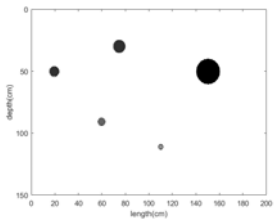

(i) Model 9

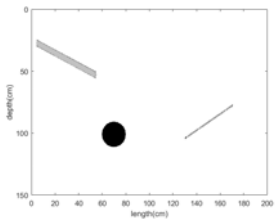

(j) Model 10

Figure 3.3: The set of models of a block of the database related to publication [P3]. The selected relative permitivitties vary from 1 (black) to 8 (white).

Real data

Two blocks and a quarry face are evaluated, as appears in Table 3.7.

Material	Type	Quarry	Distance (m)	Depth (m)
Negro Calatorao	Block	Calatorao (Zaragoza, Spain)	1.9	1.3
White Macael	Quarry face	Macael (Almería, Spain)	11	5.1
Crema Marfil	Block	Pinoso (Alicante, Spain)	2.1	1.8

Table 3.7: Characteristics of the measured data of [P3].

As can be observed, materials with different textures have been selected for the evaluation. Specifically, the first material, *Negro Calatorao*, is employed due to its layered structure whose laminations severely complicates the detection of anisotropies. The second material, *White Macael*, is collected from a white-coloured marble quarry and it present a more homogeneus structure. Finally, the third material, *Crema Marfil*, is extracted from a clear limestone block, with similar characteristics to the second material.

3.4.3 Databases

Simulated data

As mentioned above, two databases are created. For each of the ten models, a different type of synthetic noise is applied. Then, background noise is modeled as horizontal strips:

- N_A: constant amplitude
- N_B: variable amplitude
- N_C: variable amplitude with alternated positive and negative values
- N_D: amplitude with sinusoid variation

This type of noise can be seen in Fig. 3.4, which will be summed to each of the radargrams obtained from the models described in Fig. 3.3.

Real data

As regards real measured data, only one profile of each material described in Table 3.7 is measured, along the whole distance.

3.4.4 Metrics

The relative root mean square error (RRME) is used to evaluate the performance of the method (equation 3.4). This metric measures the error between the noise-free radargram and the estimated noise-free radargram. Besides, is has been used to assess the results of background methods [86].

$$RRME = \sqrt{\frac{\sum_{F}^{p=1} \sum_{T}^{d=1} (\hat{X}_a(p,d) - X_a(p,d))^2}{\sum_{F}^{p=1} \sum_{T}^{d=1} X_a^2(p,d)}} \tag{3.4}$$

where X_a is the noise-free radargram, $\hat{X}_a$ is the estimated noise-free radargram, $p = 1, ..., F$ rows related to penetration depth and $d = 1, ..., T$ related to distance.

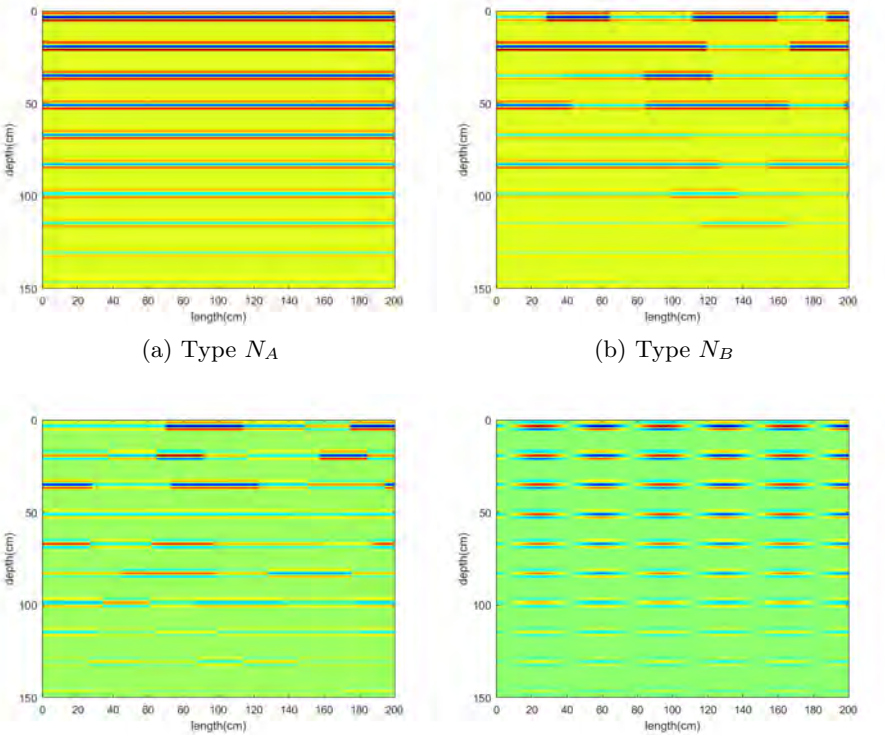

(a) Type N_A (b) Type N_B

(c) Type N_C (d) Type N_D

Figure 3.4: Types of noises of the database related to publication [P3].

Chapter 4

Results, Conclusions and Future Work

This Chapter presents results and conclusions of the performance of the proposed signal processing methods derived from each publication of this Thesis.

4.1 Characterization of ornamental stone

In paper [P1] a novel method to evaluate the internal structure, highlighting the texture and the presence of defects, in carbonated stones is presented. The measured data is first pre-processed. Then, SI-PLCA approach is applied, with the objetive of searching for GPR pulses. The activations of such pulses form the new GPR image. Besides, a variable-gain process, which compensates the energy losses, is employed. It is assumed that the energy of each pulse is approximately equal, since the GPR transmits the same pulse to each frame, independently of the encountered reflections.

The method has been evaluated using a database composed of GPR measurements, with antennas of 100, 250 and 800 MHz, over a stone quarry and three types of blocks. For the investigated quarry, a correlation between the observed geological data and the extracted and processed data is proved: two units, one corresponding to a massive upper unit (marble) and the other related to mica schits, are completely distinguished. For the case of the three evaluated blocks, two of them present no defects, information that is correlated with the reality. However, the novel method of

the third block proves the typical anisotropy of this material. The results clearly demonstrate the usefulness of GPR as a fast and efficient diagnosis tool of stone materials. Once the SI-PLCA algorithm conducted the deconvolution, every anisotropy is clearly highlighted and it allows a clearer reading of the radargram. Besides, applying the sparseness restriction, only the radargram zones with a high probability of having a anomaly are left. Then, the algorithm eliminates part of the radargram noise, since only the radargram zones with anomalies are marked. Thus, the experience of the user may not be as mandatory as before. Thus, the extracted information can be used prior to the extraction process in the quarry and during the cutting of the blocks or for the selection of ornamental stones prior to their use in artistic work or monuments.

The characterization of the quality and texture of stone materials using GPR has a wide range of potential applications. We have worked on extending this method using SI-PLCA to perform an improvement of the detection and classification of fractures in stone materials. Besides, this work suggested that the GPR response is better for sub-vertical than for horizontal defects.

4.2 Detection and Classification of fractures

Following [P1], it is considered the need to develop an automatic method which could be able to detect fractures, and to offer information about the spatial orientation of them. Then, one method for detection and other method for both detection and classification are developed. All of the measured radargrams follow the next process: pre-processing, envelope detection, migration and finally thresholding. First, DC removal, Background Removal, AGC and Band-Pass Filtering routines are conducted. Second, the technique detects the envelope, using the Hilbert Transform (HT), which is a widely used process for expressing a band-pass signal as a low-pass signal and a phasor [20]. Then, migration methods (the novel and classic migration methods) are applied. The novel detection method uses a hyperbola pattern as input kernel of the SI-PLCA algorithm, detecting the zones of the radargram with this pattern. The classification method, uses four kernels, for detection and classification: horizontal, vertical, diagonal with a title angle of 45° and finally a diagonal with a title angle of -45°. SI-PLCA offers

an output for each pattern, showing the activation of each type of defect. Besides, as the energy return from a vertical pattern is lower than the energy from a horizontal defect, a factor of compensation is calculated and applied. Finally, the targets are extracted, selecting an adequate threshold. This is solved using the Otsu's method [75].

The evaluation is performed using two test databases. First, a synthetic database composed of 41 files, with different orientation. According to the detection performance, the results are compared to the two classic migration methods. ACC, HR and FA rates are calculated, using the original simulated model and the migrated radargram of each method. The results show a reasonable performance of the classification method. Whereas all the methods obtain a quasi-perfect performance for horizontal fractures, our proposed method achieves a satisfactory performance when detecting vertical defects. In the case of diagonal defects, the classification method gets also the best result. When the defect varies its angle, our classification method detects all the fractures. Now, it is necessary to compare the performance using more input kernels, adding two diagonals with different angle. The results indicate that, with a higher number of kernel, the energy is dispersed among all of them, as well as the complexity is increased. On the other hand, the classification results of the classification method are compared to a pattern-recognition approach. For this purpose, the distribution of energy of each pattern, when using the SI-PLCA algorithm, is compared the mentioned method. In most cases, both methods correctly classify the orientation of the defect. Nevertheless, the novel classification method is able to classify the defect more accurately. Besides, it provides higher probability of correct classification. Finally, it is necessary to evaluate the performance of the method with a real database. For this purpose, two stone blocks of different qualities are tested. A 3D map is conducted, which provides information about the fractures for each orientation pattern, comparing the results with a complete report of the factory charged with cutting the blocks. The 3D classification maps, as a novelty, clearly show the main fractures in the block with lower quality, and they clearly show that the highest quality block has no relevant defects. In conclusion, these results suggest that the information with can be provided by our classification method is able to provide a evaluation of the quality of any block, with high resolution. Besides, we do not only detect the defect, with the highest performance, but it is correctly

classified, which remains a novelty in migration methods. Besides, one important innovation is related to the detection and classification of vertical defects, because they are critical in the cutting process of the blocks.

Future work will focus on extending the method to different types of stones. Moreover, the acquisition process will be performed with measurements on three block faces, and with correlations between them can improve the accuracy of the 3D maps. Lastly, the 3D maps can be used for other applications such as archaeological studies.

4.3 GPR Background removal

In [P3] we proposed a novel method to remove the background noise, based on the non-local similarity of regions over the distance. First, background noise pattern is analysed. It shows a quasi-periodic pattern in depth (in the direction perpendicular of the movement of the antenna) and a flat and horizontal pattern in distance (in the direction parallel of the movement of the antenna). Then, this noise is composed of horizontal lines of energy. Then, the method is based on two assumptions related to the background noise: it is is approximately repetitive in the direction of the movement of the antenna and it shows similar or predominant energy compared to the rest of the radargram. This method have three stages: segmentation, similarity-repeatability and non-neighboring constraint. During the first stage, the radargram is segmented. The section is a submatrix of the input radargram which cover the whole distance (in the direction of the movement of the antenna). The region is a submatrix of the section. The second stage is related to the similarity-repeatability, which identifies regions candidates. For each region, the similarity is computed taking into account the remaining regions. The Euclidean distance (EUC) is selected due to its quality and low computational cost. Finally, the third stage incorporates a necessary restriction, since a high value of similarity may no imply a valid candidate region: the distance between the evaluated regions must be taken into account. Then, the constraint excludes the neighboring regions. Besides, the minimum distance between the regions is a parameter that needs to be optimized.

Once the algorithm is designed, a synthetic database is created, with four types of noise. A part of this data is used to train the method, in order to select the best parameter related to the minimum distance and to

the size of the regions. Then, the test synthetic database, with the four type of noises, is used to do the complete evaluation of the method, which is processed by state-of-the-art methods: ATS, BMS and DTVM. The proposed algorithm provides the best performance compared to these methods. Moreover, it achieves the lowest computational cost. On the other hand, the evaluation is completed using a real database, with suitable results based on visual inspection. This novel method, unlike the classic background removal methods, models correctly the irregular pattern of noise, conserving the true anisotropies present in the radargrams.

We are working on modelling and incorporating temporal or spectral features into an unsupervised or semi-supervised approach in order to extract different types of GPR background noise.

Bibliography

[1] Abujarad F., Jostingmeier A., "Clutter removal for landmine using different signal processing techniques", *Tenth International Conference on Ground Penetrating Radar*, pp. 697-700, 2004.

[2] Abujarad F., Omar A., "GPR Data Processing Using the Component-Separation Methods PCA and ICA", International Workshop on Imaging, Italy, 2006.

[3] Al-Nuaimy W., Huang Y., Nakhkash M., Fang M.T.C., Nguyen V.T., Eriksen A., "Automatic detection of buried utilities and solid objects with GPR using neural networks and pattern recognition", *Journal of Applied Geophysics*, vol. 43, pp. 157-165, 2000.

[4] Allred B., Daniels J. J., Ehsani M. R., "Handbook of Agricultural Geophysics", *CRC Press*, 2008.

[5] Annan A. P., Davis J.L., "Impulse Radar Soundings in Permafrost", *Radio Science*, vol. 11, pp. 383–394, 1976.

[6] Annan A. P.,"Ground Penetrating Radar Principles, Procedures and Applications", *Sensors and Software*, 2003.

[7] Apel D. B., Dezelic V., "Evaluation of high frequency ground penetrating radar (GPR) in mapping strata of dolomite and limestone rocks for ripping technique", *International Journal Of Surface Mining, Reclamation And Environment*, vol. 19, pp. 260–275, 2005.

[8] Arosio D., Munda S., Zanzi L., "Quality control of stone blocks during quarrying activities", *14th International Conference on Ground Penetrating Radar (GPR)*, Shangai, China, 2012.

[9] Arosio D., Munda S., Zanzi L., Porto F., Mosele F., "Nondestructive Quality Control of Reinforced Masonry Buildings", *Journal of Infrastructure Systems. Special Issue: Nondestructive Testing in Civil Engineering*, vol. 18, no. 1, pp. 34-46, 2012.

[10] Arosio D., Zanzi L., Longoni L., Papini M., "Fracture thickness from GPR measurements", *8th International Workshop on Advanced Ground Penetrating Radar (IWAGPR)*, Florence, Italy, 2015.

[11] Arosio D., "Rock fracture characterization with GPR by means of deterministic deconvolution", *Journal of Applied Geophysics*, vol. 126, pp. 27–34, 2016.

[12] Basile V., Carrozzo M. T., Negri S., Nuzzo L., Quarta T., Villani A. V., "A ground-penetrating radar survey for archaeological investigations in an urban area (Lecce, Italy)", *Journal of Applied Geophysics*, vol. 44, no. 1, pp. 15-32, 2000.

[13] Bee Bednar J., "Modeling, Migration and Velocity Analysis in Simple and Complex Structure", 1st ed. Panorama Technologies, 2008.

[14] Bochud N., "Signal Processing-Based Identification of Pathology Using Ultrasonics", PhD Thesis, Universidad de Granada, 2014.

[15] Bodare A., "Non Destructive Test Methods of Cultural Stone", Published Report 3017, Division of Soil and Rock Mechanics, Department of Civil and Environmental Engineering, Royal Institute of Technology, Stockholm, 1996.

[16] Bostanudin N. J. F., "Computational Methods for Processing Ground Penetrating Radar Data", PhD Thesis, University of Portsmouth, UK, 2013.

[17] Bramanti M. and Bozzi E., "A procedure to detect flaws inside large sized marble rocks by ultrasound", *Subsurface Sensing Technologies and Applications*, vol. 2, pp. 1-13, 2001.

[18] Bristow C. S., "Ground Penetrating Radar", *Treatise on Geomorphology*, vol. 14, pp.183–194, 2013.

[19] Cagnoli B., Ulrych T., "Singular value decomposition and wavy reflections in ground-penetrating radar images of base surge deposits", *Journal of Applied Geophysics*, vol. 48, pp. 175-182, 2001.

[20] Carlson B., *Communications Systems, An Introduction to Signals and Noise in Electrical Communication*, McGraw-Hill International Editions, 3rd ed., pp. 196–199, 1986.

[21] Cerrillo C., Jiménez A., Rufo M., Paniagua J., Pachón F.T., "New contributions to granite characterization by ultrasonic testing", *Ultrasonics*, vol. 54, pp. 156–167 (2014).

[22] Daniels J. J., "Ground Penetrating Radar Fundamentals", Report Appendix to U.S.EPA, Region V, 2000.

[23] Daniels D. J., "Ground Penetrating Radar", 2nd ed. *The Institution of Electrical Engineers*, London, UK, 2004.

[24] Davis J. L., Annan A. P., "Ground-penetrating radar for high-resolution mapping of soil and rock stratigraphy", *Geophysical Prospecting*, vol. 37, pp. 531-551, 1989.

[25] Davis J., Heginbottom J., Annan A., Daniels R., Berdal B., Bergan T., Duncan K., Lewin P., Oxford J., Roberts N., Skehel J., Smith C., "Ground Penetrating Radar Surveys to Locate Spanish Flu Victims in Permafrost", *Journal of Forensic Sciences*, vol. 45, no. 1, pp. 68–76, 2000.

[26] Deparis J., Garambois S., Hantz D., "On the potential of Ground Penetrating Radar to help rock fall hazard assessment: A case study of a limestone slab, Gorges de la Bourne (French Alps)", *Engineering Geology*, vol. 94, pp. 89-102, 2007.

[27] Deparis J., Jongmans D., Fricout B., Villemin T., Meric O., Mathy A., Effendiantz L., "Characterization of the fracture pattern on cliff sites combining geophysical imaging and laser scanning", 1*0th International Symposium on Landslides and Engineered Slopes*, Xian, China, 2008.

[28] Der Merwe A. Gupta I., "A novel signal processing technique for clutter reduction in GPR measurements of small, shallow land mines", *IEEE*

Transactions on Geoscience and Remote Sensing, vol. 38, no. 6, pp. 2627-2637, 2000.

[29] Derovert X., Abraham O., "GPR and seismic imaging in a gypsum quarry", *Journal of Applied Geophysics*, vol. 45, pp. 157-169, 2000.

[30] De Domenico D., Campo D., Teramo A., "FDTD modelling in high-resolution 2D and 3D GPR surveys on a reinforced concrete column in a double wall of hollow bricks", *Near Surface Geophysics*, vol. 11, pp. 29–40, 2013.

[31] Doolittle J.A., Minzenmayer F.E., Waltman S.W., Benham E.C., Tuttle J.W., Peaslee S.D., "Ground-penetrating radar soil suitability map of the conterminous United States", vol. 141, no. 3-4, pp. 416-421, 2007.

[32] Dorn C., Linde N., Doetsch J., Le Borgne T., Bour O., "Fracture imaging within a granitic rock aquifer using multiple-offset single-hole and cross-hole GPR reflection data", *Journal of Applied Geophysics*, vol. 78, pp. 123–132, 2012.

[33] Falorni P., L. Capineri, L. Masotti, and G. Pinelli, "3-D radar imaging of buried utilities by features estimation of hyperbolic diffraction patterns in radar scans", *Proc. 10th Int. Conf. Ground Penetrating Radar*, Delft, The Netherlands, vol. 1, pp. 403–406, 2004.

[34] Forte E., Pipan M., "GPR Rock Mass Imaging and Characterization by Attenuation Analysis", *70th EAGE Conference and Exhibition*, Rome, Italy, 2008.

[35] Forte E., Pipan M., Casabianca D., Di Cuia R., Riva A., "Imaging and characterization of a carbonate hydrocarbon reservoir analogue using GPR attributes", Journal of Applied Geophysics, vol. 81, pp. 76-87, 2012.

[36] Francke J., "A review of selected ground penetrating radar applications to mineral resource evaluations", *Journal of Applied Geophysics*, vol. 81, pp. 29–37, 2012.

[37] Gazi A., Skevis G., Founti M. A., "Energy efficiency and environmental assessment of a typical marble quarry and processing plant", *Journal of Cleaner Production*, vol. 32, pp. 10–21, 2012.

[38] Gilmore C. G., "A Comparison of Imaging Methods using GPR for Landmine Detection and A Preliminary Investigation into the SEM for Identification of Buried Objects", PhD Thesis, University of Manitoba, Winnipeg, Manitoba, Canada, 2004.

[39] Gonzalez, M., Catapano, I., Soldovieri, F., "A comparative study of gpr reconstruction approaches for landmine detection", *IEEE Journal of Selected Topics in Applied Earth Observations and Remote Sensing*, vol. 7, no. 12, pp. 4869-4878, 2014.

[40] Grandjean G., Gourry J.C., "GPR data processing for 3D fracture mapping in a marble quarry (Thassos, Greece)". *Journal of Applied Geophysics*, vol. 36, pp. 19–30, 1996.

[41] Hoyer P., "Non-negative Matrix Factorization with Sparseness Constraints", *Journal of Machine Learning Research*, vol. 5, pp. 1457–1469, 2004.

[42] Hugenschmidt J., Kalogeropoulos A., Soldovieri F., Prisco G., "Processing strategies for high-resolution GPR concrete inspections", *NDTE International*, vol. 43, pp. 334-342, 2010.

[43] Jeannin M., Garambois S., Gregoire C., Jongmans D., "Multiconfiguration GPR measurements for geometric fracture characterization in limestone cliffs (Alps)", *Geophysics, Society of Exploration Geophysicists*, vol. 71, no. 3, pp. B85–B92, 2006.

[44] Jeng Y., Lin C., Li Y., Chen C. and Huang H., "Application of multiresolution analysis in removing ground penetrating radar noise", *CSPG CSEG CWLS Convention*, Calgary, Canada, pp. 416-419, 2009.

[45] Jol H. M., "Ground Penetrating Radar Theory and Applications", 1st ed. Elsevier Science, USA, 2008.

[46] Jolliffe I. T., Stephenson D. B., "Forecast Verification: A Practitioner's Guide in Atmospheric Science", 2nd Edition, 2011.

[47] Kadioglu S., "Photographing layer thicknesses and discontinuities in a marble quarry with 3D GPR visualisation", *Journal of Applied Geophysics*, vol. 64, pp. 109–114, 2008.

[48] Kana A. A., West L. J., Clarck R. A., "Fracture aperture and fill characterization in a limestone quarry using GPR thin-layer AVA analysis", *Near Surface Geophysics*, vol. 11, 1969.

[49] van Kempen L., Sahli H., "Signal processing techniques for clutter parameters estimation and clutter removal in GPR data for landmine detection", *Proceedings of the 11th IEEE Signal Processing Workshop on Statistical Signal Processing*, 2001.

[50] Khan U., Al-Nuaimy W., "Background removal from GPR data using Eigenvalues", *13th International Conference on Ground Penetrating Radar (GPR)*, Lecce, Italy, 2010.

[51] Kim J. H., Cho S., Yi M. J., "Removal of ringing noise in GPR data by signal processing", *Geosciences Journal*, vol. 11, no. 1, pp. 75, 2007.

[52] King B., Smaragdis P., Mysore G.J., "Noise-robust dynamic time warping using PLCA features", *Proceedings of the IEEE International Conference on Acoustics, Speech and Signal Processing*, Kyoto, Japan, 2012.

[53] Kittler J., Illingworth J., "Minimum error thresholding", *Pattern Recognition*, vol. 19, pp. 41-47, 1986.

[54] Knight R., "Ground Penetrating Radar for environmental applications", *Annu. Rev. Earth Planet. Sci*, vol. 29, pp. 229-55, 2001.

[55] Kong F. N., By T. L., "Performance of a GPR system which uses step frequency signals", *Journal of Applied Geophysics*, vol. 33, pp. 15–26, 1995.

[56] Longoni L., Arosio D., Scaioni M., Papini M., Zanzi L., Roncella R., Brambilla D., "Surface and subsurface non-invasive investigations to improve the characterization of a fractured rock mass", *Journal of Geophysics and Engineering*, vol. 9, pp. 461-472, 2012.

[57] Lualdi M., Zanzi L., "2D and 3D GPR imaging to map the fractures and to evaluate the integrity of limestone ornamental rocks", *Proceedings of the Symposium on the Application of Geophysics to Environmental and Engineering Problems (SAGEEP03)*, San Antonio, Texas, USA, pp. 613-622, 2003.

[58] Lualdi M., Zanzi L., "2D and 3D experiments to explore the potential benefit of GPR investigations in planning the mining activity of a limestone quarry", *Tenth International Conference on Ground Penetrating Radar*, Delft, The Netherlands, 21 -24 June, 2004.

[59] Luo Y., Fang G., "GPR Clutter Reduction and buried target detection by improved Kalman filter technique", *Proceedings of the Fourth International Conference on Machine Learning and Cybernetics*, Guangzhou, 2005.

[60] Luodes H., "Natural stone assessment with ground penetrating radar", *Estonian Journal of Earth Sciences*, vol. 57, n. 3, pp. 149–155, 2008.

[61] Mala geoscience (2017) [cited accessed: 2017-04-04], URL http://www.malags.com/home.

[62] Maxwell J.C., "A Treatise on Electricity and Magnetism", vol. 2, 1873.

[63] Meschede M., Asprion U., Reicherter K., "Visualization of tectonic structures in shallow-depth high-resolution ground-penetrating radar (GPR) profiles", *Terra Nova*, vol. 9, no. 4, pp. 167–170, 1997.

[64] Monga V., Mhcak M., "Robust and Secure Image Hashing via Non-Negative Matrix Factorizations", *IEEE Transactions on Information Forensics and Security*, vol. 2, pp. 376-390, 2007.

[65] Nadim G., "Clutter reduction and detection of landmine objects in ground penetrating radar data using likelihood method," *Third International Symposium on Communications, Control and Signal Processing*, pp. 98–106, 2008.

[66] Nam J., Mysore G.J., Smaragdis P., "Sound recognition in mixtures", *Proceedings of the international conference on Latent Variable Analysis/Independent Component Analysis*, Tel-Aviv, Israel, 2012.

[67] Neal A. "Ground-penetrating radar and its use in sedimentology: principles, problems and progress", *Earth Sci Rev*, vol. 66, pp. 261-330, 2004.

[68] Nielsen L., Von Brockforff A.S., Bjerager M., Surlyk F., "Three-dimensional architecture and development of Danian bryozoan mounds at Limhamn, south-west Sweden, using ground-penetrating radar", *Sedimentology*, vol. 56, pp. 695-708, 2009.

[69] Nobes D., "Geophysical surveys of burial sites: a case study of Oaro urupa", *Geophysics*, vol. 64, pp.357-367, 1999.

[70] Olhoeft, G.R., "Electrical properties of granite with implications for the lower crust", *Journal of Geophysical Research*, vol. 86, no. B2, pp. 931-936, 1981.

[71] Onur A.H., Bakrac S., "Determination of discontinuities in marble blocks via a nondestructive ultrasonic technique", *Int J Miner Metall Mater*, vol. 16, pp. 487-493, 2009.

[72] Onur A.H., Bakrac S., Karakus D., "Ultrasonic Waves in Mining Application", 1st ed. A. A. dos Santos, 2012.

[73] Orlando L., "Semiquantitative evaluation of massive rock quality using ground penetrating radar", *Journal of Applied Geophysics*, vol. 52, pp. 1-9, 2003

[74] Orlando L., Slob E., "Using multicomponent GPR to monitor cracks in a historical building", *Journal of Applied Geophysics*, vol. 67, pp. 327-334, 2009.

[75] Otsu N., "A Threshold Selection Method from Gray-Level Histograms", *IEEE Trans. Syst., Man, Cybern., Syst.*, Vol. SMC-9, No. 1, January 1979.

[76] Ozdemir C., Demirci S., Yigit E., "A Review on the Migration Methods in B-scan Ground Penetrating Radar Imaging", *Progress in Electromagnetics Research Symposium Proceedings*, KL, Malaysia, pp. 27–30, 2012.

[77] Pasolli E., Melgani F., Donelli M., "Automatic Analysis of GPR Images: A Pattern-Recognition Approach", *IEEE Transactions on Geoscience and Remote Sensing*, vol. 47, no. 7, 2009.

[78] Perez-Gracia V., Di Capua D., Gonzlez-Drigo R., "GPR resolution in Cultural Heritage applications", *13th International Conference on Ground Penetrating Radar (GPR)*, Italy, 2010.

[79] Peters L. P., Daniels J. J., Young J. D., "Ground penetrating radar as a subsurface environmental sensing tool", *Proceedings of the IEEE*, vol. 82, no. 12, 1994.

[80] Pettinelli E., Di Matteo A., Mattei E., Crocco L., Soldovieri F., Redman J. D., Annan A. P., "GPR Response from buried pipes: Measurement on field site and tomographic reconstructions," *IEEE Transactions on Geoscience and Remote Sensing*, vol. 47, no. 8, pp. 2639–2645, 2009.

[81] Pipan M., Baradello L., Forte E., Prizzon A., "GPR study of bedding planes, fractures and cavities in limestone", *The International Society for Optical Engineering*, 2000.

[82] Porsani J. L., Sauck W. A., Junior A. O. S., "GPR for mapping fractures and as a guide for the extraction of ornamental granite from a quarry: A case study from southern Brazil", *Journal of Applied Geophysics*, vol. 58, pp. 177-187, 2006.

[83] Potin D., Duflos E., Vanheeghe P., "Landmines Ground-Penetrating Radar Signal Enhancement by Digital Filtering", *IEEE Transactions on Geoscience and Remote Sensing*, vol. 44, no. 9, 2006.

[84] RadExplorer Software, MALA GeoScience, 2017, URL: *http://www.malags.com/products/mala-radexplorer* [accessed: 2017-20-04].

[85] Rashed M., Harbi H., "Background matrix subtraction (BMS): A novel background removal algorithm for GPR data", *Journal of Applied Geophysics*, vol. 106, pp. 154–163, 2014.

[86] Rashed E.A., "GPR background removal using a directional total variation minimisation approach", *Journal of Geophysics and Engineering*, vol. 12, pp. 897-908, 2015.

[87] ReflexW Software, Sandmeier Geophysical Research, 2017, URL: *http://www.sandmeier-geo.de/reflexw.html* [accessed: 2017-20-04].

[88] Rial F. I., Pereira M., Lorenzo H., Arias P., Novo A., "Vertical and Horizontal Resolution of GPR bow-tie antennas", *4th International Workshop on Advanced Ground Penetrating Radar*, Italy, 2007.

[89] Robinson M., Bristow C., McKinley J., Ruffell A., "Ground Penetrating Radar", *Geomorphological Techniques*, Part 1, Sec. 5.5, 2013.

[90] Roch K. H., Chwatal W., Bruckl E., "Potentials of monitoring rock fall hazards by GPR: considering as example the results of Salzburg", *Landslides*, vol. 3, pp. 87–94, 2005.

[91] Rodriguez-Abad I., Martinez-Sala R., Capuz Lladr R., Dez Barra R., Garca-Garca F., "Assessment of the variation of the moisture content in the Pinus pinaster Ait using the non destructive gpr technique", *Materiales de Construccion*, vol. 61, no. 301, pp. 143–156, 2011.

[92] Sadri A., "Application of impact-echo technique in diagnoses and repair of stone masonry structures", *NDTE International*, vol. 36, pp. 195-202, 2003.

[93] Saez-Perez M.P., Rodriguez-Gordillo J., "Structural and compositional anisotropy in Macael marble (Spain) by ultrasonic, x-rd XRD and optical microscopy methods", *Constr Build Mater*, vol. 23, pp .2121–2126, 2009.

[94] Saleh B., "Introduction to Subsurface Imaging", *Cambrigde University Press*, 1st Ed., 2011.

[95] Sambuelli L., "Estimation of thin fracture aperture in a marble block by GPR sounding", *Bollettino di Geofisica Teorica ed Applicata*, vol. 51, no. 2, pp.239–252, 2010.

[96] Sarpun I.H., Kilickaya M.S., "Mean grain size determination in marbles by ultrasonic first backwall echo height measurements", *NDTE Int*, vol. 39, pp. 82–86, 2006.

[97] Schneider W.A, "Integral formulation for migration in two and three dimensions", *Geophysics*, vol. 43, pp. 49–76, 1978.

[98] Scott A. H., "Dielectric constant, power factor, and resistivity of Marble", *Part of Journal of Research of the National Bureau of Standards*, March 1940.

[99] Sengodan A., Cockshott W. P., Cuenca-Garcia C., "The SIMCA algorithm for processing Ground Penetrating Radar data and its use in locating foundations in demolished buildings", *IEEE Radar Conference (RADAR)*, 2011.

[100] Sengodan A., Cockshott W. P., Cuenca-Garcia C., "A 3D reconstruction algorithm for the location of foundations in demolished buildings", *7th European Conference on Antennas and Propagation*, 2013.

[101] Sengwa R. J., Soni A., "Low-frequency dielectric dispersion and microwave dielectric properties of dry and water-saturated limestones of the Jodhpur region", *Geophysics*, vol. 71, no. 5, pp. 269-277, 2006.

[102] Sezgin M., "Two dimensional Template Matching method for buried object discrimination in GPR data", *Proceedings of SPIE - The International Society for Optical Engineering 7303*, 2009.

[103] Shkolnikov Y., "Weighted principal component analysis for real-time background removal in GPR data", *Proc. SPIE 8357, Detection and Sensing of Mines, Explosive Objects, and Obscured Targets XVII*, 2012.

[104] Sigurdsson T., "Ground penetrating radar for geological mapping", PhD Thesis, Arhus University, Arhus Geoscience, 1995.

[105] Sigurdsson T., Overgaard T., "Application of GPR for 3-D visualization of geological and structural variation in a limestone formation", *Journal of Applied Geophysics*, vol. 40, pp. 29–36, 1998.

[106] Smaragdis P., Raj B., "Shift-Invariant Probabilistic Latent Component Analysis", Tech report, 2007.

[107] Smaragdis, P., Raj, B., Shashanka, M.V., "Supervised and Semi-Supervised Separation of Sounds from Single-Channel Mixtures", *Proceedings of the 7th International Conference on Independent Component Analysis and Signal Separation*, London, UK, September 2007.

[108] Solimene R., Cuccaro A., DellAversano A., Catapano I., Soldovieri F., "Ground Clutter Removal in GPR Surveys", *IEEE Journal of Selected Topics in Applied Earth Observations and Remote Sensing*, vol. 7, no. 3, 2014.

[109] Stolt R.H. "Migration by Fourier Transform", *Geophysics*, vol. 43, no. 1, pp. 23–48, 1978.

[110] Stolt R.H., Weglein A.B., "Migration and inversion of seismic data", *Geophysics*, vol. 50, no. 12, 1985.

[111] Sweeney J. J., Roberts J. J., Harben P. E., "Study of Dielectric Properties of Dry and Saturated Green River Oil Shale", *Energy and Fuels*, vol. 21, pp. 2769–2777, 2007.

[112] Theune U., Schmitt D., Sacchi M., "Looking inside Turtle Mountain: Mapping fractures with GPR", Geophysical Institute, Department of Physics, University of Alberta, Edmonton, Alberta, 2005.

[113] Tillard S., Dubois J. C., "Analysis of GPR data: wave propagation velocity determination", *Journal of Applied Geophysics*, vol. 33, pp. 77–91, 1995.

[114] Ting-jun L., Zheng-ou Z., "Fast Extraction of Hyperbolic Signatures in GPR", *International Conference on Microwave and Millimeter Wave Technology*, pp. 1–3, 2007.

[115] Tjora S., Eide E., Lundheim L., "Evaluation of Methods for Ground Bounce Removal in GPR Utility Mapping", *Tenth International Conference on Ground Penetrating Radar*, Delft, The Netherlands, June, 2004.

[116] Toshioka, T., Tsuchida, T., Sasahara, K., "Application of GPR to detect and map cracks in rock slopes", *Journal of Applied Geophysics*, vol. 33, pp. 119-124, 1995.

[117] Tsoflias G. P., Van Gestel J. P., Stoffa P. L., Blankenship D. D., Sen M., "Vertical fracture detection by exploiting the polarization properties of ground-penetrating radar signals", *Geophysics*, vol. 69, no. 3, pp. 803-810, 2004.

[118] Ulaby F., Dobson M.C., Garvin J.B., "Microwave Dielectric Properties of Dry Rocks", *IEEE Transactions on Geoscience and Remote Sensing*, vol. 28, no. 3, 1990.

[119] Vaccaneo D., Sambuelli L., Marini P., Tascone R., Orta R., "Measurement System of Complex Permittivity of Ornamental Rocks in L Frequency Band", *IEEE Transactions on Geoscience and Remote Sensing*, vol. 42, no. 11, 2004.

[120] Valle S., Zanzi L., Sgheiz M., Lenzi G., Friborg J., "Ground Penetrating Radar Antennas: Theoretical and Experimental Directivity Functions", *IEEE Geosci. Remote Sens.*, vol. 39, no. 4, 2001.

[121] Vergara L., Gosalvez J., Fuente J. V., Miralles R., Bosch I., Salazar A., López A.M., López L.E., "Ultrasonic nondestructive testing on marble rock blocks", *Materials Evaluation*, 2002.

[122] Vuksanovic B., Bostanudin N., Hidzir H., Parchizadeh H., "Discarding Unwanted Features from GPR Images Using 2DPCA and ICA Techniques", *International Journal of Information and Electronics Engineering*, vol. 3, no. 3, 2013.

[123] Xia J., Franseena E. K., Millera R. D., Weisb T. V., Byrnesa A. P., "Improving ground-penetrating radar data in sedimentary rocks using deterministic deconvolution", *Journal of Applied Geophysics*, vol. 54, pp. 15-33, 2003.

[124] Yelf R.J., Al-Nuaimy W. "Classification System for GPR Parameters", *Proc. of the 10-th International GPR Conference*, Delft University, Netherlands, pp. 407410, 2004b.

[125] Yelf R. J., "Application of Ground Penetrating Radar to Civil and Geotechnical Engineering", *Electromagnetic Phenomena*, vol. 7, no 18, 2007.

[126] Yilmaz O., "Seismic Data Processing", *SEG*, 1987.

[127] Young R. and Sun J., "Revealing stratigraphy in ground penetrating radar data using domain filtering", *Geophysics*, vol. 64, pp. 435-442, 1999.

[128] Zhao A., Jiang Y., Wang W., "Exploring Independent Component Analysis for GPR Signal Processing", *Electromagnetics Research Symposium*, Hangzhou, China, pp. 1-4, 2005.

[129] Zhu J., Lines L. R., Gray S. H., "Smiles and frowns in migration/velocity analysis", *CREWES Research Report*, vol. 9, 1997.

[130] Zoubir A., Chant I., Brown C., Barkat B., Abeynayake C., "Signal processing techniques for landmine detection using impulse ground penetrating radar," *IEEE on Sensors Journal*, vol. 2, pp. 41–51, 2002.

Paper A

Ground-penetrating radar method used for the characterisation of ornamental stone quarries

Rey J., Martínez J., Vera P., Ruiz N., Cañadas F., Montiel V., "Ground-penetrating radar method used for the characterisation of ornamental stone quarries", in *Construction and Building Materials*, vol. 77, pp. 439-447, 2015.

Abstract

In the work non-destructive ground-penetrating radar (GPR) was used to probe the texture and presence of anisotropies in different types of carbonated rocks intended for ornamental use.

First, GPR on the different facies of a marble quarry in Macael (Almera, Spain) was applied where alternating layers of marble and mica schists can be found. GPR allows for the differentiation of the marble units from the mica schist units, which makes GPR a good tool for indirectly evaluating the reserves in a deposit. In addition, it allows for the detection of the different anisotropies in the marble units (holes, fractures), and this information could be utilised to formulate a work-plan design. Antennae of different frequencies were employed (100, 250 and 800 MHz) for these purposes, and the 250 MHz antenna had the most effective probing capacity for obtaining an accurate depth resolution.

Second, a GPR study was conducted in three types of rock known commercially as Macael Marble, Crema Marfil and Red Travertine before the block-cutting process. For this configuration, the 800 MHz antenna was used to differentiate the textures of each type of rock as well as the location of a variety of anisotropies, and the results showed that GPR is an effective tool for evaluating the block quality, determining whether resins must be injected to consolidate the block and estimating the orientation of the cutting process.

In the work, the use of a supervised two-dimensional (i.e., radargram) probabilistic latent component analysis (PLCA) approach is proposed to highlight only the information from target objects (i.e., marble anisotropy) provided by the radargram, which facilitates the data interpretation by the user. This approach can search activations of the georadar pulse across both dimensions. Once the analysis has been performed, a variable-gain compensation process is proposed to outperform the energy losses that result from the reflections of the signal when a different material is found.

The results have shown that the GPR method can be utilised as a tool for the diagnosis of stone materials prior to their use in artistic work or monuments; therefore, GPR may be considered a technique for material selection. The presence of discontinuities (sometimes visible to the naked eye)

explain many of the phenomena and typologies of the stone after its eventual alteration, and such discontinuities could be avoided by means of this pre-emptive work.

Key words: *Ground-penetrating radar, discontinuity, marble quarry, non-destructive test, Macael*

1 Introduction

Determining the texture of stone and spatial distribution of structural discontinuities, such as cavities, fractures, foliations, etc., is of utmost importance for the design of work plans and subsequent exploitation of quarries. The texture characterisation of the deposit, identification of weakness zones, and possible cartographic description of such zones by means of indirect techniques could assist in the calculation of reserves and design of the advance faces of a quarry, which would reduce extraction costs.

In addition, the evaluation and characterisation of extracted blocks by non-destructive techniques is a necessity because it allows for the location and sizing of possible defects or imperfections within the block (cracks, fractures, holes, etc.), which could maximise the exploitation of the blocks with a subsequent increase in profitability and reduction of the environmental impact of the material processing industry.

Previous works have analysed non-destructive characterisation techniques for stone materials. Sarpn and Kilickaya [20] utilised ultrasonic relative attenuation (URA) to estimate the grain size in marble and obtained similar results to that of conventional optical methods. However, ultrasonic transmission techniques have also been utilised for the study of mineralogical composition as well as for the characterisation of structural discontinuities in ornamental rocks ([19] [17]). Recently, Cerrillo et al. [3] obtained good results with statistical linear correlations between the parameters of ultrasound techniques and physical and mechanical properties of granite. Therefore, these authors consider this technique to be of great use for the study of granite material.

Ground-penetrating radar (GPR) is a non-destructive technique that has been widely used, and Sigurdsson [22] performed the first studies in limestone quarries to conduct lithographic characterisations. Sigurdsson and Overgaard [23] studied limestone with GPR (using a 100 MHz antennae),

which allowed them to differentiate zones with textural variations (bryozoan limestone, coral limestone and wackestone). Grandjean and Gourry [5] and Kadioglu [9] applied this technique for the detection of fractures in marble quarries in Greece and Turkey, respectively, Lualdi and Zanzi [12] and Arosio et al. [1] in Italy and Porsani et al. [18] used these techniques on granite quarries in Brazil.

The work proposes to apply the GPR technique as a non-destructive analysis technique for the evaluation and characterisation of stone materials. GPR was applied to the material from the beginning of the exploitation process, i.e., from its extraction from the quarry. It is our intention to determine the usefulness of GPR at this initial phase to evaluate the stone deposit and locate the fracturing, stratification and schist contents of the massifs to be exploited. This application would allow for an assessment of profitability, as well as for the optimisation of the traditional exploitation criteria.

Once the blocks have been extracted, it would be helpful to determine their internal structure (fissures, cavities, layers, etc.) before initiating the process of block rolling. Based on the information provided by these non-destructive techniques, it would be possible to evaluate whether the block must be consolidated by means of resins or other components, establish injection points (if consolidations is necessary) and optimise the process of cutting or lamination of the block. Thus, a more efficient exploitation of the material and reduction of residues would be achieved. We aim to determine the usefulness of GPR techniques at this phase.

However, detecting a true discontinuities remains a challenging problem in the field of the GPR. Although there are numerous processing algorithms used in commercial GPR systems (e.g., background removal, [10] [27]), most provide data that must be interpreted in terms of the experience of the user. To minimise the errors produced by an incorrect interpretation by the user, probabilistic latent component analysis (PLCA) has been demonstrated to be a useful tool for denoising or separating targets from non-target sources ([15] [11]).

Moreover, the presence of discontinuities and structural defects in stone materials explains many of their phenomena and typologies witnessed after alteration. Such phenomena and defects are important for art work and monuments, but because they cannot always be detected by plain sight,

GPR techniques could be used for the selection of material in advance or for the subsequent detection of anomalies and defects.

2 Geological setting

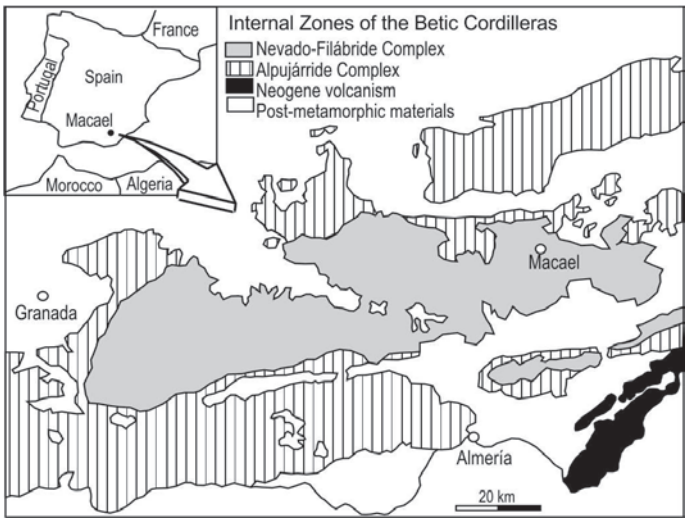

Figure 1: Simplified geological map of the inner zones of the Baetic System showing the location of the studied region (from Torres-Ruiz et al. [29]).

The first phase of the study was developed in the marble quarries near the town of Macael, Spain (Fig. 1). In geological terms, these materials belong to the inner zones of the Baetic System, and specifically to the Nevado-Filbride Complex ([8]). This unit composes the lowest tectonic complex of the set of overlapping folds of the inner zones (Penibaetic System), which surfaced because of a tectonic window under the materials of the Alpujrride Complex ([29]).

Different units formed concurrently at the Nevado-Filbride complex and underwent high-pressure and low-temperature-gradient metamorphism processes, followed by other higher-thermal-gradient processes. Carbonated rocks from the Late Triassic period are the characteristic materials of this formation, although layers of these carbonated rocks can be found alternating with layers of mica schists, calcareous mica schists, quartzitic mica schists with garnet and amphibole ([13]). The subsequent metamorphism and deformation experienced by the materials are associated with the Alpine

orogeny ([8] [29]).

The material used in quarries is a marble of granoblastic type that varies from equigranular with large grains to fine-grained heterogeneous. In addition, the marble contains small quantities of quartz and isolated muscovite and feldspar. In all marbles, a roughly marked foliation is observed that is associated with variations in grains size, certain orientations of calcite crystals and the orientation of the existing phyllosilicates.

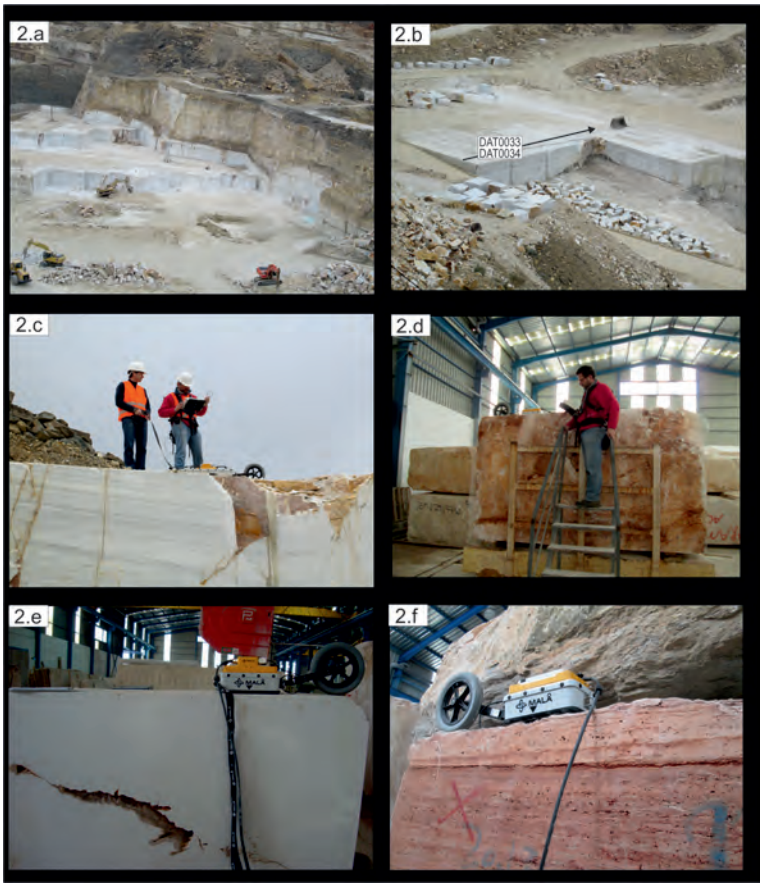

Figure 2: Photographic prints. General view of the Macael quarry under study (2a). Location of the profiles of Fig. 3 (2b). Details of the data collection using the 250 MHz antenna (2c). Study of blocks prior to the rolling process (2d). Study of a block of Crema Marfil with visible cavities; its GPR response is used for comparison purposes (2e). Study of a block of Red Travertino using the GPR technique; an evident horizontal layering is observed (2f).

Although the study is centred on white-coloured marble quarries (Fig.

2a, 2b and 2c), which are known commercially as *White Macael*, in the extraction district of Macael, there are two other marble varieties: *Tranco White* and *Yellow Triana*. These two varieties belong to the tectonic unit known as Nevado-Lubrn, whereas the *White Macael* belongs to the Bdar-Macael tectonic unit ([13]).

In the second phase, after block extraction, two other types of carbonated lithologies extracted from other locales were employed, in addition to the marbles mentioned above: clear limestone and red limestone. Clear limestone is commercially known by its Spanish name *Crema Marfil* (*White Ivory*) and consists of biomicrites (packstone) in which benthic foraminifera predominate (orbitoids and nummulits); stilolythic surfaces and diagenetic cementation processes are frequent as secondary structures (Figs. 2d and 2e).

Highly porous red limestone, which is commercially known as *Red Travertino*, was also used; this material presents characteristic banding, with well-developed and frequent cavities that are partially filled by calcite crystals (Fig. 2f). This rock was selected because, in addition to its high ornamental value, the anisotropies pose serious problems for the exploitation of this material from quarries and its eventual cutting.

3 GPR data acquisition and processing

The GPR technique was used as an electromagnetic prospection method. This is a non-destructive method based on the study of the propagation of high-frequency (in the range of 100 MHz to 1 GHz) electromagnetic waves, and the devices consist of an emitting antenna that is moved across the terrain (Fig. 2) while emitting short pulses. When these waves propagate through the boundary between two regions of different dielectric constants, the wave is reflected toward the surface, where its characteristics are measured by a receiving antenna. The penetration depth and resolution depend on the electromagnetic properties of the materials through which the waves propagate, as well as the antenna being utilised ([4]). Wave propagation through the subsoil is diminished as the terrain conductivity increases or signal frequency increases.

In general, the signals tend to be rapidly attenuated, so this technique is often employed for shallow-depth investigations. In low-conductivity ma-

terials such as carbonates, however, the signal attenuation is low, making these materials ideal for probing with the GPR method ([21] [6]).

For the same profile, an improved resolution with shallower penetration is achieved if higher-frequency antennae are employed, whereas the opposite results are obtained for low frequencies ([4]). The equipment used to conduct this study was a Pro-Ex model RAMAC/GPR system manufactured by MALA GeoScience (Mala, Sweden).

Shielded antennae of 100 and 250 MHz were used for all tests, and an antenna at 800 MHz was used for the studies of the quarry faces to be exploited. Subsequently, higher-frequency antennae at approximately 800 MHz were used on the blocks that were already extracted.

The operating parameters for the Pro-Ex Mala GPR system were selected as follows: nominal frequency 100, 250 and 800 MHz; time window 410, 185 and 47 s (with 100, 250 and 800 MHz frequency, respectively); point interval 0.03 m; sampling frequency 1100, 2610 and 7964 (with 100, 250 and 800 MHz frequency, respectively); and radar velocity 100 mm/s. The radar velocity is experimentally estimated from the obtained data of each block. The procedure to estimate the radar velocity for each dielectric block is the following: the thickness of the block and the travel time of the radargram wave along the block are experimentally measured, with both values (distance and time) the radar velocity is then estimated.

First, a variety of processing tools, including filtering and gain following, were applied to the radargrams obtained from the field ([2] [16]). The filtering and interpretation of the signal were conducted using the RAMAC GroundVision and Rad Explorer programs.

Standard band-pass filtering and gain correction as well as background removal were applied to the data. However, a new processing method based on the PLCA approach with energy compensation was proposed.

4 Image enhancement

The decomposition of a matrix to improve or highlight a specific source has been used widely in the field of image processing ([7] [14]) and audio processing (using the signal spectrogram) ([15] [11] [24], [28] [25] [26]).

A supervised PLCA approach ([26]) is used here to improve the image quality of the signal that is provided by the georadar, which facilitates data

interpretation by the user. Specifically, we apply a shift-invariance PLCA to two-dimensional data (radargram) in which the dimensions x (distance) and y (depth) are designated as the left-right and up-down dimensions, respectively. The purpose of the algorithm is to search for activations of the georadar pulse across both dimensions. The algorithm has two inputs: the radargram (its absolute value) and the pattern of the pulse transmitted by the georadar.

The proposed signal model is defined using a two-dimensional convolution (shift-invariance PLCA) ([26]):

$$P(x,y) = \sum_{z} P(z) \int \int P(\tau_x, \tau_y|z) P(x - \tau_x, y - \tau_y|z) d\tau_x d\tau_y \tag{1}$$

where $P(x,y)$ is the radargram, z is a latent variable, $P(z)$ is an N-dimensional distribution of the random variable; $P(\tau_x, \tau_y|z)$ is the kernel distribution (i.e., the pattern of the transmitted pulse) and $P(x-\tau_x, y-\tau_y|z)$ is the impulse distribution (i.e., the distance-depth coordinates (x,y) into the radargram image) where the kernel distribution is active. A sparseness constraint is applied to the impulse distributions to minimise the activation of patterns that can be simultaneously active in the radargram. As an example, Fig. 3 (bottom left) shows an input image composed of two different kernel distributions (Fig. 3 top middle right) at different positions. The two kernel distributions are the two different patterns of the input image. Once the input image decomposition has been computed, the priors $P(z_i)$ (Fig. 3 top left) indicate the amount of energy consumed by each pattern. The reconstructed image (Fig. 3 bottom right) is approximately equal to the input image and impulse distributions (Fig. 3 middle), which are represented by spikes and show the positions in which each kernel distribution is located in the input image so that the proper decomposition is performed.

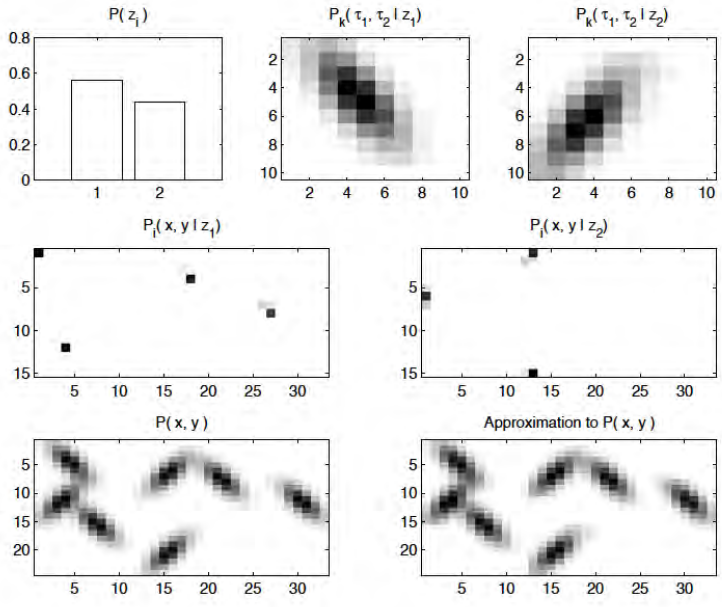

Figure 3: A shift invariant PLCA approach using convolution. The top plots display the latent variable priors to the left, whereas the remaining two plots display the two kernel distributions that were extracted. The second-row plots display the impulse distributions, whereas the bottom-row plots display the original input distribution on the left and model approximation on the right. ([26])

Once the decomposition has been computed, a variable-gain compensation process is applied to each column of the output of the PLCA to compensate for the energy losses that result from the objects reflecting the signal when a different material is found. In this process, we have assumed that the energy of each transmitted pulse is approximately equal because the georadar transmits the same pulse to each frame independently of the reflections that occur from the beginning to the end of the analysed material. This variable-gain compensation avoids the affect of early reflections at depth on the signal amplitude of the next reflections for the same distance.

5 Results and interpretation

Profiles were obtained at the quarry faces (Fig. 2b) using the different antennae (100, 250 and 800 MHz). In Fig. 4, it is possible to compare the results obtained from a specific profile with an 800 MHz (top panel) and 250

MHz (lower panel) antenna. The greater investigation depth was observed for the 250 MHz antenna, which reached more than 5 m, whereas the 800 MHz antenna barely reached 2 m and had a less-than-remarkable increase in detail. Therefore, the 250 MHz antenna appeared to be best suited for our investigation of the quarry.

The study of the quarry faces allows the correlation of geological data that are observed in the field with data from the GPR method, and such correlations can verify the effectiveness of the technique. In the sample radargram shown in Fig. 4, it is possible to distinguish two units: a generally massive upper unit (marble) and a lower unit (mica schists). The lepidoblastic texture of the mica schists is evidenced in the radargram by the banding characteristics of the signal, which are in contrast to the granoblastic texture of the marble. As verified by both the surfacing and radargram, the contact between these two lithologies is irregular. Thus, we conclude that the radargram is an effective tool for identifying the limits of the lithological units and evaluating the power and morphology of the geological bodies to be exploited.

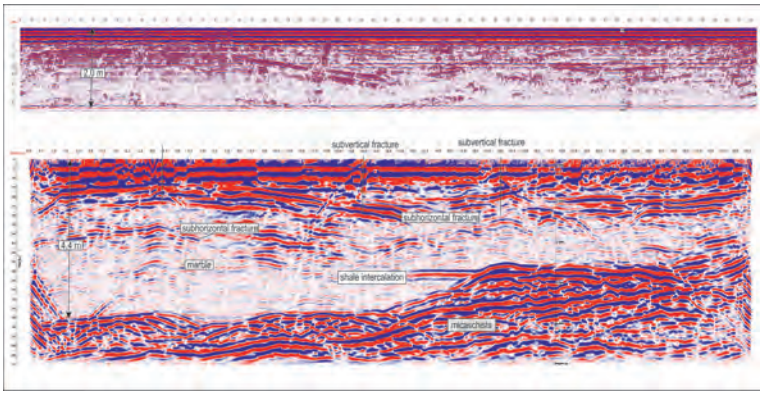

Figure 4: Radargram of the quarry faces obtained with an 800 MHz antenna (top of the figure) and 250 MHz antenna (bottom of the figure). With a 250 MHz antenna, the distinct behaviour of the mica schists and marbles stands out, which allows them to be distinguished in the radargram. In addition, sub-vertical and horizontal fractures also appear.

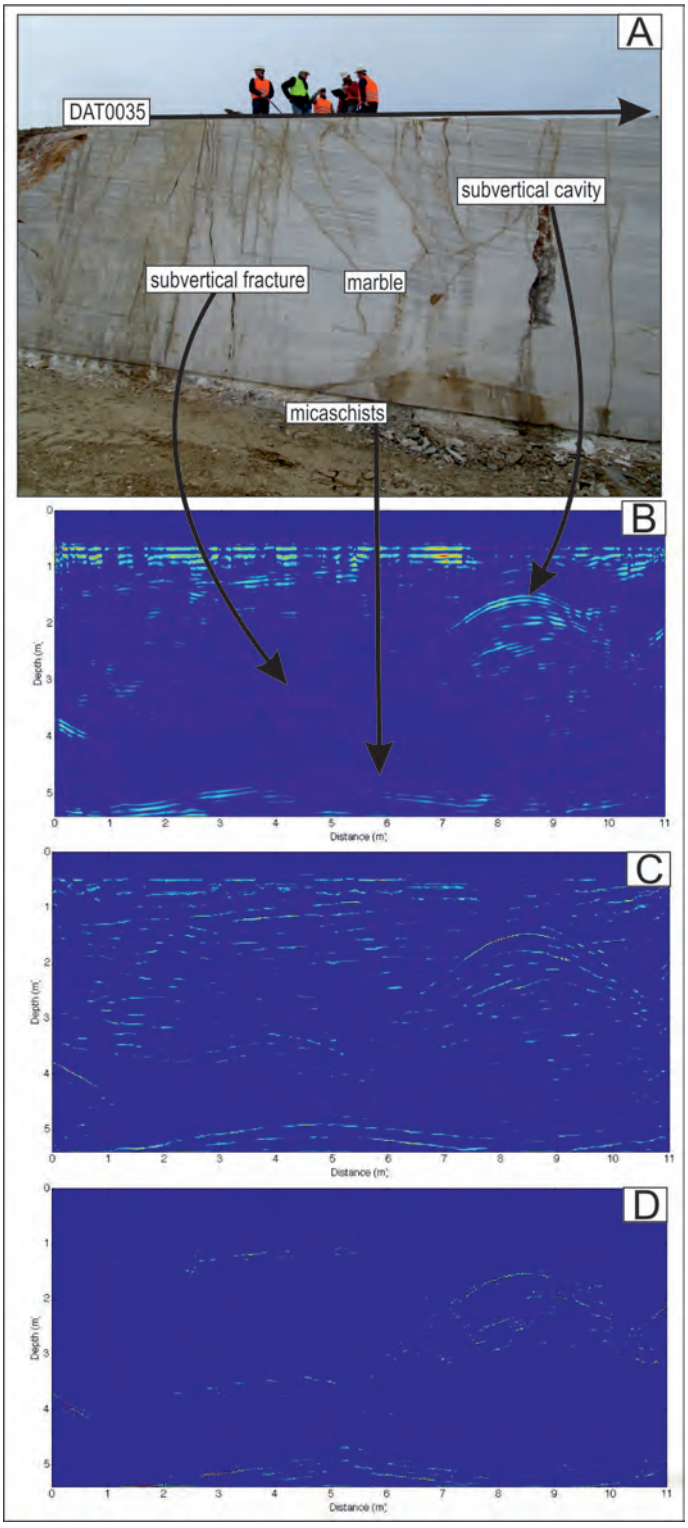

Figure 5: Details of the DAT0035 profile. Data collection from the quarry faces. (A). Radargram processed using the Rad Explorer package (B). The anisotropies observed in the field can be correlated with the results from the GPR technique (with a 250 MHz antenna). (B) Original radargram obtained using georadar. (C) Original radargram processed using the proposed PLCA 2D algorithm (D). Original radargram processed with the proposed PLCA 2D algorithm and variable gain, which compensates for energy losses.

In addition, both Fig. 4 and Fig. 5 (detail level) demonstrate the efficacy of using georadar for the detection of discontinuities (fractures and hollows) in the marble mass. In general, sub-vertical fractures are usually more challenging to detect. When they are detectable because of their span, the presence of hyperbolae stands out (Fig. 5B). Sub-horizontal fractures are usually easier to locate by means of the GPR technique (Fig. 5A). Fig. 5B shows the original radargram originating from the georadar, and each anisotropy is signalled as a reflected wave similar to the pulse transmitted by the georadar. As a result, it is difficult to clearly distinguish anisotropies located close to each other because a large amount of reflected energy is produced in a small spatial region. Another issue is that the pulse energy dies out quickly with depth as additional reflections are produced at material boundaries, making the large-depth anisotropies difficult to detect, even with a significant amount of energy. The proposed algorithm based on PLCA with energy compensation (Fig. 5c) minimises the inconveniences described above. The deconvolution conducted by the PLCA algorithm neatly shows the reflections produced on every anisotropy and allows for a clearer reading of the radargram. However, compensating for the energy lost through reflections improves the visibility of the wave throughout the depth of the material being studied. Thus, despite the occurrence of shallow-depth reflections, possible anisotropies can still be detected at greater depths because of the energy compensation. One example of this improvement can be observed in the anomaly located at an approximate depth of 3 m and distance of 4 m. In addition, the results of applying the PLCA algorithm with the sparseness restriction are shown (Fig. 5d). Applying this variation eliminates the radargram noise, leaving only the radargram zones where there is a high probability of an anomaly, although there is a drawback that occurs in the production of discontinuities in the lines that present reflections. However, this loss of continuity is not a determining factor, and complementary information is shown in Figs. 5c and 5d. Thus, once the zones with a high probability of anomalies have been detected (Fig. 5d), the user can rely on Fig. 5c for finer details on the information on the zone of interest.

The GPR technique has been applied to extracted blocks of the three types selected of carbonates, White Macael, Crema Marfil and Red Travertino, using the 800 MHz antenna. The former two show similar radargram patterns when the rock presents no defects. However, the anisotropy that the

Red Travertino presents in favour of fenestral porosity and partially filled cavities is evident to GPR techniques (compared with the radargram of Figs. 6 and 7).

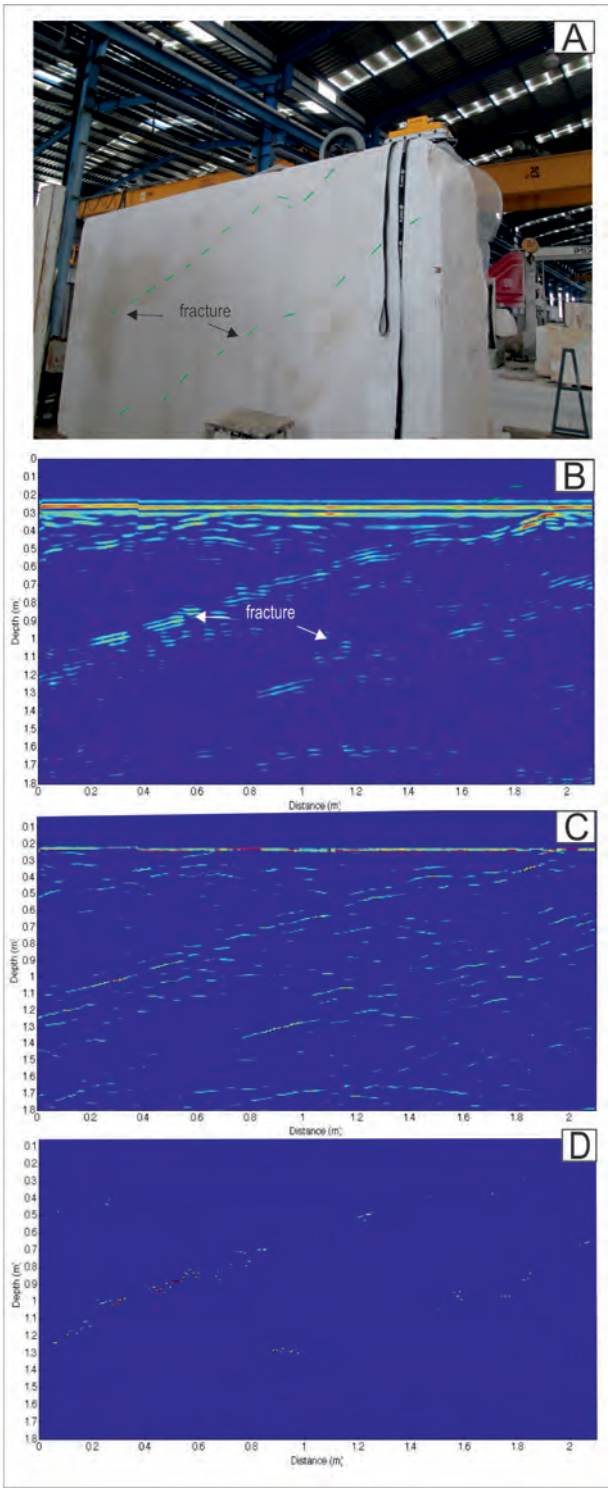

Figure 6: Details of the DAT0017 profile. The data were collected from a Crema Marfil block prior to the rolling process; certain anisotropies can be detected by plain sight (A). The profile (with an 800 MHz antenna) processed with the Rad Explorer package (B). Original radargram obtained from the georadar (C). Original radargram processed using the proposed PLCA 2D algorithm (D). Original radargram processed using the PLCA 2D algorithm and variable gain, which compensates for energy losses.

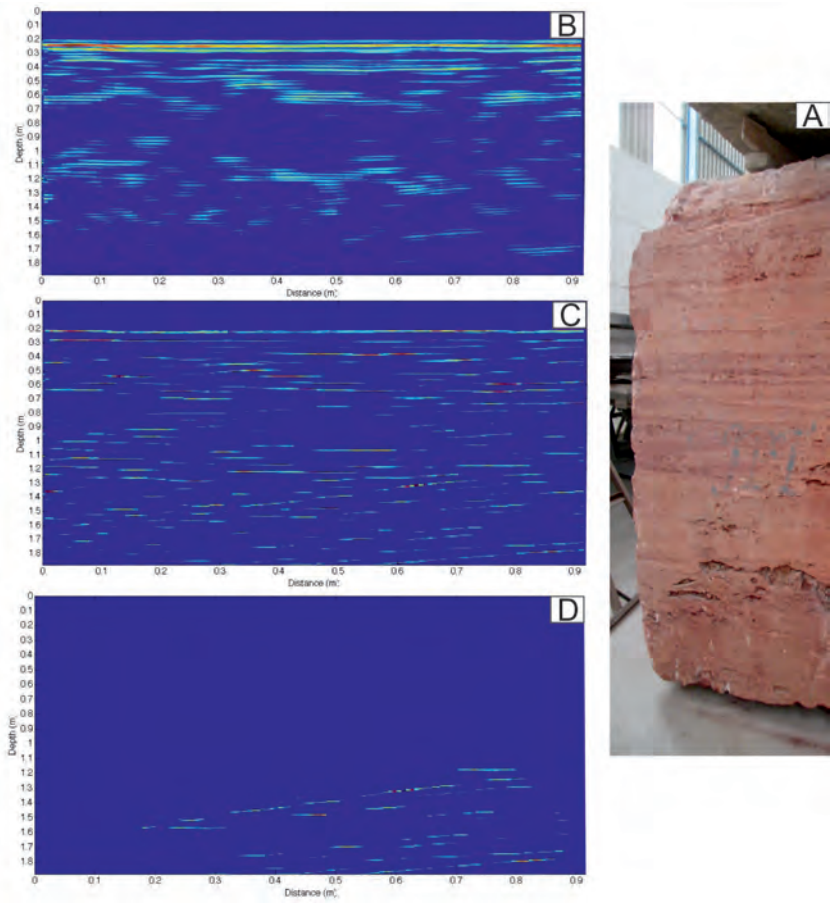

Figure 7: Details of the DAT0022 profile. (A) Block of Red Travertino from which the data were collected and anisotropies were detected by plain sight (banded). The profile (with an 800 MHz antenna) processed using the Rad Explorer package, (B) Original radargram obtained from the georadar. (C) Original radargram processed using the proposed PLCA 2D algorithm (D). Original radargram processed using the proposed PLCA 2D algorithm with variable gain, which compensates for energy losses.

From the performed test, the GPR technique has been shown to be capable of detecting small fractures and even stylolite surfaces present in the extracted blocks (Fig. 7), making it a viable characterisation technique that can be used prior to the cutting process. In relation to the size of fractures to detect, we should be able to obtain signal for those fractures with a length (in the perpendicular direction of the wave propagation) less than the wavelength of the radar wave in the dielectric. For example, the radar velocity of the dielectric of 9 is 100 mm/ns, and with a frequency of

800 MHz, this results in a wavelength of 12.5 cm.

Considering Figs. 6 and 7, the proposed image cleaning algorithm behaves similarly to Fig. 5. For both Figs. 6 and 7, the PLCA algorithm with energy compensation shows a higher amount of detail through deconvoluting the reflected pulse, which is signalled as a decrease in pulse length. Simultaneously, the energy compensation allows for the improved detection of objects at greater depths by increasing the energy of the reflected waves. However, it can be observed that Fig. 7 is less trustworthy for such detection, which might be a result of the high porosity of the Red Travertino. This potential for the detection of anisotropies can also be used as a tool for the characterisation of the quality of stone materials that are used in monuments and works with stringent quality requirements.

6 Conclusions

This work has demonstrated that the ground-penetrating radar (GPR) technique provides complementary high-resolution information for the determination of texture and structural anisotropies in ornamental stones such as marble and travertine.

The tests were conducted in carbonates with 100 MHZ, 250 MHZ and 800 MHz antennae. These stones are characterised by low conductivity, which is reflected in a low signal attenuation. By using 250 MHz antennae, it is possible to investigate depths of up to 6 m.

These studies were conducted in quarries at Macael, Spain, where layers of marble alternating with mica schists are exploited. GPR studies with 250 MHz antennae allow for a clear differentiation of the marble masses from the underlying mica schists, making GPR a promising tool for the indirect study of volume measurements of these types of deposits.

For the design of the quarry advance faces, the principal discontinuities of the volume to be exploited (fractures, cavities, etc.) must be known, and the GPR technique could also be used for this purpose. However, as observed in this work, the response is better for sub-horizontal than for sub-vertical discontinuities. Analyses were also performed in commercial blocks prior to the cutting process. Using 800 MHz antennae, it was possible to detect changes in the texture because a different behaviour was observed for rocks with a banded texture (lepidoblastic or banded by fenestral porosity) compared

to rocks with a granoblastic or microcrystalline texture. The GPR technique also allowed for the detection of structural anomalies, demonstrating the usefulness of the technique for evaluating the block quality, determining whether resins must be injected to consolidate the block and estimating the orientation of the cutting process.

Regarding the proposed processing method based on a PLCA approach with energy compensation, it can be concluded that the method is adequate for the detection of anisotropies in this type of material because it allows for the detection of zones with a high probability of anisotropy. Once these zones are located, highly detailed information can be obtained for the zones of interest. The PLCA-based algorithm achieves a deconvolution of the pulse emitted by the radar that improves the clarity of the images. However, compensating for the energy loss as a result of reflections allows for the detection of objects at higher depths because it avoids shadow zones produced by shallow reflections, meaning that it compensates for the fast attenuation resulting from the effects of wave reflection by the different materials throughout the depth axis.

The usefulness of the GPR technique for the detection and evaluation of the structure, composition and anomalies of the material has been demonstrated, and the technique can be utilised to characterise the quality of stone. Therefore, GPR can be used as a tool for the selection of ornamental stones for monuments and works with stringent quality criteria.

Acknowledgements

This study was carried out using funds provided by Government of Andalusia (Proyect TIC-7278).

References

[1] Arosio D., Munda S., Zanzi L., Porto F., Mosele F., "Nondestructive Quality Control of Reinforced Masonry Buildings", *Journal of Infrastructure Systems. Special Issue: Nondestructive Testing in Civil Engineering*, vol. 18, no. 1, pp. 34-46, 2012.

[2] Bridge J.S., Alexander J., Collier R.E.L.L., Gawthorpe R.L., Jarvis J. "Ground-penetrating radar and coring used to document the large-scale structure of point-bar deposits in 3-D", *Sedimentology*, vol. 42, p.. 839-852.

[3] Cerrillo C., Jiménez A., Rufo M., Paniagua J., Pachón F.T., "New contributions to granite characterization by ultrasonic testing", *Ultrasonics*, vol. 54, pp. 156–167, 2014.

[4] Davis J.L., Annan A.P., "Ground-penetrating radar for high-resolution mapping of soil and rock stratigraphy", *Geophysical Prospecting*, vol. 37, pp. 531-551, 1989.

[5] Grandjean G., Gourry J.C., "GPR data processing for 3D fracture mapping in a marble quarry (Thassos, Greece)". *Journal of Applied Geophysics*, vol. 36, pp. 19–30, 1996.

[6] Forte E., Pipan M., Casabianca D., Di Cuia R., Riva A., "Imaging and characterization of a carbonate hydrocarbon reservoir analogue using GPR attributes", Journal of Applied Geophysics, vol. 81, pp. 76-87, 2012.

[7] Hoyer P., "Non-negative Matrix Factorization with Sparseness Constraints", *Journal of Machine Learning Research*, vol. 5, pp. 1457–1469, 2004.

[8] IGME. "Mapa geolgico de Espaa. Escala 1/50.000. Hoja n 1013 (Macael)". *Servicio de Publicaciones Instituto Geolgico y Minero de Espaa*, Madrid, 58 pp., 1975.

[9] Kadioglu S., "Photographing layer thicknesses and discontinuities in a marble quarry with 3D GPR visualisation", *Journal of Applied Geophysics*, vol. 64, pp. 109–114, 2008.

[10] Khan U., Al-Nuaimy W., "Background removal from GPR data using Eigenvalues", *13th International Conference on Ground Penetrating Radar (GPR)*, Lecce, Italy, 2010.

[11] King B., Smaragdis P., Mysore G.J., "Noise-robust dynamic time warping using PLCA features", *Proceedings of the IEEE International Conference on Acoustics, Speech and Signal Processing*, Kyoto, Japan, 2012.

[12] Lualdi M., Zanzi L., "2D and 3D experiments to explore the potential benefit of GPR investigations in planning the mining activity of a limestone quarry", *Tenth International Conference on Ground Penetrating Radar*, Delft, The Netherlands, 21 -24 June, 2004.

[13] Lopez-Vizcaino V., "Evolucin petrolgica y geoqumica de las rocas carbonticas en el rea de Macael-Cbdar, Complejo Nevado-Filbride, SE Espaa", *Tesis Doctoral*, Univ. Granada, 241p., 1994.

[14] Monga V., Mhcak M., "Robust and Secure Image Hashing via Non-Negative Matrix Factorizations", *IEEE Transactions on Information Forensics and Security*, vol. 2, pp. 376-390, 2007.

[15] Nam J., Mysore G.J., Smaragdis P., "Sound recognition in mixtures", *Proceedings of the international conference on Latent Variable Analysis/Independent Component Analysis*, Tel-Aviv, Israel, 2012.

[16] Neal A. "Ground-penetrating radar and its use in sedimentology: principles, problems and progress", *Earth Sci Rev*, vol. 66, pp. 261-330, 2004.

[17] Onur A.H., Bakrac S., "Determination of discontinuities in marble blocks via a nondestructive ultrasonic technique", *Int J Miner Metall Mater*, vol. 16, pp. 487-493, 2009.

[18] Porsani J. L., Sauck W. A., Junior A. O. S., "GPR for mapping fractures and as a guide for the extraction of ornamental granite from a quarry: A case study from southern Brazil", *Journal of Applied Geophysics*, vol. 58, pp. 177-187, 2006.

[19] Saez-Perez M.P., Rodriguez-Gordillo J., "Structural and compositional anisotropy in Macael marble (Spain) by ultrasonic, x-rd XRD and optical microscopy methods", *Constr Build Mater*, vol. 23, pp .2121–2126, 2009.

[20] Sarpun I.H., Kilickaya M.S., "Mean grain size determination in marbles by ultrasonic first backwall echo height measurements", *NDTE Int*, vol. 39, pp. 82–86, 2006.

[21] Sengwa R. J., Soni A., "Low-frequency dielectric dispersion and microwave dielectric properties of dry and water-saturated limestones of the Jodhpur region", *Geophysics*, vol. 71, no. 5, pp. 269-277, 2006.

[22] Sigurdsson T., "Ground penetrating radar for geological mapping", PhD Thesis, Arhus University, Arhus Geoscience, 1995.

[23] Sigurdsson T., Overgaard T., "Application of GPR for 3-D visualization of geological and structural variation in a limestone formation", *Journal of Applied Geophysics*, vol. 40, pp. 29–36, 1998.

[24] Smaragdis P., Brown J., "Non-negative matrix factorization for polyphonic music transcription", *IEEE Workshop on Applications of Signal Processing to Audio and Acoustics (WASPAA)*, New Paltz, USA, 2003.

[25] Smaragdis, P., Raj, B., Shashanka, M.V., "Supervised and Semi-Supervised Separation of Sounds from Single-Channel Mixtures", *Proceedings of the 7th International Conference on Independent Component Analysis and Signal Separation*, London, UK, September 2007.

[26] Smaragdis P., Raj B., "Shift-Invariant Probabilistic Latent Component Analysis", Tech report, 2007.

[27] Solimene R., Cuccaro A., Dell'Aversano A., Catapano I. and Soldovieri F., "Background removal methods in GPR prospecting", *European Radar Conference (EuRAD)*, 2013.

[28] Paulus J., Virtanen T., "Drum Transcription with Non-negative Spectrogram Factorisation", *Proc. EUSIPCO*, 2005.

[29] Torres-Ruiz J., Pesquera A., Snchez-Vizcano V., "Chromian tourmaline and associated Cr-bearing minerals from the Nevado-Filbride Complex (Betic Cordilleras, SE Spain)", *Mineralogical Magazine*, vol. 67, pp. 517-533, 2003.

Paper B

Detection and classification of internal defects in limestone blocks based on a deconvolution technique with SI-PLCA applied to GPR signals

Montiel V., Cañadas F., Vera P., Ruiz N., Rey J., Martínez J., "Detection and classification of internal defects in limestone blocks based on a deconvolution technique with SI-PLCA applied to GPR signals", *Research in Nondestructive Evaluation*, under review.

Abstract

In this work, a novel migration method is applied to Ground-Penetrating Radar (GPR) data to detect the internal flaws of ornamental stone blocks. To detect and classify fractures in accordance with their spatial orientation, a Shift-Invariant Probabilistic Latent Component Analysis (SI-PLCA) is proposed.

GPR simulations are conducted using modelling software to test several types of fractures (with different positions, thicknesses and lengths) in rock blocks and to train several patterns as inputs for the SI-PLCA method. An 800 MHz antenna is used to assess both simulated and real data. The accuracy rate of the proposed approach is evaluated and compared with that of classical migration methods for detection and is compared to a Template Matching approach for classification; promising results are obtained.

In addition, GPR is applied to two blocks of a rock type known commercially as Crema Marfil. The 3D fracture maps obtained from the proposed approach are compared with the stone slabs from the cutting process.

The results show that the proposed approach applied to GPR radargrams is an effective method for determining the internal structure of stone materials, particularly for detecting and classifying fractures.

Key words: *GPR, Processing, Hilbert Transform, Migration, Deconvolution, PLCA, SI-PLCA, Thresholding*

1 Introduction

Structural discontinuities, such as cavities, fractures, and foliations, could cause breakage in ornamental rocks, and detecting these discontinuities remains a challenging task in the mining industry [1] [10] [19] [24] [27]. Non-destructive techniques (NDTs) can determine the location and sizes of possible defects or imperfections in extracted blocks, thus improving the exploitation of the blocks, increasing profitability and reducing the environmental impact of the quarrying industry. Knowing the internal structure (fissures, fractures, cavities, bedding, etc.) of blocks before initiating the block rolling process can be helpful. NDTs can be used to evaluate whether the block

must be consolidated using resins (or other components), to establish injection points (if necessary), and to optimise the cutting or lamination process of the block. The automatic detection of different defects in marble units can be used to evaluate the quality of the extracted blocks and to avoid transporting low-quality blocks to the cutting process. Therefore, this application can assess the profitability and optimise the traditional exploitation criteria. In addition, this method could produce remarkable benefits by reducing both cutting costs and environmental impact and increasing productivity.

Previous studies have addressed the non-destructive characterisation of ornamental stones. Sarpün and Kilickaya [30] utilised Ultrasonic Relative Attenuation (URA) to estimate grain sizes in marble. In addition, ultrasonic transmission techniques have been used to study mineralogical composition and to characterise structural discontinuities in ornamental rocks [29] [19]. Recently, Cerrillo et al. [5] applied statistical linear correlations between the parameters of ultrasonic techniques and the physical and mechanical properties of granite and obtained competitive results. However, despite their resolution, all ultrasonic techniques require sophisticated procedures because a transducer must be placed at each measured position or an array of sensors must be located along the material, thus making real measurements relatively time consuming [20].

Ground-Penetrating Radar (GPR) has been widely used to analyse quarries, usually by using portable equipment that can be used to quickly evaluate a block directly at the quarry. Sigurdsson [34] performed lithographic characterisation studies in limestone quarries. Sigurdsson and Overgaard [35] studied limestone using GPR (using a 100 MHz antenna), which allowed them to differentiate zones with textural variations (bryozoan limestone, coral limestone and wackestone). Grandjean and Gourry [10] and Kadioglu [14] used this technique to detect fractures in marble quarries in Greece and Turkey, respectively. Porsanic et al. [24] used GPR in granite quarries in Brazil. Recently, Rey et al. [27] used GPR techniques at a marble quarry in Macael (Almería, Spain). This study shows that GPR is able to differentiate marble units from mica schists, making GPR a suitable tool for evaluating the reserves in a quarry.

A GPR radargram shows the effects of clutter, which can be defined as those signals that are unrelated to the real target but that are present in the same time window and have similar spectral characteristics. Clutter may be

caused by reflections between the antenna and the surface, by interference between the emitting and receiving antenna (cross-talk) and possibly by scattered signals of other objects [6]. There are several methods that suppress this effect, such as background removal methods [15] [37]. Moreover, because of the beamwidth of the GPR antenna [40], diffractors appear as hyperbolas in radargrams. In addition, there are migration methods [9] that shift the anomaly image from its apparent position to its true position [22]. Nevertheless, traditional migration methods suffer from some limitations, as described below, and they cannot classify the type of fracture.

In addition, pattern recognition methods have been developed that can be used to classify GPR radargrams. For example, Sezgin [31] describes a 2D Template Matching method for discriminate buried objects that uses a morphological process and calculates a normalized cross-correlation between several input patterns and the input image. Moreover, Pasolli [23] developed a novel pattern-recognition system to classify buried objects using genetic algorithms and support vector machine.

To minimize the errors derived from an incorrect user interpretation, Probabilistic Latent Component Analysis (PLCA) has been demonstrated to be a promising tool for denoising or separating target sources from non-target sources [18] [16]. Thus, the main novelty of this paper is the detection and classification of internal defects as a function of the orientation (horizontal, vertical or diagonal) in damaged limestone blocks. To achieve this goal, we define a processing framework that includes a block implementing the Shift-Invariant PLCA (SI-PLCA) algorithm with a kernel distribution for each orientation: vertical, horizontal and diagonal (with tilt angles of 45° and -45°) fractures. This classification of fractures is highly relevant during the cutting process because vertical and diagonal fractures are critical for the breaking of rock slabs and the cutting speed can be adjusted accordingly.

The proposed method is tested on both synthetic datasets (one dataset for training the algorithm and another for evaluating it) and real data. Different radargrams, obtained from GPR applied to stone blocks of different qualities, are compared with theoretical models to identify different types of discontinuities. Finally, we evaluate the ability of the proposed method to detect fractures compared to traditional migration methods, and we compare its classification ability to that of a Template Matching approach. This paper is organized as follows. Section 2 presents a review of the material that

is analysed. Section 3 describes the potential of GPR for detecting internal defects in blocks, the processing algorithms used to improve its resolution and the SI-PLCA algorithm. The proposed method for detecting and classifying defects is presented in Section 4. Section 5 shows the numerical and visual results (related to synthetic and real data, respectively) used to evaluate the performance of the proposed method. Finally, the conclusions and future work are provided in Section 6.

2 Rock specimens

This study focuses on a cream-coloured massive limestone known by its Spanish name *Crema Marfil (White Ivory)*. Although this lithology was originally exploited in the Sierra de El Coto, next to the town of Pinoso (Alicante, Spain), there are currently more than twenty quarries that extract this rock. These quarries are distributed in different geologic domains in the external areas of the Baetic System between the provinces of Murcia and Alicante (Spain) and process a rock volume of greater than 500.000 m^3 per year.

The limestone consists of biomicrites (packstone) that is dominated by benthic foraminifera (orbitoids and nummulits) and also includes remains of echinoderms, gastropods and algae. The association of foraminifera has allowed these facies to be attributed to the Eocene [8] [11].

Their good mechanical performance (high impact resistance and low water absorption coefficient) along with aesthetic considerations justify the high demand for these rocks in the construction industry. Nevertheless, there are secondary processes that negatively alter their original quality and thus their exploitation potential. In this regard, the presence of stylolitic surfaces, joints or even karstification processes should be noted [3]. All of these factors could contribute to generating discontinuities, which could result in breaking the rock.

3 Background

The GPR technique is used as a non-destructive prospection method and is based on studies of the propagation of high-frequency electromagnetic (EM) waves from an emitting antenna that uses short pulses while moving across

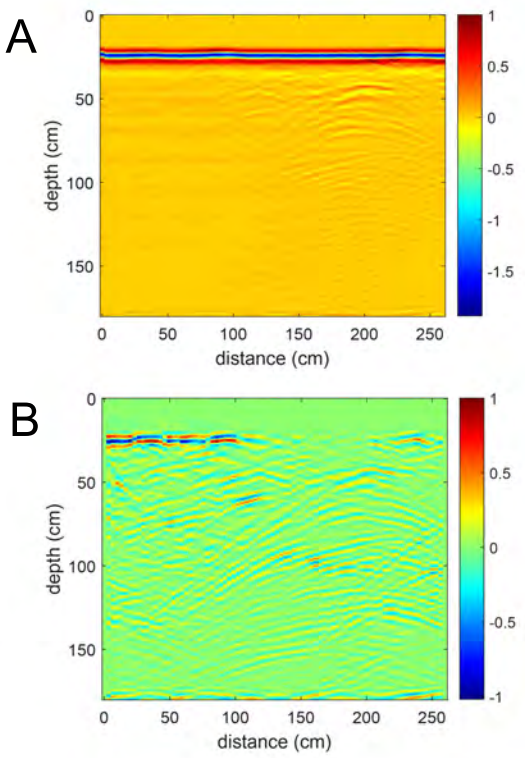

Figure 1: (A) Raw radargram resulting from a real measurement of a block using the MALAGS Pro-Ex model RAMAC GPR system with an 800 MHz antenna. The Y-axis is displayed according to a velocity value of 10 cm/ns in time/depth conversion. (B) Radargram after pre-processing (DC removal, background removal, AGC and band-pass filtering) performed with the RadExplorer software.

a surface. When there is a boundary between two regions with different EM parameters (conductivity, permittivity and permeability), the emitted wave is reflected toward the surface, where the receiving antenna measures its energy.

The potential of this technique for detecting fractures and internal defects in quarries [27] [17] and natural stone blocks [1] has been assessed, representing the most promising method for this application because of its resolution and short measuring time.

The nominal frequency should be selected based on the necessary tradeoff between the penetration depth (low frequency) and resolution (high frequency) [28] as well as on the EM properties of the material to be tested.

Typically, analysing a raw radargram (B-scan) is not trivial due to the effects of clutter, as mentioned previously. Various pre-processing techniques [6] [28] [12] are applied to each trace in the depth (A-scan) of the radargram to both reduce clutter and enhance the signal-to-noise ratio (SNR).

Fig. 1 presents two radargrams: Fig. 1.A shows a raw radargram extracted from measurements of a *Crema Marfil* block using a GPR system that is equipped with an antenna with a nominal frequency of 800 MHz. After pre-processing, we obtain the image shown in Fig. 1.B. The internal structure of the block is thus clearly identified, and the interface (separation between rock and air/soil) is highlighted (at approximately 180 cm). Some diagonal reflections, due to the contrast between the rock and the air when the antenna reaches the lateral end of the block, are present on the right side of the radargram, making the internal analysis of the block difficult. Finally, some problems can be observed at a depth of 40-100 cm and at a distance of 120-225 cm, where the fractures have an unknown spatial orientation.

As previously shown in Fig. 1, the image of a target generated using GPR does not correspond to its geometrical representation due to the beamwidth of the antenna, the wavelength of the radiation and the physical dimensions of the buried object [6]. Because most GPR systems use broad beamwidth antennae, an object that is not directly under the antenna reflects energy. As a result, a single point scatterer appears as a hyperbola, where the appendix indicates the spatial position of the target. A brief review of migration methods that have been previously proposed to solve this issue is provided in the following.

3.1 Migration methods

Migration is an algorithm for processing data to correctly focus targets in the subsurface. This technique, which is based on spatial deconvolution, attempts to locate the reflections from the dipping reflectors back to their true spatial position and physical shape, thus improving the spatial resolution [22], increasing the target detectability and reducing the effect of the antenna beamwidth. This algorithm requires the propagation velocity to be known in advance (a different velocity model from the medium velocity could produce a misleading migrated section) [42].

The most relevant migration methods are Kirchhoff [32] and F-K [38].

3.1.1 Kirchhoff

This technique is based on the diffraction summation method, which consists of searching the input data in (x, t) space for energy that could come from a diffracting source located in the output (x, z). Then, the method sums the amplitudes in (x, t) space along the diffraction curve (Huygen's secondary source) at each point in (x, z). The selection of the aperture width and the maximum dip to migrate is critical for preserving the dipping events and decreasing the computational costs. Moreover, velocity errors can lead to undermigration or overmigration.

3.1.2 F-K

The F-K migration (or Stolt migration) technique was first developed by Stolt [38]. It is the fastest known migration technique [2] because it is based on the Fourier transform. This method works in the frequency-wavenumber $(\omega - k)$ range, and a variable transform is performed within this range based on the constant velocity assumption; however, this method was later modified to handle velocity variations. Velocity errors can also cause undermigration or overmigration when using this technique in addition to problems related to the maximum dip to migrate.

3.2 SI-PLCA

The decomposition of probability density or count data into a set of shift-invariant components has been widely evaluated by extracting features from real-world audio and images to improve the quality of the inputs. Moreover, non-negativity has proven to be a valuable property, and its use is appropriate for this type of decomposition [36]. Thus, a non-negative radargram could be thought of as a distribution that can also be decomposed and can be modelled using non-negative values. Thus, our radargrams should be pre-processed using a Hilbert Transform (HT) for envelope detection and then decomposed using this algorithm. The main reason for using HT instead of applying its absolute value lies in the necessity of discarding the phase information and of considering only the envelope.

SI-PLCA is defined using a two-dimensional convolution as

$$P(y, z) = \sum_{\varphi} P(\varphi) \int \int P(\tau_y, \tau_z|\varphi) P(y - \tau_y, z - \tau_z|\varphi) d\tau_y d\tau_z \tag{1}$$

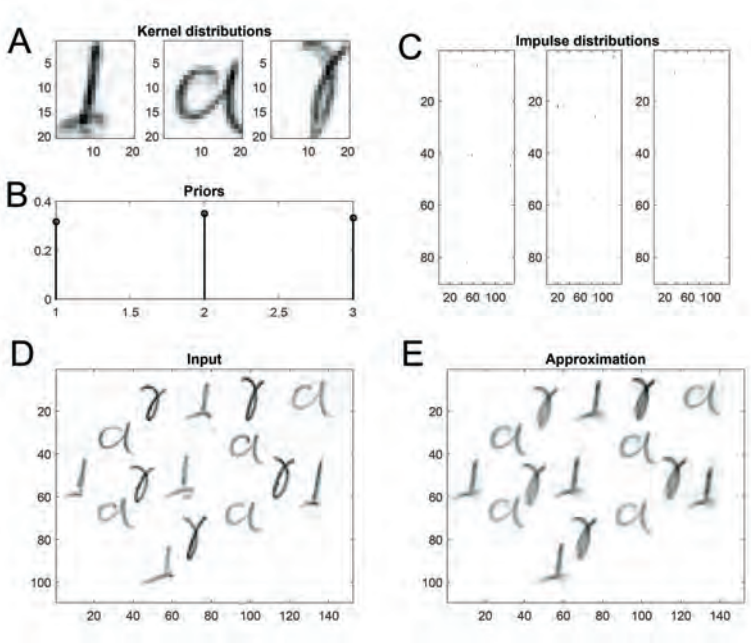

Figure 2: (A) Extracted kernel distributions $P(\tau_y, \tau_z|\varphi)$, (B) Priors $P(\varphi)$, (C) Impulse distributions $P(y-\tau_y, z-\tau_z|\varphi$, (D) Handwriting example $P(y, z)$ using three different characters, and (E) The resulting approximation.

where the y dimension is the distance, the z dimension is the depth, $P(y, z)$ is the radargram (input), φ is the latent variable, $P(\varphi)$ is an N-dimensional distribution of the random variable φ, and $P(\tau_y, \tau_z|\varphi)$ is the kernel distribution, which can be shifted in the left-right and up-down dimensions. The algorithm can obtain the kernel distribution from scratch or can be initialized if the kernels are known in advance (as in our case). Therefore, the kernel distributions correspond to the searched patterns (one per orientation). Finally, $P(y-\tau_y, z-\tau_z|\varphi)$ is the impulse distribution (output), which provides the spatial positions of the kernels.

An example of an input image $P(y, z)$ composed of 109x152 greyscale pixels is shown in Fig. 2.D. Three different characters at arbitrary positions constitute the image. The three 20x20 kernel distributions ($P(\tau_y, \tau_z|\varphi)$), which are estimated by the algorithm, are shown in Fig. 2.A. Once the decomposition has been computed, the priors $P(\varphi_i)$ (Fig. 2.B) indicate the probability of each letter, namely, the weight of each kernel in the input figure. On the other hand, the impulse distribution $P(y-\tau_y, z-\tau_z|\varphi)$ (Fig.

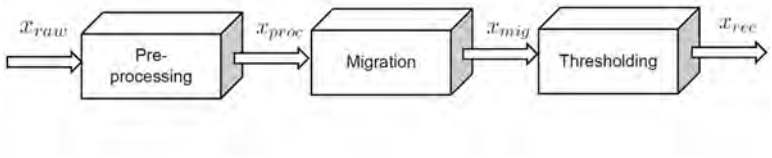

Figure 3: Flowchart of the general processing of the radargram. The raw radargram (x_{raw}) is pre-processed and then migrated (x_{mig}). Finally, the relevant part of the B-scan is selected after thresholding (x_{rec}). In this way, the reconstructed radargram is generated and represents the existing fractures.

2.C) contains the activations (position and energy) that correspond to each letter. The equation is iteratively applied until the estimates for $P(\varphi)$, $P(y-\tau_y, z-\tau_z|\varphi$ and $P(y,z)$ converge to a solution. For most cases presented in [36], convergence can be achieved in approximately a hundred iterations with similar results. The reconstructed image ($P(y,z)$) (Fig. 2.E), which is composed of these three patterns, is approximately equal to the input image. This example clearly shows the potential of SI-PLCA for classifying different patterns. In addition to positioning the kernel, the algorithm is able to show the activation of each pattern with the prior information. The computational complexity and implementation are detailed in [36].

4 Methods

The objective of the proposed method, which is based on the SI-PLCA approach [36], is to identify and extract possible fractures that present horizontal, vertical or diagonal spatial orientations in a radargram. For this purpose, the proposed method consists of three stages: pre-processing, migration and thresholding, as shown in Fig. 3. First, each profile is pre-processed. Then, radargrams are migrated (using both the proposed method and the classic migration techniques). Finally, the noise and energy from non-targets is discarded using a thresholding procedure based on the Otsu method [21].

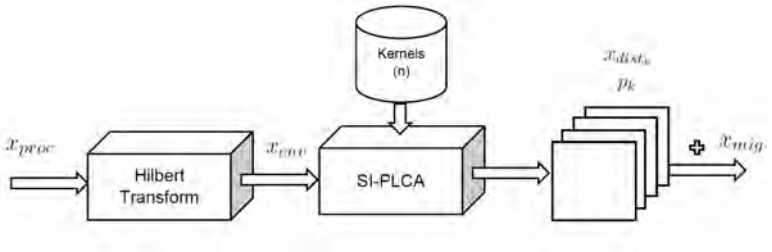

Figure 4: Block diagram detailing the proposed migration method. First, the pre-processed radargram (x_{proc}) of a section of the block is processed using HT for envelope detection (x_{env}) and is then processed using the SI-PLCA algorithm with a database of n synthetic patterns known in advance. These patterns exhibit different shapes depending on the fracture that must be found. Thus, the output of the proposed migration method is a set of activations for each pattern (x_{dist_k}) and their priors (p_k).

4.0.1 Pre-processing

This first stage processes each input GPR profile x_{raw} into an output GPR profile x_{proc}. The steps in standard pre-processing are as follows: (a) DC removal so that the mean (or median) value of the A-scan is zero; (b) background removal, which removes a constant instrument component from the recording (a subtraction of the mean trace determined in a window); (c) automatic gain control (AGC), which equalizes the amplitude of the signal to account for the fact that the emitted wave could suffer high attenuation along the material; and (d) band-pass filtering, which deletes unwanted frequencies and increases the SNR. This pre-processing (normally available in standard GPR software) was conducted using the software RadExplorer [25], which is a tool widely used in the field of GPR analysis.

A real radargram is shown in Fig. 1.A, and the pre-processed radargram is shown in Fig. 1.B. The internal structure of the block is more clearly presented in the pre-processed radargram because the interference that masks the structure, i.e., the wave reflections due to changes in the EM properties (block-soil or block-air, which is more common), has been attenuated or removed. However, energy from the anisotropies of the material or noise remains in the radargram.

4.0.2 Migration

This second stage attempts to improve the results obtained from the classical migration methods, which not only detect the defects but also classify the type of defect, representing our main contribution. The block diagram of the proposed migration technique based on SI-PLCA is shown in Fig. 4. First, the radargrams are processed by the HT, obtaining a non-negative image. Then, the SI-PLCA algorithm is applied with a set of simulated kernels (known in advance as patterns). The output consists of a set of activations per pattern, indicating the energy and the position of the fracture. Then, because we have an impulse distribution per pattern, these activations are summed to obtain the total impulse distribution; this is the migrated radargram.

4.1 Envelope Detection using HT

The Hilbert Transform is a widely used tool for expresing a band-pass signal as a low-pass signal (with the complex envelope) and a phasor [4]. Each trace (A-Scan) of the pre-processed radargram, $x_{proc}(t)$, is a signal with a certain envelope, frequency and phase and can be converted to an analytic signal $x_a(t) = x_{proc}(t) + j\hat{x}_{proc}(t) = x_c(t)e^{j\phi(t)}$, where $\hat{x}_{proc}(t)$ is the HT of the input signal $x_{proc}(t)$. Thus, $x_c(t)$ and ϕ are the complex envelope and the phase of the signal $x_{proc}(t)$, respectively. Then, $x_{env}(t) = |x_c(t)|$ is the envelope. Thus, the whole B-Scan x_{env} can be processed using the SI-PLCA algorithm since the inputs are non-negative values.

4.2 Proposed SI-PLCA methods

In this subsection, the proposed classification method and hyperbola method are detailed.

First, a synthetic dataset is created using the ReflexW commercial package [26], which applies the Finite-Difference Time-Domain (FDTD) method, using a configuration as similar to the real measured data as possible. Considering that a 3D simulation has a very high computational cost, a 2D simulation is applied to the database as a suitable approximation for a real GPR measurement; no significant differences are shown between the 2D and 3D results.

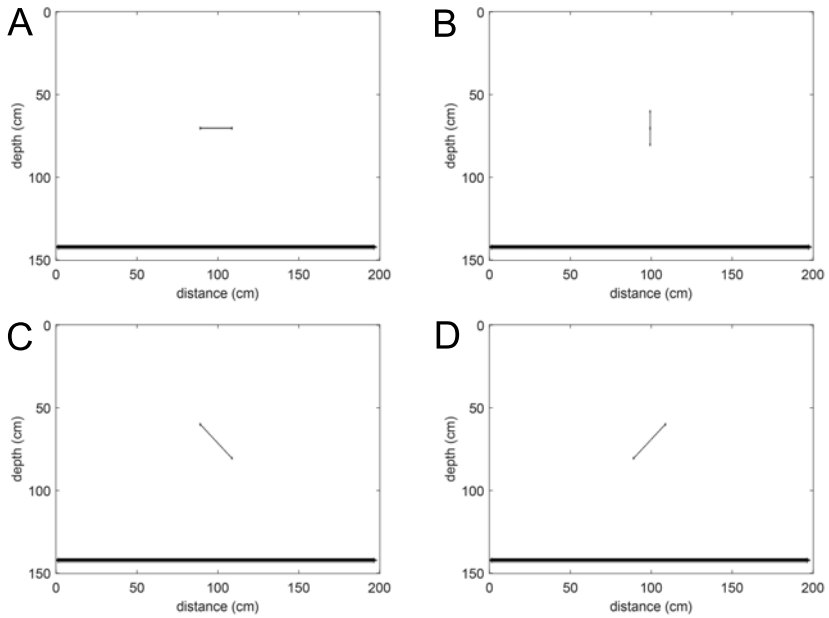

Figure 5: The four models, implemented using the software ReflexW, that constitute the database. Each model represents a block of stone (relative permittivity ϵ_r = 8) with dimensions of 1.50x2 m and a flaw (ϵ_r = 1) with a dimensions (width x length) of 0.002x0.2 m

The dataset is composed of four simulated models that represent different spatial orientations of fractures, specifically, horizontal, vertical and diagonal fractures with tilt angles of 45° and -45° (with a length of 0.2 m and a width of 0.002x0.2 m). The term length refers to the larger linear dimension of the fracture regardless of its spatial orientation, and the term width refers to the smaller linear dimension.

The simulation was performed using the following operating parameters: antenna nominal frequency of 800 MHz, sampling interval of 0.005 m (a value of less than $\lambda/4$ to avoid spatial aliasing) and sampling frequency of 62.5 GHz (this frequency is established by default in the ReflexW software). The selected time window varies depending on the block thickness, which in our case is 150 cm. For this estimation, the propagation velocity is calculated first, knowing the relative permittivity of the material ϵ_r. This value is estimated according to [33] [6] [39], and its value varies between 7 and 8. Moreover, the dielectric constant was estimated using the software RadExplorer (using its fitting hyperbola tool) for radargrams from real limestone

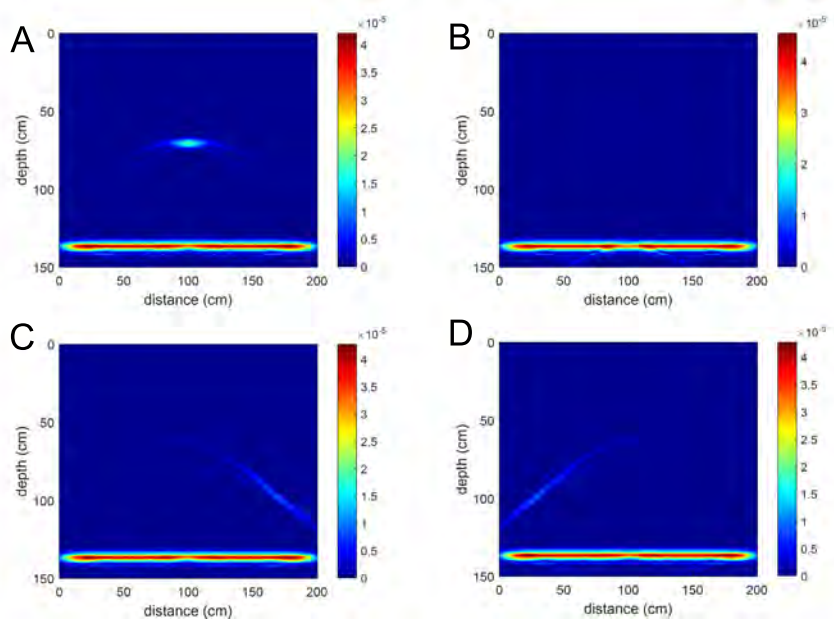

Figure 6: The radargrams, obtained using the software ReflexW, related to the four models of the database shown in Fig. 5. Each radargram comprises only non-negative values.

blocks, and a mean value of approximately 8 was obtained (a constant value between 7 and 9 was obtained depending on the block). For this reason, we vary this constant between these values. Then, limestone has a simulated random pattern (with a normal distribution), where the dielectric constant has a variance of 1 and a mean value of 8. In this way, the anisotropy in the block structure is simulated as realistically as possible. The fracture is assumed to be filled with air. Finally, the estimated velocity of the medium is approximately 106 mm/ns using the selected permittivity value. As a result, the estimated time window is approximately 35 ns using the estimated velocity of the medium and knowing the depth of the designed profile.

The four models of the above-mentioned database are shown in Fig. 5. The radargrams obtained after applying envelope detection are presented in Fig. 6, which shows the orientations of the fractures in the different radargrams. Moreover, the positions of the diagonal defects suffer a strong lateral shift due to the geometry of the zero-offset acquisitions. This effect was evaluated using initial simulations that indicate that this lateral shift increases with increasing inclination of the diagonal defect.

Then, the first proposed algorithm, called the classification method, uses

these four patterns (kernels for the SI-PLCA method). Once the algorithm converges (a total of 100 iterations is used because the convergence was observed experimentally), we extract the impulse distribution of each orientation pattern (x_{dist_k}), as well as the priors (p_k, the activation per pattern). This allows us to classify the defects, unlike the existing migration methods, because their orientations can be established in terms of the impulse distribution, which is weighted with the corresponding prior, and the maximum energy. In this way, kernels that are the most likely to occur are prioritized.

The energy returned from each pattern is different because a horizontal fracture returns a higher amplitude than a vertical fracture due to its geometry. To overcome this damaging effect, the impulse distribution of each fracture must be compensated using SI-PLCA as follows. First, each pattern (horizontal, vertical or diagonal) is considered as both an input image and an input kernel, and an identical process is applied for all the patterns. The maximum amplitude of each impulse distribution is equalized, obtaining the compensation factor of each pattern c_k. Finally, when a radargram is processed using SI-PLCA methods and taking its patterns as kernels, the sum of the impulse distributions is weighted by the prior of each kernel; then, with this sum, the compensation factor, and the image give the proposed migrated radargram x_{mig}.

$$x_{mig} = \sum_{k=1}^{n} x_{dist_k} \cdot p_k \cdot c_k \tag{2}$$

where n is the total number of kernels.

To compare the proposed method with an SI-PLCA approach that models a traditional migration method, an SI-PLCA not informed by kernels based on different fracture orientations is considered. In this manner, the proposed method is compared to an SI-PLCA called the hyperbola method that is composed of only one kernel and is based on a hyperbola pattern.

Finally, to illustrate the scheme, Fig. 7.A shows a simulation of a horizontal fracture, and Fig. 7.B displays the radargram after envelope detection. The radargrams reconstructed using SI-PLCA with four kernels and one kernel are shown in Fig. 7.C and 7.D, respectively.

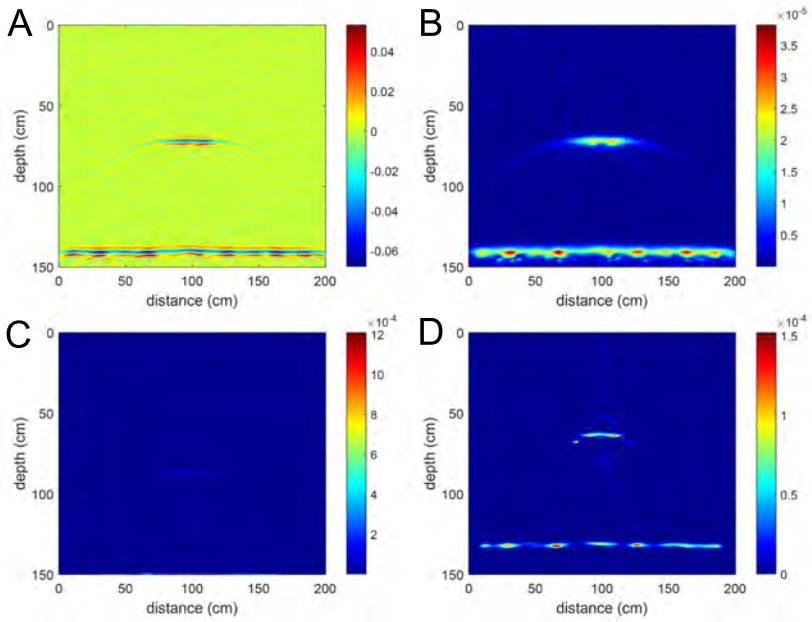

Figure 7: (A) Raw radargram of a horizontal fracture, (B) Radargram after envelope detection using HT, (C) Reconstructed radargram using the hyperbola method, and (D) Reconstructed radargram using the classification method.

4.3 Thresholding

Once the envelope detection and deconvolutions have been computed, it is important to select an adequate threshold by extracting the targets from the background.

In an ideal case, the histogram of an image presents a deep valley between two peaks (representing the target and background) so that the threshold is the centre of this valley. However, in real images, precisely selecting the valley bottom is not trivial. A technique that can be used to solve this problem is the Otsu method [21], which is a nonparametric and unsupervised method for automatic threshold selection.

For the proposed methods, the energy from the end of the block (interface) is always active in the radargram due to the change between block-air (or soil) mediums; the same occurs due to anisotropies inside the block. Therefore, it is useful to analyse how the energy is distributed in the deconvoluted radargram to define a dynamic thresholding for each radargram.

Then, the Otsu method can determine whether the energy inside the block has sufficient significance when compared with the energy of the anisotropies to be labelled as a fracture. As the interface is used as a reference, multi-level thresholding is used, which uses two thresholds to classify the pixels into three classes: the air/block interface, the fracture and the background. Then, the minimum threshold is used as the final threshold.

In this way, the Otsu method is applied to obtain a binary reconstructed radargram in which each pixel indicates whether it is part of a fracture (see e.q., 3).

$$x_{rec}(t,d) = \begin{cases} 1, & if x_{mig}(t,d) \geq thresh \\ 0, & otherwise \end{cases} \tag{3}$$

where the parameters t and d indicate depth in time and distance, respectively, x_{mig} represents each pixel of the image output of the migration stage, the parameter $thresh$ is related to the estimated threshold using the Otsu method, and x_{rec} corresponds to the reconstructed radargram after the thresholding process.

5 Evaluation

5.1 Data

The interpretation of the data from a GPR system is a complicated procedure due to the complexity of the signals. Although signal processing is applied to the real measurements from a GPR system, it is important to conduct simulations as realistically as possible to achieve an objective evaluation of the GPR performance for evaluating different defects.

First, the proposed methods were evaluated using databases composed of synthetic and real radargrams. We highlight that different simulations were performed for training and testing tasks to validate the results. Finally, the proposed methods were evaluated by analysing the internal structure of real limestone blocks.

5.1.1 Simulated data

The software ReflexW [26] was used to create synthetic data using the same operating parameters mentioned in Section 4.2.

5.1.2 Real data acquisition

The analysis of a real block is a complex process because the size is variable and the surface is usually rough. The established working method consists of measuring different profiles along the top face (the direction of measurement is denoted as 'Y', and 'Z' is the depth), each separated by 10 cm in the 'X' direction. To achieve correct antenna positioning, a measuring tape was used as a reference along each profile. It is important to preserve this positional accuracy and the correct antenna orientation.

Profiles were obtained using the Pro-Ex model RAMAC/GPR system manufactured by MALA GeoScience and a shielded 800 MHz antenna. The operating parameters were a sampling interval of 0.026 m and a sampling frequency of 8 GHz.

5.2 Metrics

To assess the robustness of the proposed method, the accuracy and error rates were evaluated using a database of simulated data, and we compared the reconstructed radargram x_{rec} and its corresponding model. This objective evaluation is only possible using simulated data because this type of data can maintain the ground truth of each model image for comparative purposes. The following three values were computed as results: accuracy (ACC), hit rate (HR) and false alarm (FA) rate [13]. ACC represents the percentage of correctly classified pixels; HR represents the percentage of pixels with correctly detected defects (this metric is therefore our priority), and FA represents the percentage of pixels with no defects that are erroneously classified as defects.

$$ACC = \frac{N_D^{corr} + N_N^{corr}}{N_D + N_N} \times 100 \tag{4}$$

$$HR = \frac{N_D^{corr}}{N_D} \times 100 \tag{5}$$

$$FA = \frac{N_N^{notcorr}}{N_N} \times 100 \tag{6}$$

where N_D^{corr} and N_N^{corr} are the total number of pixels with defects and the total number of pixels with no defects that are correctly classified from the reconstructed radargram, respectively; $N_D^{notcorr}$ and $N_N^{notcorr}$ are the total

number of pixels with defects and the total number of pixels with no defects erroneously classified from the reconstructed radargram, respectively; and $N_D = N_D^{corr} + N_D^{notcorr}$ and $N_N = N_N^{corr} + N_N^{notcorr}$ are the total number of pixels with defects and the total number of pixels with no defects from the model, respectively.

For comparison purposes, the references N_D and N_N were obtained from the four model images (in Fig. 5), which were assumed to be the ground truth, whereas N_D^{corr}, N_N^{corr} and $N_N^{notcorr}$ were extracted from the reconstruction of each method. Because the metrics are defined for Boolean images, when some energy appears in our model, it is assumed to be a defect. To correctly compare the model and reference, it is necessary to remove the part of the final reflection (at the end of the block) prior to evaluating the metrics.

In our case, ACC is not a representative metric because the part of the image with rock is higher than the fracture part. Therefore, even though the fracture was not reconstructed, the ACC rate would be very high. A higher HR and lower FA indicate better results. HR, which is the number of pixels correctly detected as a fracture, should be maximized. A zero value of HR means that there are no pixels above Otsu's threshold, and a 50 % HR represents that the method is able to correctly detect half of the fracture pixels. In contrast, FA, which is the number of pixels incorrectly detected as a fracture, should be minimized.

5.3 Algorithms for comparison

Two reference state-of-the-art migration methods (Kirchhoff [32] and F-K [38], which are denoted as 'K' and 'FK', respectively) were used to evaluate the proposed method. For this purpose, images migrated by each classic migration method were obtained using the ReflexW software. The selected velocity for performing the migration methods was 106 mm/ns according to the permittivity, as mentioned above.

5.4 Results evaluating synthetic data

5.4.1 Database

A database of 41 different model images was created in the ReflexW software. These images were generated by defining a profile of a limestone block with

File	1	2	3	4	5	6	7	8	9	10	File	11	12	13	14	15	16	17	18	19	20
Width (cm)	1	1	1	1	1	0,02	0,05	0,08	2	3	Width (cm)	1	1	1	1	1	0,02	0,05	0,08	2	3
Length (cm)	10	20	30	40	50	30	30	30	30	30	Length (cm)	10	20	30	40	50	30	30	30	30	30
Orientation (°)	0	0	0	0	0	0	0	0	0	0	Orientation (°)	45	45	45	45	45	45	45	45	45	45
File	21	22	23	24	25	26	27	28	29	30	File	31	32	33	34	35	36	37	38	39	40
Width (cm)	1	1	1	1	1	0,02	0,05	0,08	2	3	Width (cm)	1	1	1	1	1	1	1	1	1	1
Length (cm)	10	20	30	40	50	30	30	30	30	30	Length (cm)	30	30	30	30	30	30	30	30	30	30
Orientation (°)	90	90	90	90	90	90	90	90	90	90	Orientation (°)	5	10	20	30	40	50	60	70	80	85

Table 1: Detailed information about the length, width and orientation of each file (1-40) in the database.

	K Method			FK Method			Hyperbola Method			Class-4 Method			Class-6 Method		
Files	ACC	HR	FA	ACC	HR	FA	ACC	HR	FA	ACC	HR	FA	ACC	HR	FA
H	99,67%	88,30%	0,31%	99,65%	91,98%	0,33%	99,84%	33,67%	0,02%	99,81%	75,85%	0,13%	99,80%	69,33%	0,13%
D	99,75%	2,69%	0,01%	99,75%	22,35%	0,07%	99,73%	2,25%	0,02%	99,53%	26,74%	0,28%	99,54%	25,77%	0,27%
V	99,78%	1,47%	0,00%	99,78%	2,30%	0,00%	99,78%	0,84%	0,00%	99,76%	7,52%	0,04%	99,76%	2,53%	0,02%
A	99,68%	37,26%	0,17%	99,71%	40,63%	0,15%	99,78%	9,57%	0,01%	99,52%	46,60%	0,35%	99,58%	41,50%	0,28%
E	100,00%	0,00%	0,00%	100,00%	0,00%	0,00%	100,00%	0,00%	0,00%	100,00%	0,00%	0,00%	100,00%	0,00%	0,00%

Table 2: Mean values of ACC, HR and FA rate for each type of fracture for each method (K, FK, hyperbola, Class-4 and Class-6 methods). 'H' (10 files), 'V' (10 files) ,'D' (10 files) and 'A' (10 files) denote the mean rates for horizontal, vertical, diagonal and varying angle orientation fractures, respectively. 'E' is the only model with no fractures.

fractures of different widths (smaller linear dimension), lengths (larger linear dimension) and orientations.

The information for each file is detailed in Table 1. The first 10 files are horizontal fractures; files 11-20 are diagonal fractures with a tilt angle of 45°; files 21-30 are vertical fractures; and files 31-40 are diagonal fractures with varying slopes (from 5° to 85°). The width of the fractures varies between 0.02 cm and 3 cm, and the lengths range from 10 cm and 50 cm. Finally, file 41, which does not appear in the table, is a perfect section of block without any fractures. All these model images are processed using the ReflexW software to obtain their corresponding radargrams.

5.4.2 Detection

Table 2 reports the migration results (the average for the same type of files) provided by each method when evaluating the database shown in Table 1. For all the simulations, the FA mean is less than 0.35%. Thus, the percentage for highlighting a non-existing fracture is approximately 0%. The results show that FA is always zero when HR is zero, which indicates that Otsu's threshold works properly for detecting fractures. This is because an HR value of zero indicates the non-existence of fractures and a value of FA greater than zero indicates that a fracture is detected incorrectly.

In Table 2, the first two columns correspond to the conventional migration methods (K and FK). The third column shows the results using the hyperbola method (only one kernel based on a hyperbola pattern). The fourth column shows the results of the classification method (hereinafter called Class-4) that uses four patterns or kernels (horizontal, vertical and diagonal 45° and -45°). To evaluate the proposed method when increasing the number of patterns, the fifth column reports the classification method using six patterns at the expense of increased complexity (denoted as Class-6). The goal of using six patterns is to analyse the reconstruction performance to determine whether a larger number of kernels can improve the HR and FA results while covering as many angles as possible. The two new patterns present angles of 10° and -10° to determine whether the algorithm is able to discriminate this small angle diagonal from a horizontal fracture.

Files 1-10 (first row) correspond to horizontal fractures, and HR is relatively high for all these cases. The best performance is achieved with the FK method, followed by the K method. However, FA is slightly higher with these methods. Because of the lateral diagonals and the hyperbolas at the sides of the simulated fracture, the reconstruction is not fully accurate for the SI-PLCA-based methods (both the classification and hyperbola methods). A possible reason for this behaviour is that the proposed methods use kernels that have been cropped to minimize the computation time of the method. Comparing the results obtained using both classification methods shows that HR is slightly higher for the Class-4 method.

For the case of diagonal discontinuities (files 11-20), the Class-6 and Class-4 methods obtain the best HR mean results at the expense of slightly increased FA results. The best of the classic methods is FK migration; the K method does not obtain a satisfactory result. The hyperbola method is unable to detect any diagonal fractures. Comparing both classification methods shows that increasing the number of possible patterns that model diagonal defects does not improve the reconstructed radargram.

The fractures with vertical orientations are the most critical defects because the wave propagation direction is parallel to the orientation of the fracture. In these fractures, the classification methods obtain better performance than the other methods. In addition, the Class-4 method obtains a better HR than the Class-6, FK and K methods. For the two classification methods, using only four kernels provides better HR results, demonstrating

	K Method	FK Method	Hyperbola Method	Class-4 Method	Class-6 Method
H	10	10	10	10	10
D	8	9	7	10	10
V	2	2	2	9	3
A	5	7	5	10	10
E	1	1	1	1	1
Total	26	29	25	40	34

Table 3: Defects detected by each method evaluated. 'H' (10 files), 'V' (10 files), 'D' (10 files) and 'A' (10 files) denote the mean rates for the horizontal, vertical, diagonal and varying angle orientation fractures, respectively. 'E' is the only model with no fractures. For example, the FK method detects 9 of 10 diagonal defects.

that increasing the number of kernels decreases the detection capability.

The diagonals with different slopes show that the classification and conventional migration methods obtain analogous HRs. As an aside, the hyperbola method achieves a very low HR value.

Finally, all the methods obtain a 0% HR and a 0% FA in the last file, which has no defects. Thus, they all produce correct results when there is no fracture.

Therefore, the results indicate that that the proposed methods obtain comparable results to the FK method and outperform the other migration methods evaluated, such as the hyperbola method and the K method. With regard to the number of kernels that should be used by the SI-PLCA algorithm, the results confirm that the energy is dispersed among all the kernels used, which increases complexity and leads to worse results compared to using the minimum number of kernels; in the proposed method, this minimum number is four. As a result, the classification method uses only the previous four kernels.

Table 3 illustrates the number of defects (depending on their spatial orientation) that each method is able to detect (when HR is greater than zero).

The proposed Class-4 method obtains the best detection performance and outperforms all the methods evaluated considering all types of defects. The results show that all methods provide perfect performance when detecting horizontal fractures. However, only the Class-4 method achieves satisfactory performance for vertical fractures. Focusing on defects that show variations in the angle of the diagonal, the Class-4 method detects all the fractures, demonstrating better performance than the other methods.

	Class-4 Method				Template Matching Method			
File	**Horizontal**	**Vertical**	**Diagonal 45°**	**Diagonal -45°**	**Horizontal**	**Vertical**	**Diagonal 45°**	**Diagonal -45°**
1	33,17%	**38,92%**	11,53%	16,37%	27,71%	**35,87%**	22,84%	23,82%
2	**88,05%**	11,95%	0,00%	0,00%	**34,25%**	30,23%	22,24%	23,50%
3	**84,09%**	11,92%	1,49%	2,50%	**32,48%**	31,02%	20,72%	23,44%
4	**79,84%**	14,88%	3,09%	2,19%	**35,05%**	31,37%	19,26%	19,63%
5	**77,79%**	18,02%	1,76%	2,43%	**32,77%**	29,66%	20,75%	20,90%
6	**76,63%**	17,38%	1,64%	4,35%	**32,92%**	32,49%	19,25%	18,94%
7	**76,63%**	17,38%	1,64%	4,35%	**32,92%**	32,49%	19,25%	18,94%
8	**76,63%**	17,38%	1,64%	4,35%	**32,92%**	32,49%	19,25%	18,94%
9	**80,71%**	14,00%	2,50%	2,79%	**32,00%**	29,60%	21,56%	26,10%
10	**75,76%**	17,63%	3,15%	3,47%	**33,11%**	28,54%	21,24%	25,38%
11	0,00%	27,37%	**65,45%**	7,18%	23,28%	29,95%	**38,10%**	10,06%
12	0,00%	14,24%	**85,62%**	0,14%	19,35%	30,14%	**44,11%**	10,93%
13	0,00%	13,22%	**85,68%**	1,10%	19,46%	26,43%	**46,37%**	8,92%
14	0,00%	17,75%	**76,09%**	6,16%	18,89%	28,33%	**43,12%**	9,12%
15	0,00%	14,40%	**79,70%**	5,90%	19,64%	30,11%	**39,95%**	10,97%
16	0,00%	20,04%	**68,52%**	11,45%	19,24%	22,27%	**45,97%**	9,39%
17	0,00%	19,84%	**68,52%**	11,63%	18,76%	21,94%	**43,91%**	9,50%
18	0,00%	15,70%	**82,90%**	1,40%	20,36%	25,53%	**46,72%**	8,92%
19	0,00%	10,94%	**89,01%**	0,05%	19,67%	28,14%	**43,16%**	13,49%
20	0,00%	10,98%	**88,82%**	0,21%	20,59%	28,44%	**41,22%**	15,57%
21	-	-	-	-	**26,62%**	21,05%	18,57%	14,02%
22	11,59%	20,68%	32,36%	**35,37%**	**26,52%**	21,46%	18,69%	13,10%
23	10,29%	21,32%	33,60%	**34,79%**	**25,68%**	25,46%	17,80%	12,31%
24	9,89%	20,56%	33,99%	**35,55%**	**27,82%**	17,67%	18,40%	14,12%
25	10,40%	20,28%	32,39%	**36,93%**	**27,34%**	17,17%	19,66%	13,81%
26	11,27%	20,25%	33,71%	**34,77%**	**25,44%**	22,57%	18,38%	14,58%
27	11,27%	20,25%	33,71%	**34,77%**	**25,44%**	22,57%	18,38%	14,58%
28	11,27%	20,25%	33,71%	**34,77%**	**25,44%**	22,57%	18,38%	14,58%
29	0,00%	**62,01%**	15,98%	22,01%	24,13%	**33,74%**	21,83%	20,22%
30	0,00%	**71,37%**	11,93%	16,71%	22,63%	**34,77%**	24,88%	24,17%
31	**67,90%**	21,48%	3,67%	6,95%	**33,20%**	31,63%	22,40%	20,37%
32	**49,09%**	31,89%	9,37%	9,66%	**33,07%**	31,30%	23,16%	18,08%
33	23,03%	**54,88%**	14,02%	8,07%	28,14%	**33,88%**	27,03%	14,31%
34	8,30%	**51,18%**	28,47%	12,04%	26,61%	**35,98%**	30,24%	10,95%
35	3,54%	33,44%	**46,52%**	16,50%	21,00%	33,35%	**37,48%**	10,98%
36	0,00%	20,81%	**68,64%**	10,55%	19,00%	24,65%	**42,75%**	9,50%
37	1,98%	25,69%	**43,92%**	28,40%	22,94%	**30,43%**	27,78%	12,04%
38	8,28%	21,38%	**39,02%**	31,32%	24,20%	**31,84%**	27,18%	10,08%
39	9,47%	19,87%	**37,49%**	33,17%	22,39%	**27,40%**	22,93%	11,20%
40	8,78%	18,66%	**37,29%**	35,27%	**25,76%**	17,54%	25,09%	12,60%
41	-	-	-	-	**26,85%**	20,10%	18,73%	14,24%

Table 4: Comparison results related to the distribution of the energy provided by the proposed method and the Template Matching method [31].

As mentioned in Section 2, vertical and diagonal fractures are critical, and the Class-4 method is able to detect them well, showing promising results. Moreover, the results highlight the improved performance of the proposed method with four kernels compared to the one with six kernels because the probability of detection for vertical fractures is higher when four patterns are used. Therefore, the proposed method evaluated in the next section is the Class-4 method because it obtained the best detection performance.

5.4.3 Classification

In addition to detecting the fractures, the proposed method is able to discriminate between the spatial orientation of the fractures.

The classification method uses four different kernels; thus, four impulse distribution images (with the contribution of each pattern) can be obtained at the output. The energy of the impulse distribution above the threshold, weighted with its prior, determines whether the fracture is vertical, horizontal or diagonal.

To evaluate these results, it is necessary to display the classification obtained with a pattern recognition method. Therefore, a Template Matching approach [31], as described in Section 1, is applied for the same four patterns.

Table 4 shows the energy distribution of each impulse distribution image (provided that it is above the threshold). The classification method correctly classifies the orientation of the fracture for the horizontal files except for File 1, and the Template Matching method obtains a similar result (with lower probabilities). The fracture in this file is shorter in length than the horizontal kernel of SI-PLCA (see Fig. 5 (A)). In addition, all the diagonal defects (Files 11-20) are correctly classified for both methods. It must be stressed that for the file in which there is no detection of the fracture, no classification is possible, such as for File 21. Files 29 and 30 (vertical fractures with widths greater than 2 cm) are correctly classified. However, Files 22-28 are detected as diagonals by our method (this could be caused by the amplitudes at the sides of the hyperbola, which have a diagonal shape), whereas the Template Matching method classifies them as horizontals. For the diagonal fractures (Files 31-40), if they have a small slope (Files 31 and 32), they are detected as horizontal fractures. In intermediate cases (Files 33 and 34), the methods show that they have a vertical orientation, most likely due to the hyperbolas at the sides of the fracture. Once the angle increases further (Files 35-36), they are classified as diagonals. When increasing the slope (Files 37-39), the proposed method classifies these files as diagonals, whereas the Template Matching method indicates that these are vertical fractures. Finally, the last file is classified by the proposed method as diagonal, whereas the other approach establishes that it is a horizontal fracture, which implies that the proposed method is more reliable.

In most cases, both methods correctly classify the fracture. However, the proposed method is able to detect and classify the defect more accurately. For horizontal, diagonal and vertical fractures, the energy per pattern in the Template Matching Method is dispersed. Therefore, the proposed method can provide higher robustness in the presence of noise. To conclude, the pro-

posed method correctly classifies the orientation of most files with detected fractures. As a result, the proposed method provides a high probability of correct classification of a detected defect.

5.5 Results evaluation on real data

Although the ability of the proposed method to correctly evaluate defects using simulated data has been shown, the objective of this work is to investigate the potential and applicability of GPR systems for real limestone blocks. Therefore, we applied the proposed method to several real limestone blocks. A complete report, which was provided by the factory charged with cutting the block, shows the number of breaks and cracks of each table as well as pictures of the problems encountered. In this way, a reliable comparison can be performed between the actual cutting process of the blocks and the results obtained from the proposed method. In addition, our novel method is able to classify fractures; therefore, 3D maps were created for each type of defect, which is not possible with conventional migration techniques. In this way, users can examine each map of the block and predict its quality.

Two *Crema Marfil* blocks were analysed in this study.

5.5.1 Test

First, a top-quality block of *Crema Marfil* (Block 1 hereafter) with dimensions of 160x300x140 cm (X x Y x Z) was analysed. For the measurement profiles taken every 10 cm, as shown in Fig. 8, we selected a time window of 36 ns. This block has an apparently good quality, and a total of 15 profiles of 10 cm (the approximate width of the antenna) were taken. The cutting process resulted in 46 tables with widths of 3 cm. Thus, 1 profile corresponds to approximately 3 tables. Fig. 8 shows four tables of Block 1 with some minor problems. In general, the tables have only scattered horizontal and diagonal filled fractures that did not cause breakage. The report indicates that the slabs from this block are of high quality.

A second-quality block of *Crema Marfil* (Block 2) with dimensions of 120x260x160 cm (X x Y x Z) was analysed, and some visible fractures were found. The selected time window of the measurement for this block was 39 ns. After the cutting process, 53 tables of 2 cm were obtained. Moreover, 11 profiles of 10 cm were measured along the block. Thus, 1 profile covers 5

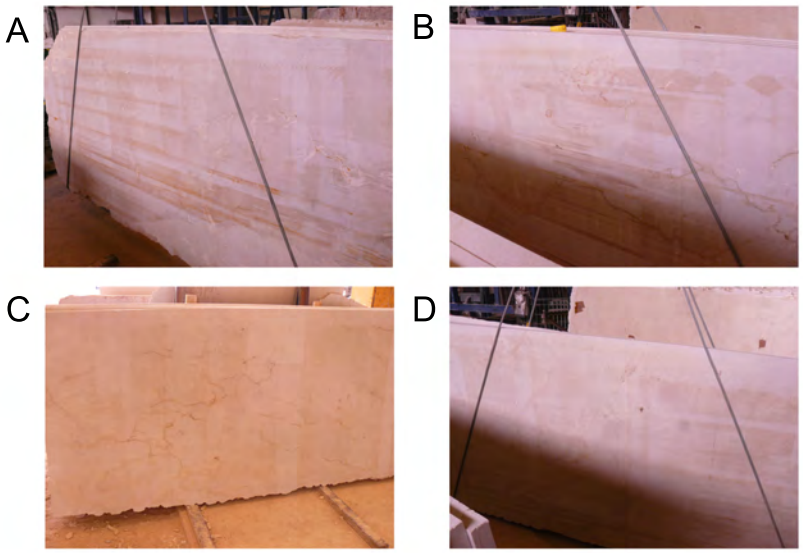

Figure 8: Block 1. (A) Table 1, (B) Table 9 and (C) Table 17, which present some scattered fissures (with a general orientation),(D) Table 36, which generally has high quality.

tables. As shown in Fig. 9, the first three tables suffered from an important vertical break (A) and were completely broken in half. The intermediate tables of the block have other vertical fractures (B) and (C) that did not break the slabs. Finally, the last table has a horizontal fracture, which caused a break (D).

5.5.2 3D maps

First, we tested that the signal emitted by the 800 MHz antenna was able to reach the end of the block despite the strong attenuation in depth.

As explained previously, the classification method is able to correctly classify the types of fractures between horizontal, vertical and 45° and -45° diagonals and is thus quite useful for real limestone blocks. We obtained the different reconstructed radargrams (of each section of the block) following the processes described in Fig. 3 and Fig. 4: pre-processing and migration using the classification method, omitting the thresholding. When working with synthetic data, it is necessary to process the data and to automatically extract metrics to check their behaviour with different orientations. When analysing real blocks, thresholding is not necessary because the general qual-

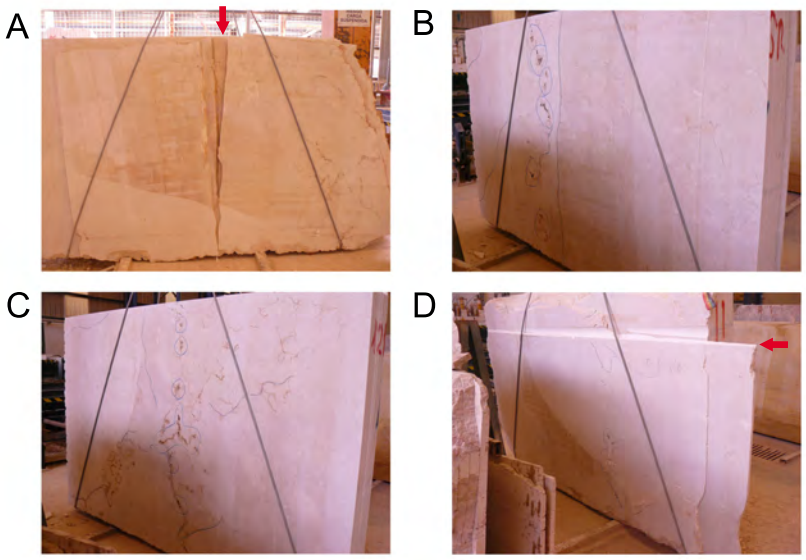

Figure 9: Block 2. (A) Tables 1, 2 and 3 (corresponding to profile 1 for the measurement), which broke in half after the cutting process due to a vertical fracture. (B) Table 15 (profile 3), which has a vertical fracture, a diagonal fracture in the top-left corner, and some small cavities in the left half. (C) Table 39 (profile 8), which has some cavities in the middle and some scattered diagonal cracks. (D) Table 53 (profile 10), which suffered horizontal breaking.

ity status is estimated by the user.

It is possible to extract a 3D map of each located pattern. For this purpose, all the profiles were joined together to process four 3D maps. Fig. 10 presents the 3D map for Block 1, and Fig. 11 displays the diagram of Block 2.

Fig. 10 shows the horizontal map of Block 1 in blue, and some energy can be observed at the end of the block because this interface, called block-ground, is obviously horizontal. Thus, there are no defects inside this block. Analysing the vertical map shown in green shows only one point of energy at the beginning of the block. Finally, the diagonals with tilt angles of 45° (in red) and -45° (in yellow) show no evidence of defects, and the diagonal reflections, due to the contrast between the rock and the air when the antenna reaches the lateral end of the block, are not even present in the map. As a result, this *Crema Marfil* block shows no relevant defects.

For Block 2, which is shown in Fig. 9, the main problem is the critical

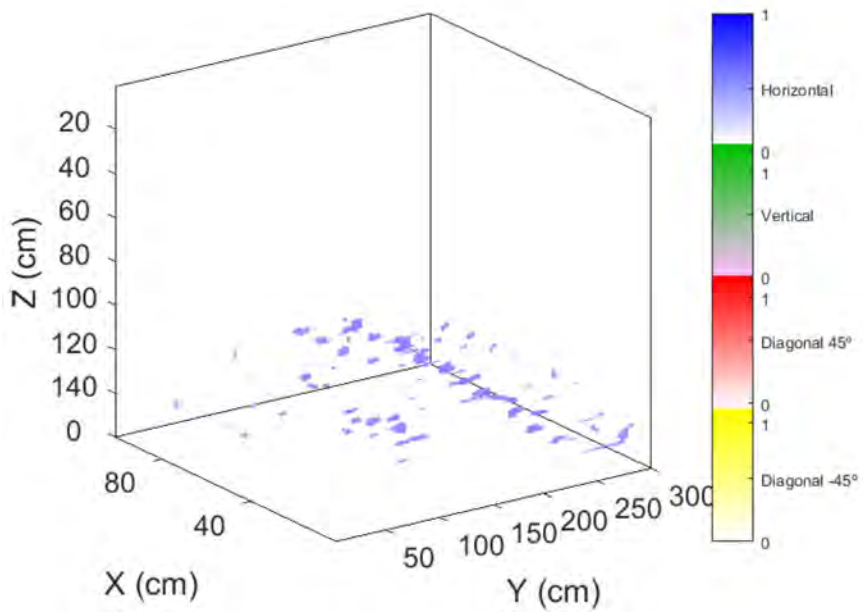

Figure 10: 3D map for Block 1, where blue, green, red and yellow represent horizontal, vertical, diagonal 45° and diagonal -45° fractures, respectively. The profiles are measured along the Y direction (same direction as the cutting of the tables so that a suitable comparison can be performed), from Y=0 to Y=300. The first measured profile occurs at X=10, whereas the final profile is measured at X=150, with a total of 15 profiles.

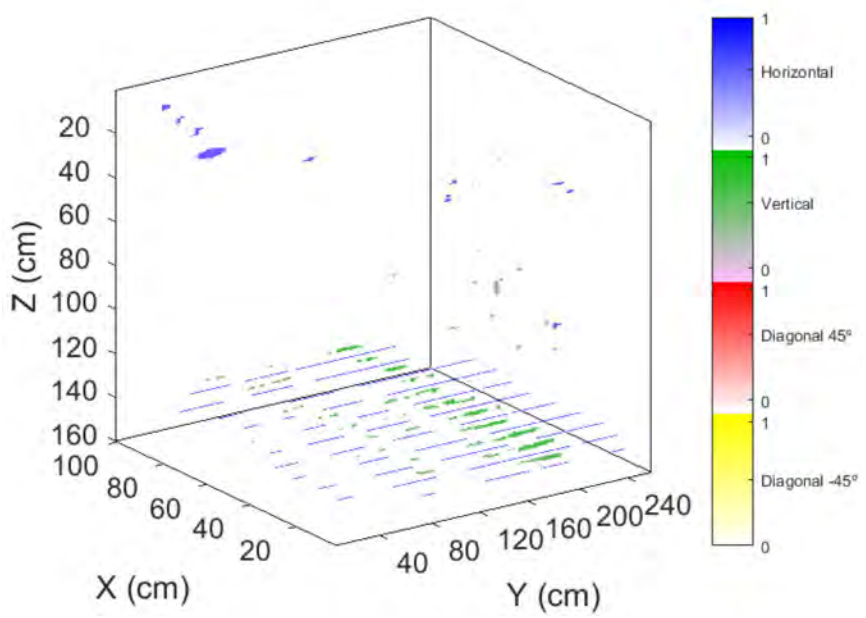

Figure 11: 3D map for Block 2, where blue, green, red and yellow represent horizontal, vertical, diagonal 45° and diagonal -45° fractures, respectively. The profiles are measured along the Y direction (same direction as the cutting of the tables so that a suitable comparison can be performed), from Y=0 to Y=260. The first measured profile occurs at X=10, whereas the final profile is measured at X=110, with a total of 11 profiles.

vertical fracture; this fracture is easy to locate and is displayed in the map related to Fig. 11 in green (Y=120-160 cm). This is consistent with the breaks of the first 3 tables of the block. Moreover, other vertical problems appear but exhibit lower energy. Regarding the horizontal problems (Fig. 11 in blue), we can conclude that part of the energy is observed at the end of the block (X=100 cm, Y=60 cm, Z=30 cm), which seems to be related to the horizontal fracture in the last table. Focusing on the map related to the diagonal fractures shown in red in Fig. 11, some energy is detected in the same zones where there are vertical fractures. This energy confirms our assumption that some important defects, with angles between 45° and 90°, appear during the first part of the block. The last diagram shown in yellow in Fig. 11 (composed of diagonals with a tilt angle of -45°) does not show any problems.

Comparing the two sets of maps shown in Fig. 10 and Fig. 11, both blocks have clearly marked bottoms at the end of the Z direction in the horizontal maps. However, Block 2 presents some horizontal defects and considerable vertical and diagonal defects in other places. As a result, we can relate the obtained 3D maps with the defects encountered after the cutting process. Then, the amplitudes in the horizontal map that model the horizontal fracture can be observed in the last table of Block 2. The vertical and diagonal maps present amplitudes at the beginning of the block that correspond to the broken first tables.

Finally, the results suggest that the information from analysing the 3D maps obtained using the proposed method can quickly evaluate the quality of an actual block. Nevertheless, the user can perform a more detailed analysis of each profile by evaluating its associated two-dimensional radargram.

6 Conclusion and Future Work

In this paper, GPR techniques for evaluating the internal structures of stone blocks are proposed. It is well known that the analysing the structure of blocks (fissures, fractures, cavities, layers, etc.) before performing the block rolling process can facilitate exploitation. Therefore, this analysis can be used to discard blocks directly at the quarry or to optimize the cutting process via reductions in the cut velocity to avoid breaking the blocks. Moreover, block handling can be varied during cutting when there is the

possibility of applying resins to consolidate the block.

First, an 800 MHz antenna was selected for the proposed GPR campaign, which seems to be appropriate given the reasonably good resolution obtained in synthetic and real-world cases. The simulations demonstrated that this antenna can detect vertical fractures (the most critical orientation) with widths of 2 cm. Second, the proposed framework for processing GPR signals, composed of pre-processing, migration and thresholding stages, was able to reliably estimate the existence of fractures using simulated data.

We propose a novel migration method for GPR radargrams using the SI-PLCA algorithm to improve the detection of defects and the classification of their spatial orientation in damaged materials such as ornamental stone blocks. Specifically, the proposed method is based on training fractures with a variety of orientations (vertical, horizontal and diagonals) to obtain a pattern for each orientation fracture. Then, each radargram is analysed, and the SI-PLCA method provides information about the amplitude associated with each pattern at each position of the block. Using this technique, we not only predicted the existence of fractures with similar accuracy to that of classical migration methods but also obtained a 3D map that provides information about the fractures for each orientation pattern. This classification of fractures depending on the spatial orientation is a novel result in GPR signal processing.

The proposed method was tested using state-of-the-art migration and classification methods to evaluate both simulated and real data. The results are promising because the proposed method outperformed the detection and classification performance of the compared methods. For instance, the proposed model obtains the best detection performance when the fracture has a vertical orientation, which is the most critical spatial orientation. Moreover, the classification performance of the proposed model is more robust because the energy per pattern is not dispersed.

Future work will focus on extending our real data measurements to different types of stones. Moreover, measurements on three block faces will be performed to analyse correlations between the different spatial orientations and to improve the accuracy of the 3D maps. Finally, 3D reconstruction will be considered for other applications, such as archaeological studies.

Acknowledgement

This work was performed using funds provided by the Andalusian Business, Science and Innovation Council under Project P11-TIC-7278. The authors are grateful to the Advanced Technology Center for Stone (CTAP) in Macael (Almería, Spain) for their support during data acquisition and the evaluation of the final results.

References

[1] Arosio D., Munda S., Zanzi L., "Quality control of stone blocks during quarrying activities", *14th International Conference on Ground Penetrating Radar (GPR)*, Shangai, China, 2012.

[2] Bee Bednar J., "Modeling, Migration and Velocity Analysis in Simple and Complex Structure", 1st ed. Panorama Technologies, 2008.

[3] Cañaveras J.C., García del Cura M.A., Sánchez-Moral S., Muñoz-Cervera M.C., Ordóñez S., "Procesos de karstificación polifásica en las canteras de Crema Marfil (Pinoso, Alicante). Aplicación a la explotación de rocas ornamentales", *Geogaceta*, vol. 31, pp. 31-34, 2002.

[4] B. Carlson, *Communications Systems, An Introduction to Signals and Noise in Electrical Communication*, McGraw-Hill International Editions, 3rd ed., pp. 196-199, (1986).

[5] Cerrillo C., Jiménez A., Rufo M., Paniagua J., Pachón F.T., "New contributions to granite characterization by ultrasonic testing", *Ultrasonics*, vol. 54, pp. 156–167 (2014).

[6] Daniels D. J., "Ground Penetrating Radar", 2nd ed. *The Institution of Electrical Engineers*, London, UK, 2004.

[7] De Domenico D., Campo D., Teramo A., "FDTD modelling in high-resolution 2D and 3D GPR surveys on a reinforced concrete column in a double wall of hollow bricks", *Near Surface Geophysics*, vol. 11, pp. 29–40, 2013.

[8] Gallego CoidurasI.C. , García de Domingo A., López Olmedo F., "Mapa Geológico de España 1:50.000", hoja 870 (Pinoso), Instituto Tecnológico y Geológico de España, 1981.

[9] Gilmore C. G., "A Comparison of Imaging Methods using GPR for Landmine Detection and A Preliminary Investigation into the SEM for Identification of Buried Objects", PhD Thesis, University of Manitoba, Winnipeg, Manitoba, Canada, 2004.

[10] Grandjean G., Gourry J.C., "GPR data processing for 3D fracture mapping in a marble quarry (Thassos, Greece)". *Journal of Applied Geophysics*, vol. 36, pp. 19–30, 1996.

[11] Jerez Mir L., Jerez Mir F., García Monzón G., "Mapa Geológico de España 1:50.000", hoja 891 (Cieza), Instituto Tecnológico y Geológico de España, 1982.

[12] Jol H. M., "Ground Penetrating Radar Theory and Applications", 1st ed. Elsevier Science, USA, 2008.

[13] Jolliffe I. T., Stephenson D. B., "Forecast Verification: A Practitioner's Guide in Atmospheric Science", 2nd Edition, 2011.

[14] Kadioglu S., "Photographing layer thicknesses and discontinuities in a marble quarry with 3D GPR visualisation", *Journal of Applied Geophysics*, vol. 64, pp. 109–114, 2008.

[15] Khan U., Al-Nuaimy W., "Background removal from GPR data using Eigenvalues", *13th International Conference on Ground Penetrating Radar (GPR)*, Lecce, Italy, 2010.

[16] King B., Smaragdis P., Mysore G.J., "Noise-robust dynamic time warping using PLCA features", *Proceedings of the IEEE International Conference on Acoustics, Speech and Signal Processing*, Kyoto, Japan, 2012.

[17] Luodes H., "Natural stone assessment with ground penetrating radar", *Estonian Journal of Earth Sciences*, vol. 57, n. 3, pp. 149–155, 2008.

[18] Nam J., Mysore G.J., Smaragdis P., "Sound recognition in mixtures", *Proceedings of the international conference on Latent Variable Analysis/Independent Component Analysis*, Tel-Aviv, Israel, 2012.

[19] Onur A.H., Bakrac S., "Determination of discontinuities in marble blocks via a nondestructive ultrasonic technique", *Int J Miner Metall Mater*, vol. 16, pp. 487-493, 2009.

[20] Onur A.H., Bakrac S., Karakus D., "Ultrasonic Waves in Mining Application", 1st ed. A. A. dos Santos, 2012.

[21] Otsu N., "A Threshold Selection Method from Gray-Level Histograms", *IEEE Trans. Syst., Man, Cybern., Syst.*, Vol. SMC-9, No. 1, January 1979.

[22] Ozdemir C., Demirci S., Yigit E., "A Review on the Migration Methods in B-scan Ground Penetrating Radar Imaging", *Progress in Electromagnetics Research Symposium Proceedings*, KL, Malaysia, pp. 27–30, 2012.

[23] Pasolli E., Melgani F., Donelli M., "Automatic Analysis of GPR Images: A Pattern-Recognition Approach", *IEEE Transactions on Geoscience and Remote Sensing*, vol. 47, no. 7, 2009.

[24] Porsani J. L., Sauck W. A., Junior A. O. S., "GPR for mapping fractures and as a guide for the extraction of ornamental granite from a quarry: A case study from southern Brazil", *Journal of Applied Geophysics*, vol. 58, pp. 177-187, 2006.

[25] RadExplorer Software, MALA GeoScience, 2016, URL: *http://www.malags.com/products/mala-radexplorer* [accessed: 2016-20-04].

[26] ReflexW Software, Sandmeier Geophysical Research, 2016, URL: *http://www.sandmeier-geo.de/reflexw.html* [accessed: 2016-20-04].

[27] Rey J., Martínez J., Vera P., Ruiz N., Cañadas F., Montiel V., "Ground-penetrating radar method used for the characterisation of ornamental stone quarries", *Construction and Building Materials*, vol. 77, pp.439-447, 2015.

[28] Robinson M., Bristow C., McKinley J., Ruffell A., "Ground Penetrating Radar", *Geomorphological Techniques*, Part 1, Sec. 5.5, 2013.

[29] Saez-Perez M.P., Rodriguez-Gordillo J., "Structural and compositional anisotropy in Macael marble (Spain) by ultrasonic, x-rd XRD and optical microscopy methods", *Constr Build Mater*, vol. 23, pp .2121–2126, 2009.

[30] Sarpun I.H., Kilickaya M.S., "Mean grain size determination in marbles by ultrasonic first backwall echo height measurements", *NDTE Int*, vol. 39, pp. 82–86, 2006.

[31] Sezgin M., "Two dimensional Template Matching method for buried object discrimination in GPR data", *Proceedings of SPIE - The International Society for Optical Engineering 7303*, 2009.

[32] Schneider W.A, "Integral formulation for migration in two and three dimensions", *Geophysics*, vol. 43, pp. 49–76, 1978.

[33] Scott A. H., "Dielectric constant, power factor, and resistivity of Marble", *Part of Journal of Research of the National Bureau of Standards*, March 1940.

[34] Sigurdsson T., "Ground penetrating radar for geological mapping", PhD Thesis, Arhus University, Arhus Geoscience, 1995.

[35] Sigurdsson T., Overgaard T., "Application of GPR for 3-D visualization of geological and structural variation in a limestone formation", *Journal of Applied Geophysics*, vol. 40, pp. 29–36, 1998.

[36] Smaragdis P., Raj B., "Shift-Invariant Probabilistic Latent Component Analysis", Tech report, 2007.

[37] Solimene R., Cuccaro A., DellAversano A., Catapano I., Soldovieri F., "Ground Clutter Removal in GPR Surveys", *IEEE Journal of Selected Topics in Applied Earth Observations and Remote Sensing*, vol. 7, no. 3, 2014.

[38] Stolt R.H., Weglein A.B., "Migration and inversion of seismic data", *Geophysics*, vol. 50, no. 12, 1985.

[39] Vaccaneo D., Sambuelli L., Marini P., Tascone R., Orta R., "Measurement System of Complex Permittivity of Ornamental Rocks in L Frequency Band", *IEEE Transactions on Geoscience and Remote Sensing*, vol. 42, no. 11, 2004.

[40] Valle S., Zanzi L., Sgheiz M., Lenzi G., Friborg J., "Ground Penetrating Radar Antennas: Theoretical and Experimental Directivity Functions", *IEEE Geosci. Remote Sens.*, vol. 39, no. 4, 2001.

[41] Vergara L., Gosalvez J., Fuente J. V., Miralles R., Bosch I., Salazar A., López A.M., López L.E., "Ultrasonic nondestructive testing on marble rock blocks", *Materials Evaluation*, 2002.

[42] Yilmaz O., "Seismic Data Processing", *SEG*, 1987.

Paper C

A novel method to remove GPR background noise based on the similarity of non-neighboring regions

Montiel V., Cañadas F., Vera P., Ruiz N., Rey J., Martínez J., "A novel method to remove GPR background noise based on the similarity of non-neighboring regions", *Journal of Applied Geophysics*, under review.

Abstract

Ground penetrating radar (GPR) is a non-destructive technique that has been widely used in many areas of research, such as landmine detection or subsurface anomalies, where it is required to locate targets embedded within a background medium. One of the major challenges in GPR research remains the improvement of the image quality of stone materials by means of detection of true anisotropies since most of the errors are caused by an incorrect interpretation by the users. However, it is complicated due to the interference of the horizontal background noise, e.g., the air-ground interface, that reduces the high-resolution quality of radargrams. Considering the entire radargram, weak or deep anisotropies located at different depth of the background noise can be masked. However, most of anisotropies that are located at the same depth as the background noise often show similar or predominant energy compared to this type of noise. In order to enhance the image quality of the GPR radargrams, this work proposes a novel background removal method assuming that the horizontal noise shows repetitive two-dimensional regions along the movement of the GPR antenna. Specifically, the proposed method, based on the non-local similarity of regions over the distance, computes similarities between different regions at the same depth. In this manner, most repetitive regions are identified using a criterion to avoid closer regions. Evaluations are performed using a set of synthetic and real GPR data. Experimental results show that the proposed method obtains promising results compared to the classic background removal techniques and the most recently published background removal methods.

Key words: *Ground penetrating radar (GPR), background, horizontal noise, radargram, region, similarity, non-neighboring*

1 Introduction

Ground penetrating radar (GPR) is a geophysical and non-destructive technique applied in different areas of research such as archaeology [1], building construction [2], landmine detection [3] or analysis and characterisation of stone materials [4] [5] [6]. In general, GPR is used because it provides accu-

rate spatial location of targets from high-resolution images in short periods of time at affordable cost. Focusing on the stone materials, one of the major challenges in the analysis of GPR data remains to detect true anisotropies (e.g., cavities, holes, fractures or discontinuities) to minimize incorrect interpretations since most of the time the interpretation is based on the GPR experience of the user.

GPR background noise (non-target) can be defined as a type of horizontal noise active in almost all GPR data. This noise can be considered approximately flat and smooth most of the time, showing more or less continuity along the traces. Moreover, it shows a quasi-periodic pattern in the direction perpendicular of the surface. As a result, it draws horizontal lines in the direction of the movement of the antenna as shown in Fig. 1. The effect of the noise is the reduction of the image quality obtained by GPR [7]. Some causes of this noise are the scattered signals from closer objects or the reflection from the air-ground interface [8] [9] that complicate the detection of true defects.

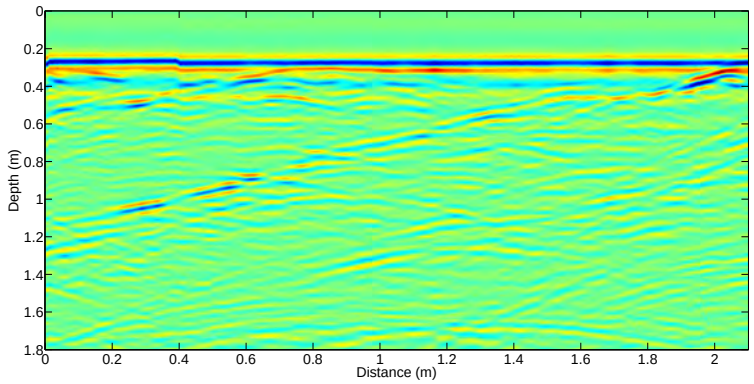

Figure 1: *Radargram of a real block of stone (Crema Marfil) obtained by GPR from a marble quarry located in Pinoso (Alicante, Spain). The horizontal noise can be observed at a depth from 0.22 m to 0.34 m*

Although one of the most reference method to remove GPR background noise is the average trace subtraction (ATS) [10], it is well-known that it is not a robust background removal evaluating rapid variations of horizontal noise because the local data used by ATS can be highly corrupted by outliers so, the anisotropies are distorted. This fact implies that the average energy value is composed of energy from background noise and anisotropies.

As a result, ATS degrades the true anisotropies intend of keeping the original features of them. Several approaches have been published in the last decades in order to improve the GPR background removal, such as parametric system identification [11], filtering [12] [13] [14], wavelet domain [15] [16], likelihood processing [17], ICA [18], deterministic deconvolution [19], Eigenimage processing [20] [21] and PCA [22]. Recently published state-of-the-art techniques are presented in [23] [24]. Specifically, Rashed [23] presents the background matrix subtraction (BMS) technique based on calculating a complete background matrix through a series of windowing, sample exclusion, weighting, and iteration. These series of processes guarantee that the background matrix is least affected by target response and is composed purely of horizontal background noise. In [24], a directional total variation minimisation (DTVM) algorithm is proposed based on the principle of reducing the global variation of a signal, while preserving a close match to its original form.

In this paper, we propose a novel, efficient and fast method to remove the background noise in GPR data. Specifically, the proposed method is based on exploiting the repetitive pattern shown by the horizontal noise in the direction of the movement of the antenna. From a region obtained by GPR, we search repeating regions over the distance at the same depth. A region could be considered as horizontal noise when its spatial similarity compared with another regions not neighboring be sufficiently similar. In this manner, regions mainly composed of horizontal background noise show higher spatial similarity between them. However, regions mainly composed of anisotropies show lower similarity due to the particularity of the each target along the traces. Experimental results, using both synthetic and real GPR data, are evaluated comparing the performance of the proposed method with the reference average trace subtraction technique (ATS) and recent state-of-the-art background removal methods [23] [24].

The remainder of this paper is organized as follows. In Section 2, the proposed method is detailed. Section 3 optimizes and evaluates the background removal performance of the proposed method compared to recent state-of-the-art methods using both synthetic and real GPR data. Finally, conclusions and future work are presented in Section 4.

2 Proposed method

The goal of the proposed method is to remove the horizontal background noise preserving the true anisotropies obtained by GPR. The proposed method is based on two observations: (i) the horizontal background noise can be modeled as a repetitive pattern in the direction of the movement of the antenna so, it draws horizontal lines across the traces; (ii) it can be assumed that most of anisotropies that are located at the same depth as the horizontal background noise often show similar or predominant energy compared to this type of noise. Three situations can occur comparing regions not neighboring: (1) regions mainly composed of horizontal noise show high similarity between them due to the feature of repeatability; (2) regions mainly composed of anisotropies show low similarity due to the specific spatial location and geometry of each anisotropy; (3) regions composed of anisotropies and horizontal noise must be appropriately processed (detailed in section 2.3) computing a model of background noise based on the fact that the energy of a anisotropy located at the same depth as the background noise often shows similar or predominant energy compared to this noise. The proposed method consists of three stages: segmentation, similarity-repeatability and non-neighboring constraint. Each stage is detailed in this section. The proposed background noise removal is provided in the flowchart in Fig. 2.

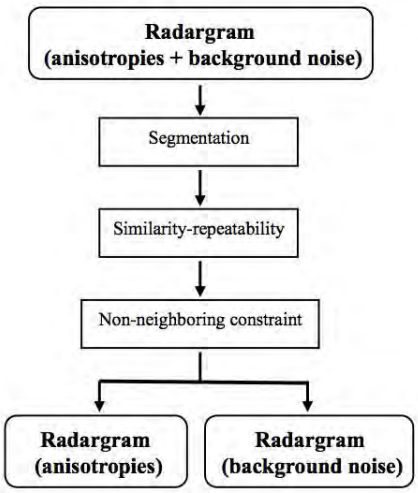

Figure 2: *Flowchart of the proposed horizontal background removal*

2.1 First stage: Segmentation

A radargram is a depth versus distance representation of GPR data. Each input radargram X, mixture of anisotropies and horizontal background noise, can be modeled by two separate radargrams: X_a (only composed of anisotropies) and X_n (only composed of horizontal background noise) as eq. (1). We assume that each of these radargrams exhibits the specific features shown by the anisotropies and horizontal background noise.

$$X(p,d) = X_a(p,d) + X_n(p,d) \tag{1}$$

where $p = 1,...,F$ rows related to penetration depth, $d = 1,...,T$ columns related to distance or traces and $F \cdot T$ elements. Therefore, the dimensions p (penetration depth) and d (distance) are designated as the up-down and left-right dimensions shown previously in Fig. 1.

The concepts of section and region are introduced in order to segment the input radargram X. The relationship between section and region is shown in Fig. 3. The $i-th$ section is defined as a submatrix S_i (see eq. (2)) composed of T_V rows and T columns (traces) of the input radargram X. In this manner, a set of $R_F = \frac{F}{T_V}$ non-overlapped sections are computed,

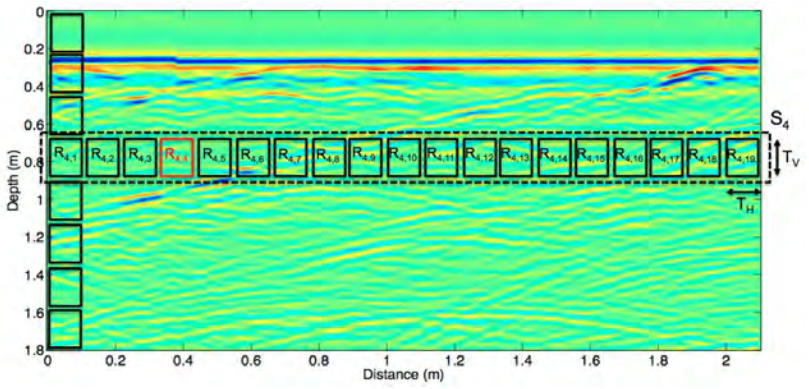

Figure 3: *The segmentation process. This radargram is composed of eight sections ($S_1,...,S_8$) but only the fourth section S_4, composed of nineteen regions ($R_{4,1},...,R_{4,19}$), is detailed. The entire radargram is segmented into 152 regions.*

$$
\begin{aligned}
S_i &= X(p_i, d) \\
&\quad i \in [1, R_F],\ p_i \in [(i-1)\cdot T_V + 1, i \cdot T_V], \\
&\quad d \in [1, T]
\end{aligned}
\tag{2}
$$

The j^{th} region $R_{i,j}$ belonging to the section S_i is defined as a submatrix composed of T_V rows and T_H columns as shown in eq. (3). Thus, each section is partitioned using $R_C = \frac{T}{T_H}$ non-overlapped regions,

$$
\begin{aligned}
R_{i,j} &= X(p_i, d_j) \\
&\quad i \in [1, R_F],\ p_i \in [(i-1)\cdot T_V + 1, i \cdot T_V] \\
&\quad j \in [1, R_C],\ d_j \in [(j-1)\cdot T_H + 1, j \cdot T_H]
\end{aligned}
\tag{3}
$$

At the end of this stage, the input radargram X is segmented using a total number of $R_T = (R_F \cdot R_C)$ regions of size T_V rows of depth penetration and T_H traces of distance.

2.2 Second stage: Similarity-repeatability

Based on the first assumption previously mentioned, this stage attempts to model a radargram only composed of horizontal background noise. To this end, the goal is to identify regions candidates in which the horizontal noise is active mixed or not with anisotropies. Because the horizontal noise shows a repetitive pattern along the distance, this similarity implies repeatability and vice versa. A radargram only composed by anisotropies cannot be considered repetitive along the distance because the energy distribution related to these anisotropies can be considered approximately random dependent on the exact spatial location and geometry from each of them. We propose a criterion, based on the similarity of a region respect to the other ones of the same section, to identify noisy regions. In this manner, high values of similarity seem to indicate high probability of repetition being the repetition an useful characteristic to discriminate horizontal noise from anisotropies. Finally, the radargram of noise extracted could be modeled estimating how much horizontal background noise is active in each noisy candidate region.

For each region $R_{i,j}$, a measure of similarity $M_{i,j,z}$ is computed taking into account $R_{i,j}$ and a set of regions defined by a moving window $V_{i,z}$ that is slided horizontally along the distance using shifts of one column. In the computation of the similarity $M_{i,j,z}$, the sizes of $R_{i,j}$ and $V_{i,z}$ are the same

and $V_{i,z} \notin R_{i,j}$. Several measures such as the cosine similarity (COS), the Euclidean distance (EUC), the Kullback-Liebler (KL) divergence and their normalized versions were evaluated. Preliminar results showed that EUC normalized provides the best quality and lowest computational cost. For this reason, EUC normalized has been used in this work. It is computed using the normalized radargram $\overline{X}$ that gives the same importance to each trace, that is, the L^2-norm of each trace is equal to 1.0 (see eq. (4)). As a result, a normalized region $\overline{R}_{i,j}$ is extracted from the normalized radargram and the similarity $M_{i,j,z}$ is computed as shown in eq. (5),

$$\overline{X}(p,d) = \frac{X(p,d)}{\sqrt{\sum_{p=1}^{F} X^2(p,d)}} \tag{4}$$

$$M_{i,j,z} = \|\overline{R}_{i,j} - \overline{V}_{i,z}\|^2 \tag{5}$$

Fig. 3 shows $\overline{R}_{4,4}$ (red square) as the region for which potential noise candidates must be identified along the distance. In this example, only some of the moving windows $\overline{V}_{4,z}$ are shown as black squares. Specifically, these particular set of windows $\overline{V}_{4,z}$ coincide with the regions $\overline{R}_{4,j}$, $j \in [1,4) \cup (4,19]$.

2.3 Third stage: Non-neighboring constraint

This stage is critical in the proposed method. Although a high similarity is necessary to identify candidates regions $\overline{V}_{i,z}$ which are mainly composed of horizontal noise, it is not a sufficient condition. It is due to consecutive regions of small size only composed of anisotropies could provide high values of similarity. This fact indicates that not always a high value of similarity implies a valid candidate to model background noise. Although the local similarity, using neighboring regions, provides satisfactory results evaluating regions only composed of noise, this similarity does not provide satisfactory results evaluating regions not only composed of noise. The reason is because the horizontal noise is characterized by a repetitive pattern that can be observed in neighboring and non-neighboring regions along the traces. However, regions without noise are characterized by a non-repetitive pattern in neighboring regions along the traces. To overcome this problem, we propose to apply a constraint that excludes the neighboring regions to $R_{i,j}$. The identification of the optimal region $\overline{V}_{i,o}$, that minimizes the background

noise of the region of interest $\overline{R}_{i,j}$, is computed solving the minimization problem shown in eq. (6) in which the constraint has been applied. Specifically, the regions $\overline{V}_{i,z}$ associated to $\overline{R}_{i,j}$ are defined as the set of regions separated, at least, U_m traces from the region of interest. Experimental results showed that the optimal region $\overline{V}_{i,o}$ is the non-neighboring region that obtains the highest similarity satisfiying the previous constraint.

$$\overline{V}_{i,o} = \underset{\overline{R}_{i,z},|z-j|\geq\lceil U_m\rceil}{\arg\min} M_{i,j,z}, \tag{6}$$

More details can be found in section 3.1.4 in which an optimization analysis of the parameter U_m is performed to maximize the background removal performance of the proposed method.

Once the optimal region $\overline{V}_{i,o}$ belonging to the region of interest $\overline{R}_{i,j}$ has been identified, the estimation of the horizontal background noise $\overline{R}_{i,n}$ is computed in eq. (7). This calculation, based on the second assumption previously mentioned, assumes that the energy of most of anisotropies located at the same depth as the background noise often shows similar or predominant energy compared to this noise.

$$\overline{R}_{i,n} = min(\overline{R}_{i,j}, \overline{V}_{i,o}) \tag{7}$$

To ensure that the background removal process is conservative, the estimation of the anisotropies $\overline{R}_{i,a}$ is computed as follows,

$$\overline{R}_{i,a} = \overline{R}_{i,j} - \overline{R}_{i,n} \tag{8}$$

Considering eq. (7), three scenarios can be considered: (i) both regions $\overline{R}_{i,j}$ and $\overline{V}_{i,o}$ are mainly composed of horizontal background noise. In this context, the use of the minimum value, between $\overline{R}_{i,j}$ and $\overline{V}_{i,o}$, keeps most of the noise active because most of the elements are very similar; (ii) both regions $\overline{R}_{i,j}$ and $\overline{V}_{i,o}$ are mainly composed of anisotropies. Here, the use of the minimum value between $\overline{R}_{i,j}$ and $\overline{V}_{i,o}$ removes most of the anisotropies since it is unlikely to compare identical elements in these regions due to the singularity of each anisotropy; (iii) $\overline{R}_{i,j}$ and $\overline{V}_{i,o}$ are composed of anisotropies and noise. The use of the minimum value between $\overline{R}_{i,j}$ and $\overline{V}_{i,o}$ attenuates the effect of the noise because we have observed that the energy of the anisotropies is often similar or predominant compared to the energy of the

horizontal background noise located at the same depth as these anisotropies.

3 Evaluation

3.1 Synthetic data

3.1.1 Test data

The background removal performance of the proposed method is first evaluated using synthetic data. For this purpose, an initial synthetic database has been created with ReflexW commercial package [25]. This software consists on geophysical near-surface processing and interpretation, based on the Finite-Different Time-Domain (FDTD) method, which obtains quasi-real results [26]. The noise-free synthetic database is composed of ten velocity models that are generated by defining a block of stone with a dimension of 1.5 m (depth, 2187 rows) × 2 m (distance, 401 scans, columns or traces) using different relative permittivity and zero conductivity as shown in Fig. 4. Once the models are created, the noise-free synthetic radargrams are obtained using the following operating parameters: nominal frequency of 800 MHz, distance interval of 0.005 m (according to the Nyquist theorem [26]) and sampling frequency of 62.5 GHz (this frequency is established by default by the ReflexW software).

Due to horizontal background noise can appear more or less continuous in the direction of the movement of the antenna, it is common the presence of different areas in which the background noise does not draw purely constant horizontal patterns along the traces. For this reason, the background noise, created by the software ReflexW and modeled as horizontal strips, is generated simulating four common types of synthetic horizontal noises shown in Fig. 5. Assuming movement along the distance of the block of stone, the noise N_A is modeled by constant amplitude, N_B is modeled by variable amplitude, N_C is modeled using variable amplitude with alternated positive and negative values and N_D is modeled by amplitude with sinousoid variation. In any case, each type of the previous synthetic noise has been modeled using variable amplitude in penetration depth simulating the energy decrease of the wave as penetration increases. As a result, the initial synthetic database is composed of forty evaluation files, one file for each combination between velocity model and type of noise as can be observed

in Table 1.

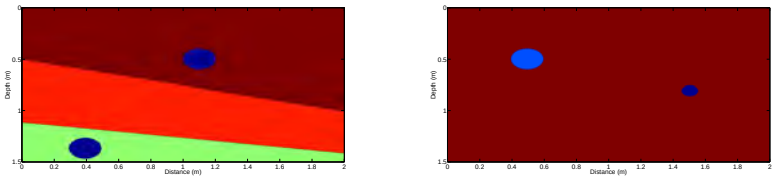

(a) Model 1

(b) Model 2

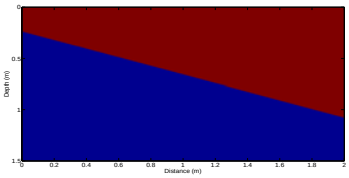

(c) Model 3

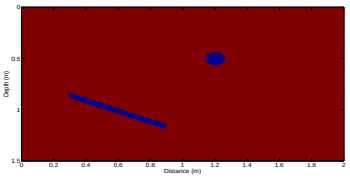

(d) Model 4

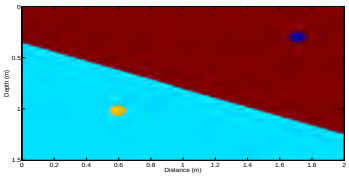

(e) Model 5

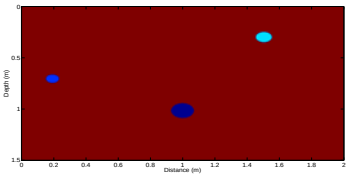

(f) Model 6

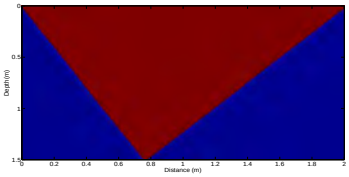

(g) Model 7

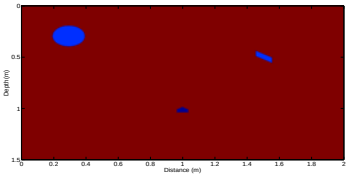

(h) Model 8

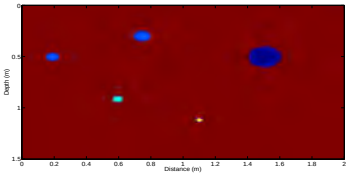

(i) Model 9

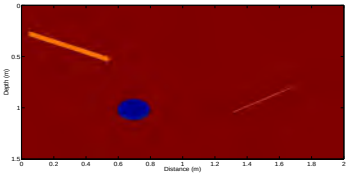

(j) Model 10

Figure 4: *The set of velocity models related to each block of the synthetic database. Each block has a dimension of 1.5 m (depth, 2187 rows) × 2 m (distance, 401 traces)*

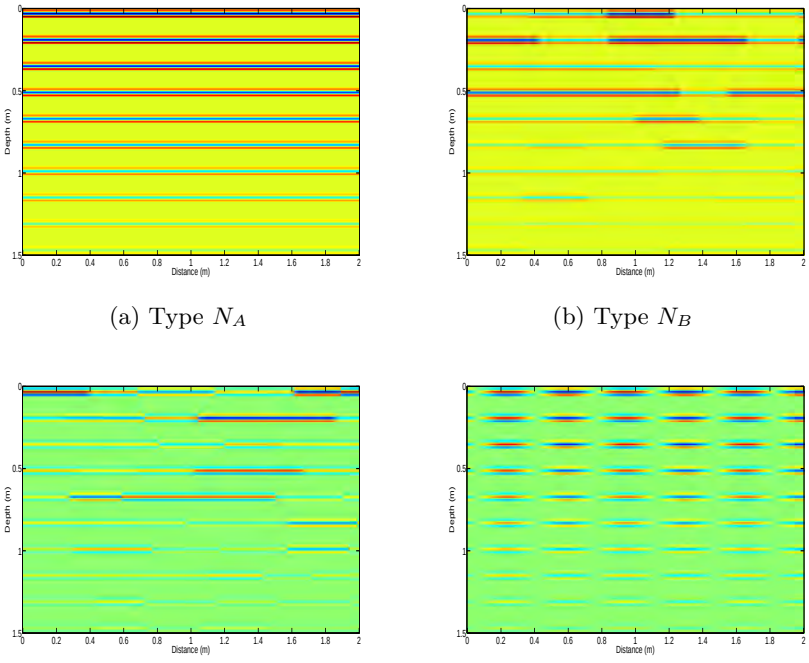

(a) Type N_A (b) Type N_B

(c) Type N_C (d) Type N_D

Figure 5: *Types of horizontal synthetic noises*

Table 1: The set of evaluation files that compose the initial synthetic database. An identifier is used to select each combination between velocity model and type of synthetic noise

Identifier	Velocity model	Type of synthetic noise	Database
F1, F2, F3, F4	M1	N_A, N_B, N_C, N_D	Test
F5, F6, F7, F8	M2	N_A, N_B, N_C, N_D	Test
F9, F10, F11, F12	M3	N_A, N_B, N_C, N_D	Test
F13, F14, F15, F16	M4	N_A, N_B, N_C, N_D	Test
F17, F18, F19, F20	M5	N_A, N_B, N_C, N_D	Development
F21, F22, F23, F24	M6	N_A, N_B, N_C, N_D	Development
F25, F26, F27, F28	M7	N_A, N_B, N_C, N_D	Development
F29, F30, F31, F32	M8	N_A, N_B, N_C, N_D	Development
F33, F34, F35, F36	M9	N_A, N_B, N_C, N_D	Development
F37, F38, F39, F40	M10	N_A, N_B, N_C, N_D	Development

The synthetic database is partitioned into two different databases: development and test. The development database, composed of approximately

the two-thirds of the synthetic database (24 files, from file F17 to F40), is used to optimize the parameters T_V, T_H and U_m. The test database, composed of the remainder one-third of the database (the first 16 files, from file F1 to F16), is used to evaluate the performance of the proposed method. Note that the development database is not a part of the test database in order to validate the results.

3.1.2 Metrics

Each background removal method provides as output two estimated radargrams: $\hat{X}_a$ (only composed of anisotropies) and $\hat{X}_n$ (only composed of the background noise).

The relative root mean square error (RRME) [24] is a quantitative metric used to assess the performance of the proposed method. Specifically, RRME (see eq. (9)) measures the relative root mean square error between the noise-free synthetic radargram X_a and the estimated noise-free radargram $\hat{X}_a$ provided by each background removal method.

$$RRME = \sqrt{\frac{\sum_{p=1}^{F}\sum_{d=1}^{T}\left(\hat{X}_a(p,d) - X_a(p,d)\right)^2}{\sum_{p=1}^{F}\sum_{d=1}^{T}X_a^2(p,d)}} \tag{9}$$

Higher quality of the estimated noise-free radargram is obtained as smaller the value of RRME (>0), showing better performance in the task of the horizontal background removal.

3.1.3 State-of-the-art methods

The background removal performance of the proposed method has been evaluated using most frequently used and some of the most recently published techniques. Consequently, the state-of-the-art methods ATS [10], BMS [23] and DTVM [24] have been used. The method ATS has been implemented in this work whereas the methods BMS and DTVM have been directly obtained from their authors.

3.1.4 Parameters optimization

Prior to the performance comparison with most frequently and recent published methods, we have determined the optimization of the parameters for

the proposed method using the development set. Specifically, the proposed method depends on the parameters (T_V, T_H) related to the size of the region $\overline{R}_{i,j}$ and the non-neighboring constraint using the parameter U_m. Performing a hyperparametric analysis evaluating approximately until the half of the size of the block previously mentioned by means of $T_V \in [10, 1500]$ rows, $T_H \in [10, 140]$ traces and $U_m \in [1, 140]$ traces. Next, the RRMEs are calculated for each file of the development database and are averaged for each combination of values T_V-T_H-U_m. Results showed that the highest quality of the estimated free-noise radargram $\hat{X}_a$ is obtained using the optimal values T_{V_o} = 100, T_{H_o} = 20 and U_{m_o} = 40. From this optimal configuration T_{V_o}- T_{H_o}-U_{m_o}, a more detailed study using the development database is conducted below in order to analyze both the effect of the size of region and the non-neighboring constraint in the background removal procedure.

Fig. 6 shows the RRME results of the proposed method keeping fixed the optimal parameter U_{m_o} = 40 and varying the values T_{V_o}, T_{H_o} to measure the importance of the size of region. It can be observed that the minimum RRME is obtained using T_{V_o} = 100 and T_{H_o} = 20. However, the quality of estimated noise-free radargram seems to reduce for $T_V >> 1$ or $T_H >> 1$ because the effect of the non-neighboring constraint would be less significant evaluating higher sizes of region.

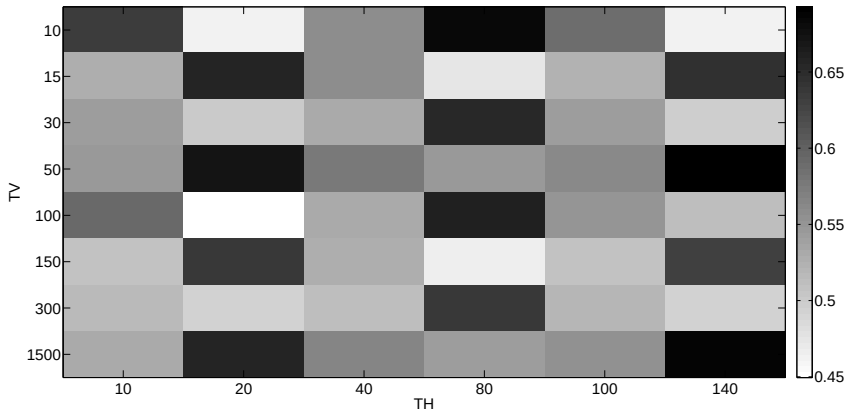

Figure 6: *RRME results keeping fixed U_{m_o} = 40 traces and varying the parameters T_V, T_H to measure the influence of the size of the region $\overline{R_{i,j}}$*

Fig. 7 shows the RRME results of the proposed method keeping fixed the optimal parameters T_{V_o} = 100, T_{H_o} = 20 and varying the value U_{m_o}

to analyze the importance of the non-neighboring constraint. Results show that non-neighboring constraint is a critical stage because the non-use of the constraint (U_m = 1) implies the highest error. However, RRME results tend to improve increasing the spatial separation of the region until the optimal value U_{m_o} = 40. This fact indicates that regions of size (T_{V_o}, T_{H_o}): (i) mainly composed of horizontal background noise often show similar patterns of horizontal noise separated approximately U_{m_o} traces; (ii) mainly composed of anisotropies are sufficiently dissimilar to remove parts of anisotropies belonging to regions separated approximately U_{m_o} traces. This fact implies that it is unlikely to compare the same anisotropy between regions separated approximately U_{m_o} traces at the same depth because the energy of each anisotropy depends highly on its geometry and localization. Finally, RRME results tend to get worse increasing the value $U_{m_o} > 40$ because this spatial separation implies high dissimilarity between noise regions.

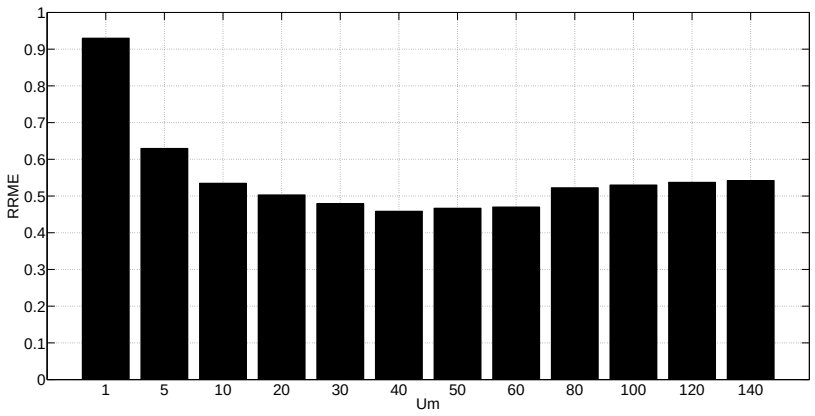

Figure 7: *RRME results keeping fixed T_{V_o} = 100, T_{H_o} = 20 and varying the parameter U_m to analyze the influence of the non-neighboring constraint*

3.1.5 Performance evaluation

It is not fair to objectively compare the performance from the development database, because the parameters (T_V, T_H and U_m) of the proposed method has been optimized using the development set. For this reason, RRME results, calculated for each file of the test database and averaged for each type of noise, are shown in Fig. 8 comparing the proposed method, using the optimal parameters T_{V_o}-T_{H_o}-U_{m_o} obtained in the previous section, and

the other state-of-the-art methods.

In general, the noise removal performance of the methods evaluated are similar both Fig. 8(a) and Fig. 8(b). In Fig. 8(a) in which the type of noise exhibits constant amplitude along the traces, the method DTVM shows the highest performance in the average RRME values, however, the proposed method is ranked in the second position being its performance similar to the BMS method. An example in the removal of this type of noise can be observed in Fig. 9 and Fig. 10. In this example, BMS removes most of the region of the peak (located at 0.3 m of depth and 1.1 m of distance) of the hyperbola related to the localization of the anisotropy. However, the proposed method remains unchanged most of the energy of the peak of the hyperbola. ATS provides a smearing effect near the left edge of the peak of the hyperbola and a high amount of energy of the peak has been attenuated. Although DTVM provides the best quality, it can be observed that higher energy located in the peak of the hyperbola is obtained by the proposed method. With the exception of ATS, the remainder methods show competitive results and high quality of the estimated noise-free radargram taking into account the type of noise N_A.

In Fig. 8(b) in which the type of noise presents variable amplitude along the traces, the method DTVM still shows the highest performance in the average RRME values for type of noise N_B. Nevertheless, the method BMS shows a slightly improvement compared to the proposed method. However, the percentage of improvement of the method DTVM compared to BMS and the proposed method is lower testing this type of noise N_B.

A change in the trend of the performance of the proposed method and the state-of-the-art methods is observed evaluating not purely horizontal noises in Fig. 8(c) and Fig. 8(d). In both figures, the proposed method obtains the best performance in RRME results evaluating the estimated noise-free radargram. BMS and DTVM are ranked in the second and third position respectively, and ATS is ranked in the last position. Highlight that only the proposed method and BMS provide satisfactory results evaluating the type of noise N_C and N_D. A new example in the removal of this type of noise N_C can be observed in Fig. 11 and Fig. 12. In Fig. 12, BMS fragments the horizontal noise remaining artifacts in the hyperbola area but it still removes most of the energy regarding to the peak and closer areas to the peak of the hyperbola related to the anisotropy. However, the

proposed method keeps most of the energy of the peak of the hyperbola but removes all the fragments of noise located in the region of interest delimited by the hyperbola from the anisotropy. A new example in the removal of this type of noise N_D can be observed in Fig. 13 and Fig. 14. In Fig. 14, although BMS and the proposed method provides promising results, the proposed method maintains higher details related to the energy from the anisotropies, especially near to the peaks of hyperbolas located at a depth equal to 0.31 m, 0.91 m and 0.98 m. These results suggest that the spatial similarity combined with the non-neighboring constraint add higher robustness to remove not only purely horizontal noise. Note that ATS still provides the worst performance, independently of the type of noise evaluated, because the moving average traces can be affected by outliers or the use of local data.

Considering the overall performance, Fig. 15 reports that the proposed method provides the best performance in the background noise removal averaging all the types of noises previously evaluated. Results indicate that the proposed method and BMS show higher robustness compared to ATS and DTVM. This fact can be confirmed because the proposed method and BMS are able to keep most of the features of the anisotropies removing most of the interference of the noise. Although DTVM achieves the best quality of the estimated radargram removing purely horizontal noise (noise type N_A), DTVM followed by ATS obtain the worst performance evaluating not purely horizontal noise. This fact is due to these methods are not designed to deal with noises that exhibit rapid variations along the traces. Specifically, DTVM is based on horizontal variation and ATS is based on the use of local data, assumptions that are not valid with types of noise that show abrupt changes along the movement of the GPR antenna.

An interesting advantage of the proposed method can be derived from Table 2 using Matlab on a PC with Intel Core i5 CPU of 2.5 GHz and 4 GB of RAM. Results show that the proposed method achieves the lowest computational cost compared to the other state-of-the-art methods. Specifically, the proposed method provides a reduction of a factor equal to 10, 40 and 220 compared to ATS, BMS and DTVM. Therefore, the proposed method can be considered effective and computationally efficient for the task of background removal in GPR data.

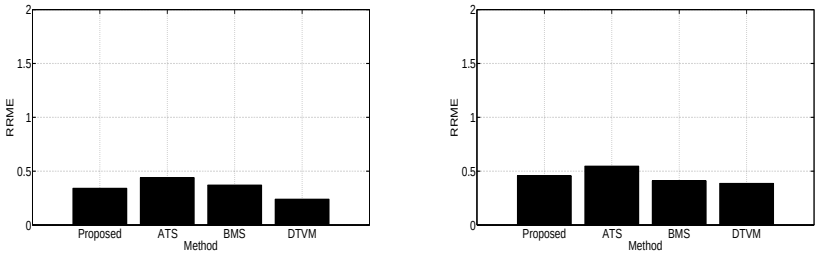

(a) Noise type N_A (b) Proposed (noise estimated)

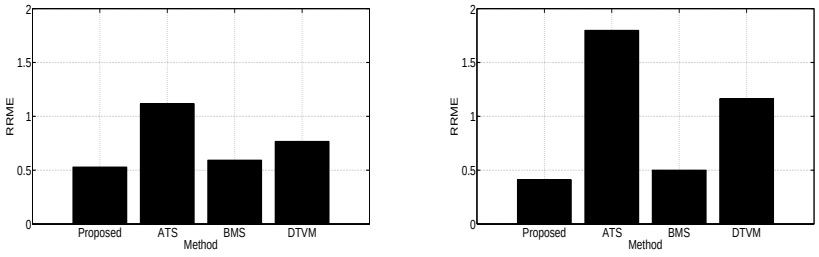

(c) Noise type N_C (d) Noise type N_D

Figure 8: *RRME results, from the test database, evaluating different types of synthetic noises*

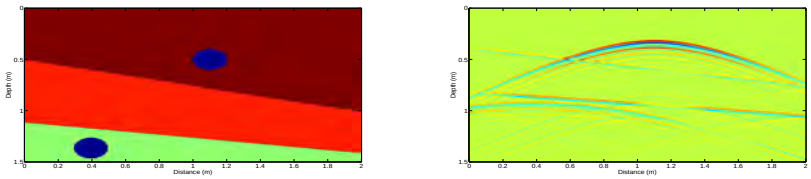

(a) Velocity model, (b) Noise-free synthetic radargram

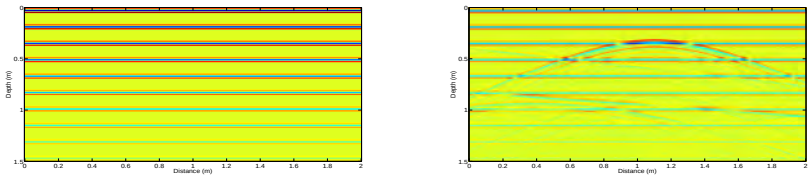

(c) Noise type N_A (d) Mixture

Figure 9: *File F1 (Model M1 and noise N_A) of the test database*

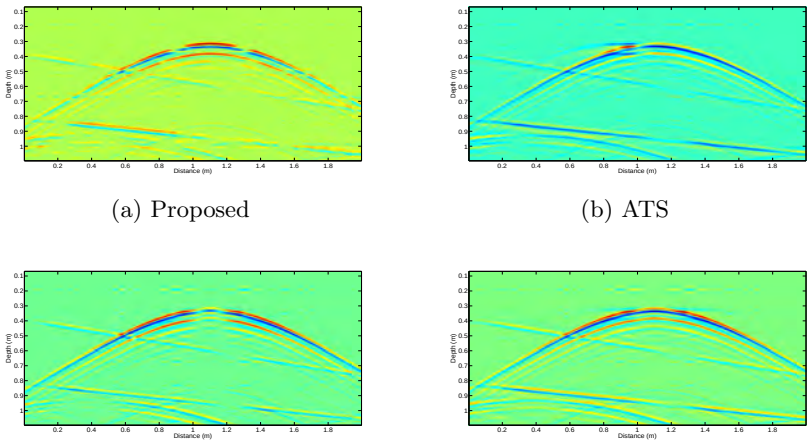

(a) Proposed (b) ATS

(c) BMS (d) DTVM

Figure 10: *Output of the proposed method and the state-of-the-art methods evaluating the file F1 of the test database (noise type N_A). A zoom-image of the output has been performed in order to better observe the details near of the main anisotropies.*

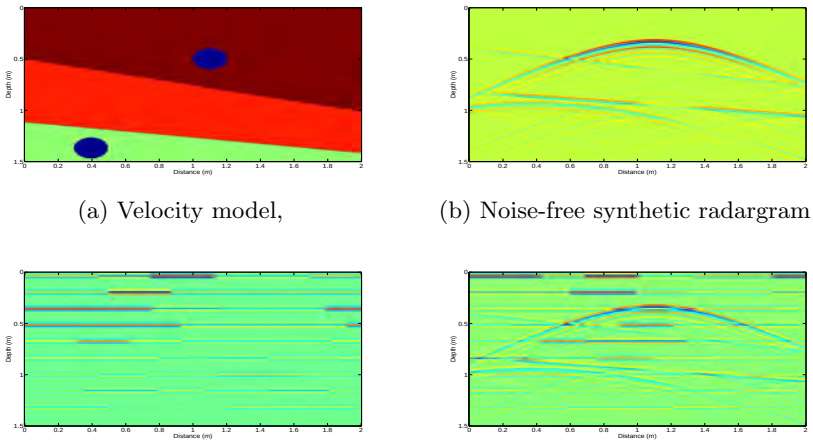

(a) Velocity model, (b) Noise-free synthetic radargram

(c) Noise type N_C (d) Mixture

Figure 11: *File F3 (Model M1 and noise N_C) of the test database*

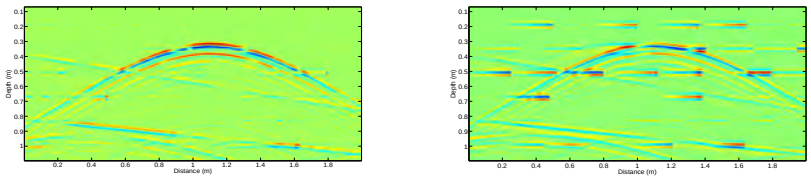

(a) Proposed (b) ATS

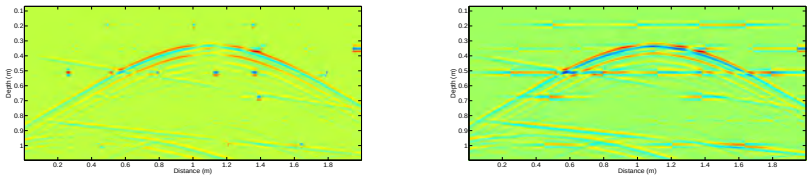

(c) BMS (d) DTVM

Figure 12: *Output of the proposed method and the state-of-the-art methods evaluating the file F3 of the test database (noise type N_C). A zoom-image of the output has been performed in order to better observe the details near of the main anisotropies.*

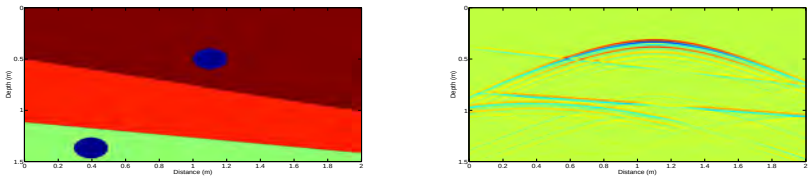

(a) Velocity model, (b) Noise-free synthetic radargram

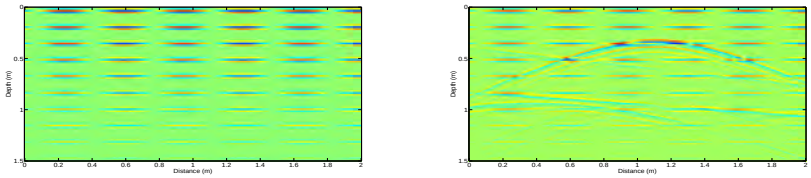

(c) Noise type N_D (d) Mixture

Figure 13: *File F4 (Model M1 and noise N_D) of the test database*

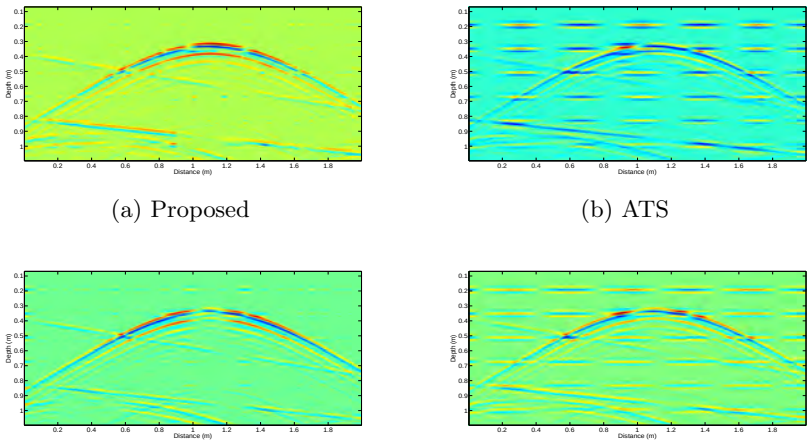

(a) Proposed (b) ATS

(c) BMS (d) DTVM

Figure 14: *Output of the proposed method and the state-of-the-art methods evaluating the file F4 of the test database (noise type N_D). A zoom-image of the output has been performed in order to better observe the details near of the main anisotropies.*

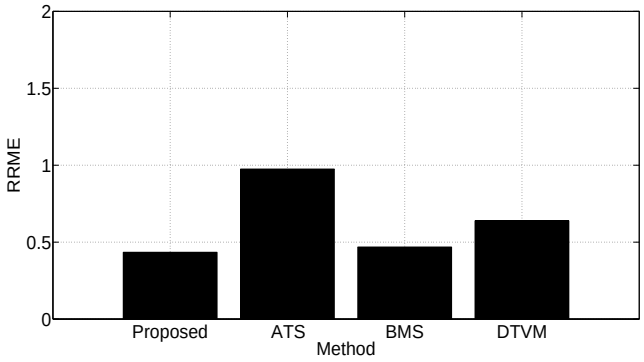

Figure 15: *RRME results, from the test database, averaging the RRME results taking into account all the types of noise evaluated (N_A, N_B, N_C, N_D)*

Table 2: Average computational cost of the proposed method and the other state-of-the-art methods evaluating any file of the synthetic database

	Proposed	ATS	BMS	DTVM
Time (seconds)	1.5	15.2	61.1	328.6

3.2 Field data

3.2.1 Test data

Although evaluation using synthetic data is important for explaining how each background removal method works, it is interesting a new evaluation using real GPR data in order to analyze the improvement obtained in the field data [23] [24]. For this reason, a set of three real GPR data are tested according to Table 3.

Table 3: Characteristics of the real GPR data

Identifier	Material	Type	Place of the quarry	Distance	Depth
P1	Negro Calatorao	Block	Calatorao (Zaragoza, Spain)	1.9 m	1.3 m
P2	Blanco Macael	Quarry face	Macael (Almería, Spain)	11.0 m	5.1 m
P3	Crema Marfil	Block	Pinoso (Alicante, Spain)	2.1 m	1.8 m

3.2.2 Performance evaluation

Three GPR profiles (Table 3) obtained from field data are used to evaluate the proposed method where the results are compared to those of the state-of-the-art methods previously mentioned. Due to the fact that it is not possible to have the free-noise radargram in a real scenario, the comparison of the results of real GPR data is based on visual inspection [23]. The data of the profiles previously mentioned has been collected using a Pro-Ex model RAMAC/GPR system manufactured by MALA GeoScience [27].

The first real GPR data, identified as P1, is obtained from a limestone block, commercially known by its Spanish name *Negro Calatorao*, in Calatorao (Zaragoza, Spain) shown in Fig. 16. The data are collected using a 1.6 GHz antenna. A time window of 45.5 ns has been selected. The analysis is performed using a sampling rate of 733 samples per trace and 475 scans using a distance interval of 0.004 m. Highlight that the removal of the horizontal noise in blocks of *Negro Calatorao* is very relevant and attractive in the stone industry because it is well-known that this material is composed of a layered structure whose laminations severely complicates the detection of anisotropies. The input radargram (Fig. 16) can be labelled as a high quality block because no anisotropies are observed inside it (it was experimentally confirmed after the cutting process) and only the horizontal noise

can be noticed at a depth from 0.02 m to 0.07 m. Comparing Fig. 17(a), Fig. 17(c), Fig. 18(a) and Fig. 18(c), it is shown that the best quality of the estimated free-noise radargram is obtained by the proposed method since it is the only method that removes most of the noise providing satisfactory results. Moreover, the proposed method is the only method that model correctly the irregular pattern of noise (Fig. 17(b)) since the rest of the methods extract a noise pattern more horizontal that the original noise. As occurs in the synthetic data, ATS obtains the worst performance and DTVM is slightly outperformed by BMS that model a less horizontal noise compared to DTVM. The poor performance of background noise removal can be due to the high dependence of local data in the case of ATS and to be designed to deal with purely horizontal noise in the case of BMS and DTVM.

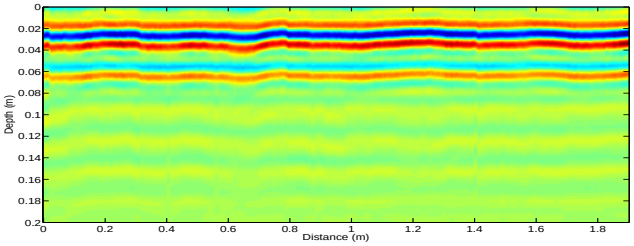

Figure 16: *A zoom-image, in depth, of the radargram of the file P1 (Table 3) has been performed in order to better observe the details of the horizontal noise*

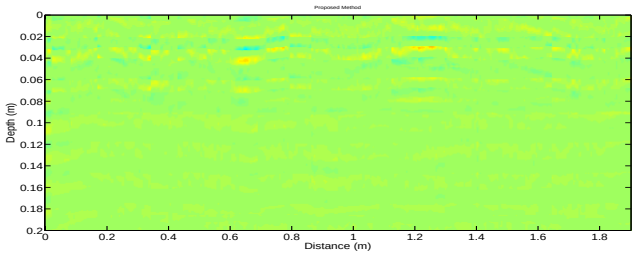

(a) Proposed (free-noise estimated)

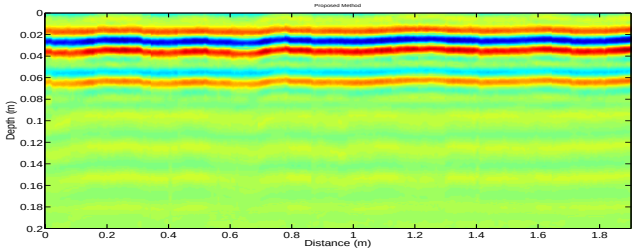

(b) Proposed (noise estimated)

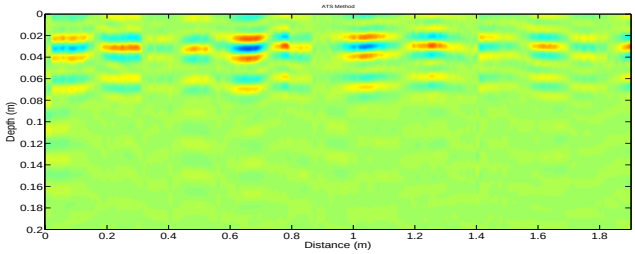

(c) ATS (free-noise estimated)

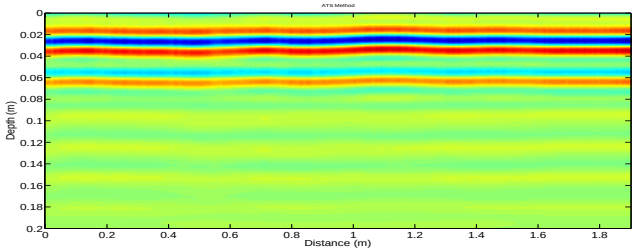

(d) ATS (noise estimated)

Figure 17: *Outputs of the background removal methods when the file P1 is evaluated. (a,b) Proposed, (c,d) ATS*

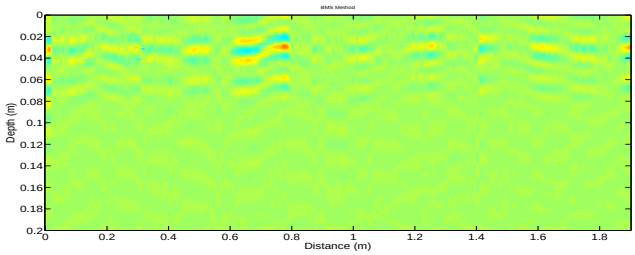

(a) BMS (free-noise estimated)

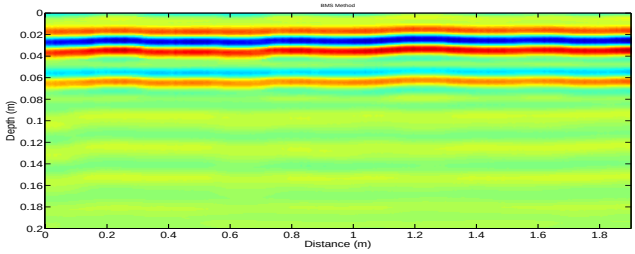

(b) BMS (noise estimated)

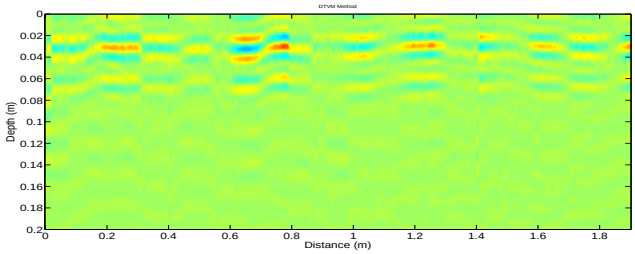

(c) DTVM (free-noise estimated)

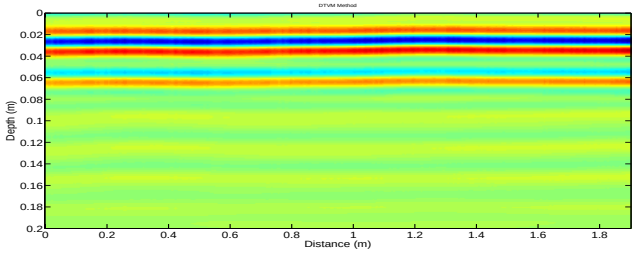

(d) DTVM (noise estimated)

Figure 18: *Outputs of the background removal methods when the file P1 is evaluated. (a,b) BMS and (c,d) DTVM*

The second real GPR data, identified as P2, is collected from a quarry of limestone, known by *Blanco Macael*, in Macael (Almería, Spain) by means of a 250 MHz antenna. The data are obtained in time mode using a time

window of 119.5 ns, a sampling rate of 312 samples per trace and 1571 scans with a distance interval of 0.007 m. Due to low-frequency antennas provide greater penetration depth and less resolution than high-frequency antennas, a 250 MHz antenna has been used to investigate the quarry face because the greater investigation depth was observed for the 250 MHz antenna, which reached more than 5 m. The input radargram (Fig. 19) can be labelled as a medium quality block because an anisotropy (a subvertical cavity experimentally confirmed after the cutting process) is detected approximately at a depth of 1.4 m and a distance of 8.5 m by the presence of hyperbola. In this case, the horizontal noise can be detected at a depth from 0.5 m to 1.0 m. Results show that the best quality of the estimated noise-free radargram is obtained by the proposed method as can be observed in Fig. 20(a). Comparing the results provided by the state-of-the-art method in Fig. 20 and Fig. 21, the promising performance of the proposed method is due to the capability of removing most of the horizontal noise maintaining most of the features of the previous anisotropy and high amplitude contrast with the background. This fact is confirmed in Fig. 20(a) where the hyperbola edges can be clearly observed. However, this promising behavior does not occur in the rest of the compared methods. Specifically, ATS attenuates a great percentage of horizontal noise at the expense of removing a high portion of the region of interest defined by the hyperbola related to the anisotropy (Fig. 20(d)). The method BMS shows the worst performance because the estimated noise-free radargram is approximately empty since BMS removes all the noise including the energy related to the anisotropies (Fig. 21(a,b)). Although DTVM works better than BMS, BMS and DTVM cannot remove the horizontal noise active at the beginning of the radargram, considering a distance from 0 m to 0.8 m, because this noise exhibits a horizontal pattern highly discontinuous. Unlike the proposed method, the estimated noise radargram processed by ATS, BMS and DTVM draw a smoother noise along the distance than the original noise and the energy of the estimated noise is still mixed with significant energy from anisotropies.

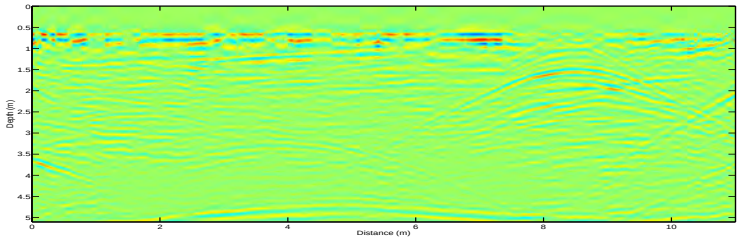

Figure 19: *Radargram of the file P2 (Table 3)*

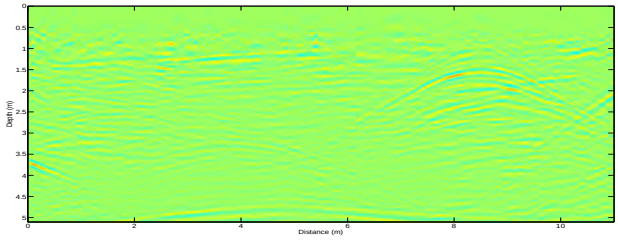

(a) Proposed (free-noise estimated)

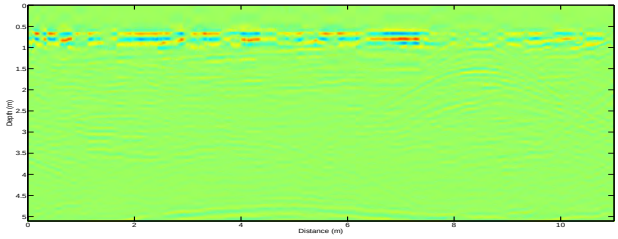

(b) Proposed (noise estimated)

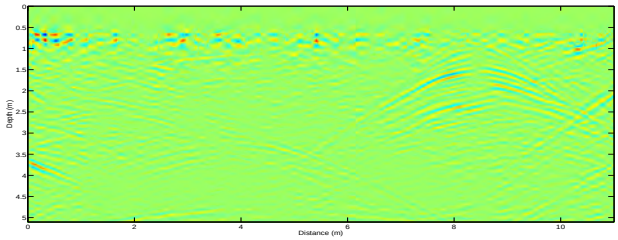

(c) ATS (free-noise estimated)

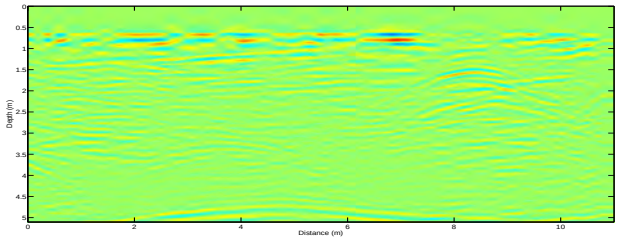

(d) ATS (noise estimated)

Figure 20: *Outputs of the background removal methods when the file P2 is evaluated. (a,b) Proposed, (c,d) ATS*

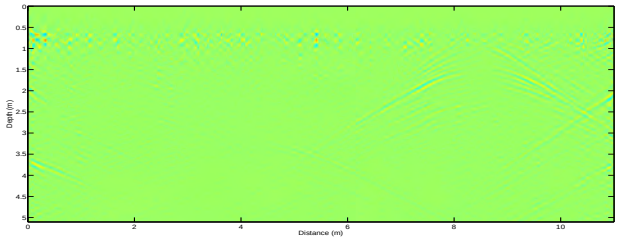

(a) BMS (free-noise estimated)

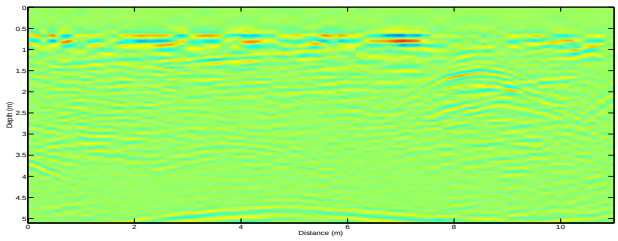

(b) BMS (noise estimated)

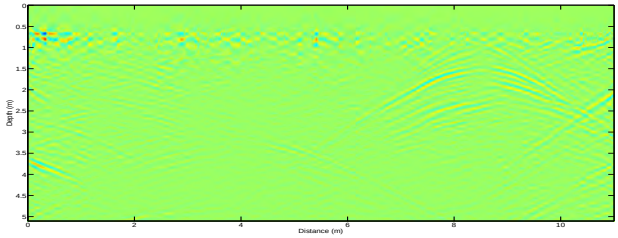

(c) DTVM (free-noise estimated)

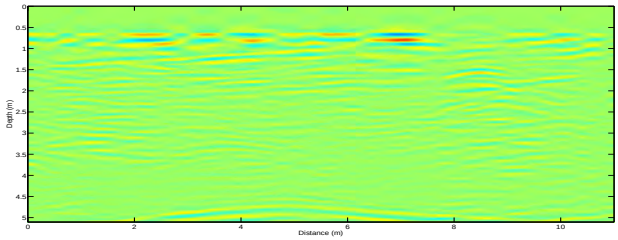

(d) DTVM (noise estimated)

Figure 21: *Outputs of the background removal methods when the file P2 is evaluated. (a,b) BMS and (c,d) DTVM*

The third real GPR data, identified as P3, is collected from a limestone block, commercially known by its Spanish name *Crema Marfil* in Pinoso (Alicante, Spain). The data are obtained using a 800 MHz antenna, a

time window of 36.16 ns, a sampling rate of 288 samples per trace and 525 scans by means of a distance interval of 0.004 m. The input radargram (Fig. 22) can be labelled as a medium quality block because two remarkable anisotropies are detected (both anisotropies were experimentally confirmed after the cutting process). The first anisotropy is a relevant diagonal fracture from a depth (left-right) of 1.2 m to 0.4 m and the second one is a less relevant diagonal fracture from a depth (left right) of 1.4 m to 0.8 m. The horizontal noise is located between 0.22 m to 0.33 m of depth. Again, the best removal of noise is achieved by the proposed method minimizing the residues of anisotropies active in the estimated noise radargram (Fig. 23(b)). Highlight that the proposed method is the only method that is able to separate the energy emitted from a set of small fractures or holes at a depth of approximately 0.4 m in the first half of the block (Fig. 23(a)). In this case, DTVM presents the second best quality of the estimated noise-free radargram outperforms the performance of the method BMS comparing Fig. 24(a) and Fig. 24(c). Following a similar behaviour as in the previous file, BMS shows the worst performance because the estimated noise-free radargram is approximately empty since BMS removes all the noise including the energy related to the anisotropies. Although ATS and BMS help to clean significant amount of unwanted energy from the original noise, both of them also remove high amplitudes of a portion, located from a depth of 0.7m and a distance of 0.6m, of the first diagonal fracture. However, this fact does not occur taking account DTVM or the proposed method. Finally, the superiority of the proposed method over ATS, BMS and DTVM is clear in this field GPR dataset.

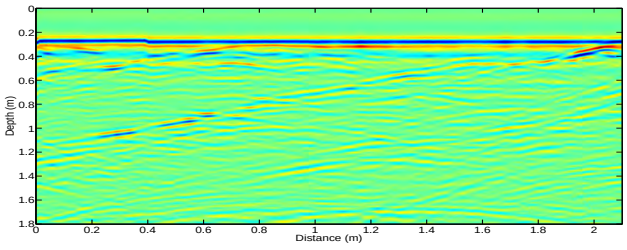

Figure 22: *Radargram of the file P3 (Table 3)*

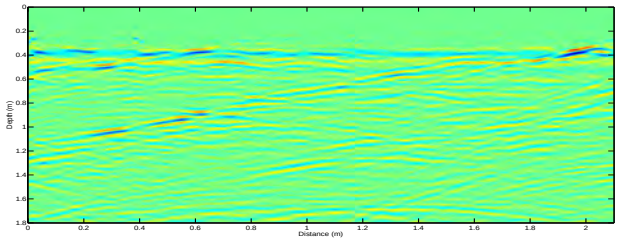

(a) Proposed (free-noise estimated)

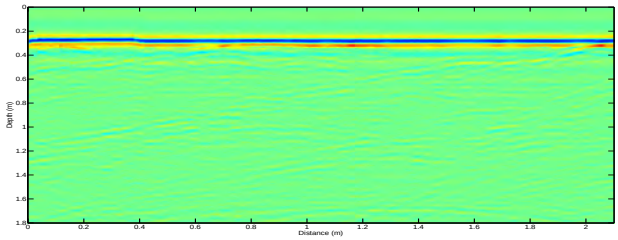

(b) Proposed (noise estimated)

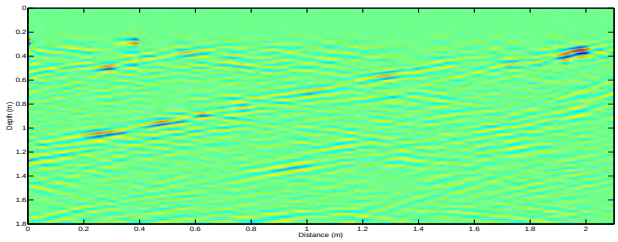

(c) ATS (free-noise estimated)

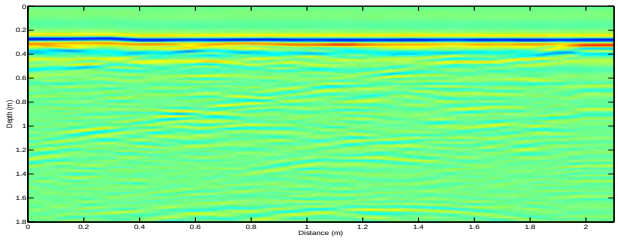

(d) ATS (noise estimated)

Figure 23: *Outputs of the background removal methods when the file P3 is evaluated. (a,b) Proposed, (c,d) ATS*

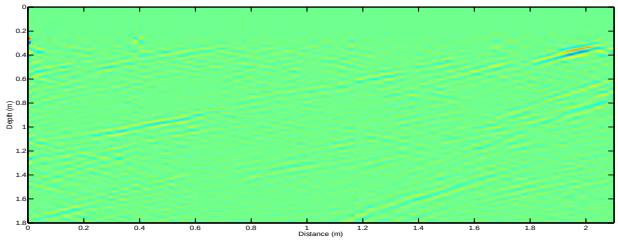

(a) BMS (free-noise estimated)

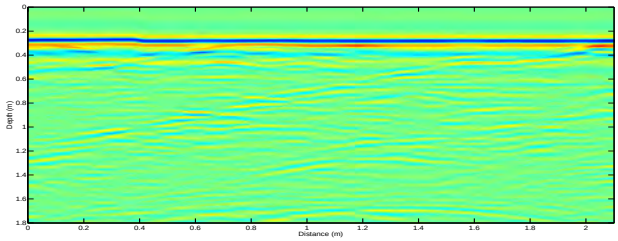

(b) BMS (noise estimated)

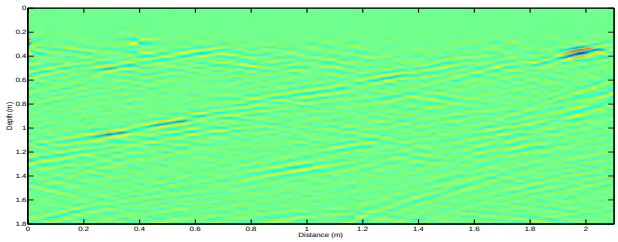

(c) DTVM (free-noise estimated)

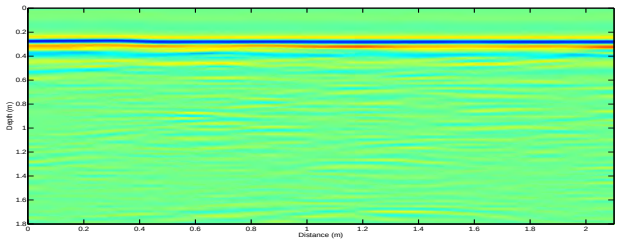

(d) DTVM (noise estimated)

Figure 24: *Outputs of the background removal methods when the file P3 is evaluated. (a,b) BMS and (c,d) DTVM*

4 Conclusions & Future work

This work proposes a background removal method to be applied in GPR data. The idea behind the proposed method is to exploit the feature of repeatability shown by this type of noise in the direction of the movement of the antenna. Specifically, the method attempts to identify repeating regions over the traces at the same depth. In this manner, high values of similarity seem to provide high probability of repetition compared to anisotropies. The local similarity, using neighboring regions, provide satisfactory results evaluating regions only composed of noise. However, the same local similarity does not provide satisfactory results evaluating regions not only composed of noise since the horizontal noise is also characterized by a repetitive pattern not neighboring along the traces. To overcome this problem, the identification of similar regions is combined using a non-neighboring constraint.

The optimization procedure of the proposed method indicates that the use of the non-neighboring constraint minimizes the residues of the noise in the estimated free-noise radargram. Evaluation on synthetic data reports that the proposed method is a competitive method testing different types of noise. Further, the proposed method exhibits higher robustness taking into account all types of synthetic noise evaluated and compared to the state-of-the-art methods used. Evaluation on real data indicates that the proposed method outperforms the background removal performance of ATS, BMS and DTVM. Specifically, the proposed method is able to model a more accurate pattern of GPR background noise compared to BMS and DTVM. Evaluation suggests that BMS and DTVM tend to smooth to a large extent the horizontal variation of the noise because they have been designed to deal with purely horizontal noise. Results indicate that the proposed method is a promising tool to remove the horizontal noise even in blocks of stone composed of a layered structure, e.g., *Negro Calatorao*, in which laminations make difficult the detection of anisotropies analyzing this type of materials. Finally, an additional advantage of the proposed method is its computational efficiency compared to the state-of-the-art methods evaluated.

Our future work will focus on modeling and incorporating temporal or spectral features into an unsupervised or semi-supervised approach in order to extract different types of GPR background noise.

Acknowledgment

The authors would like to thank Dr. Mohamed Rashed and Dr. Essam Rashed for sharing their background removal codes of the methods BMS and DTVM respectively, in order to evaluate the proposed method. The authors are grateful to the Advanced Technology Center (CTAP) for Stone in Macael (Almería, Spain) for their support during data acquisition and evaluation of the final results. This work was carried out using funds provided by Government of Andalusia under the project P11-TIC-7278.

References

[1] Daniels, D., *Ground penetrating radar*. Institution of Electrical Engineers, 2nd ed., 2004.

[2] Orlando, L., "Using gpr to monitor cracks in a historical building," in *4th International Workshop on Advanced Ground Penetrating Radar*, pp. 45–48, 2007.

[3] Gonzalez, M., Catapano, I., Soldovieri, F., "A comparative study of gpr reconstruction approaches for landmine detection," *IEEE Journal of Selected Topics in Applied Earth Observations and Remote Sensing*, vol. 7, no. 12, pp. 4869–4878, 2014.

[4] S. Kadioglu, "Photographing layer thicknesses and discontinuities in a marble quarry with 3D GPR visualisation," *Journal of Applied Geophysics*, vol. 64, no. 3-4, pp. 109–114, 2008.

[5] Arosio, D., Munda, S., Zanzi, L., Porto, F. and Mosele, F., "Nondestructive Quality Control of Reinforced Masonry Buildings," *Journal of Infrastructure Systems. Special Issue: Nondestructive Testing in Civil Engineering*, vol. 18, no. 1, pp. 34–46, 2012.

[6] Rey, J., Martinez, J., Vera, P., Ruiz, N., Canadas, F. and Montiel, V., "Ground-penetrating radar method used for the characterisation of ornamental stone quarries," *Construction and Building Materials*, vol. 77, pp. 439–447, 2015.

[7] Solimene, R., Cuccaro, A., Dell'Aversano, A., Catapano, I. and Soldovieri, F., "Ground Clutter Removal in GPR Surveys," *IEEE Journal of Selected Topics in Applied Earth Observations and Remote Sensing*, vol. 7, no. 3, pp. 792–798, 2014.

[8] U. Khan, "Background removal from GPR data using Eigenvalues," in *13th International Conference on Ground Penetrating Radar (GPR)*, (Lecce), pp. 1–5, 2010.

[9] Vuksanovic, B., Bostanudin, N., Hidzir, H. and Parchizadeh, H., "Discarding Unwanted Features from GPR Images Using 2DPCA and ICA Techniques," *International Journal of Information and Electronics Engineering*, vol. 3, no. 3, pp. 317–323, 2013.

[10] D. Nobes, "Geophysical surveys of burial sites: a case study of Oaro urupa," *Geophysics*, vol. 64, pp. 357–367, 1999.

[11] Der Merwe, A. and Gupta, I., "A novel signal processing technique for clutter reduction in GPR measurements of small, shallow land mines," *IEEE Transactions on Geoscience and Remote Sensing*, vol. 38, no. 6, pp. 2627–2637, 2000.

[12] Young, R. and Sun, J., "Revealing stratigraphy in ground penetrating radar data using domain filtering," *Geophysics*, vol. 64, pp. 435–442, 1999.

[13] Zoubir, A., Chant, I., Brown, C., Barkat, B. and Abeynayake, C., "Signal processing techniques for landmine detection using impulse ground penetrating radar," *IEEE on Sensors Journal*, vol. 2, pp. 41–51, 2002.

[14] Potin, D., Duflos, E. and Vanheeghe, P., "Landmines ground-penetrating radar signal enhancement by digital filtering," *IEEE Transactions on Geoscience and Remote Sensing*, vol. 44, pp. 2393–2406, 2006.

[15] Abujarad, F., Jostingmeier, A., "Clutter removal for landmine using different signal processing techniques," in *Tenth International Conference on Ground Penetrating Radar*, pp. 697–700, 2004.

[16] Jeng Y., Lin C., Li Y., Chen C. and Huang, H., "Application of multiresolution analysis in removing ground penetrating radar noise," in

CSPG CSEG CWLS Convention, (Calgary, Canada), pp. 416–419, 2009.

[17] G. Nadim, "Clutter reduction and detection of landmine objects in ground penetrating radar data using likelihood method," in *Third International Symposium on Communications, Control and Signal Processing*, pp. 98–106, 2008.

[18] Zhao, A., Jiang, Y., and Wang, W., "Exploring Independent Component Analysis for GPR Signal Processing," in *Electromagnetics Research Symposium*, (Hangzhou, China), pp. 1–4, 2005.

[19] Xia, J., Franseen, E., Miller R., Weis T. and Byrnes, A., "Improving ground-penetrating radar data in sedimentary rocks using deterministic deconvolution," *Journal of Applied Geophysics*, vol. 54, pp. 15–33, 2003.

[20] Cagnoli, B., and Ulrych, T., "Singular value decomposition and wavy reflections in ground-penetrating radar images of base surge deposits," *Journal of Applied Geophysics*, vol. 48, pp. 175–182, 2001.

[21] Kim, J., Cho, S., Yi, M., "Removal of ringing noise in GPR data by signal processing," *Geosciences Journal*, vol. 11, no. 1, pp. 75–81, 2007.

[22] Y. Shkolnikov, "Weighted principal component analysis for real-time background removal in GPR data," in *Proc. SPIE 8357, Detection and Sensing of Mines, Explosive Objects, and Obscured Targets XVII*, 2012.

[23] Rashed, M. and Harbi, H., "Background matrix subtraction (BMS): A novel background removal algorithm for GPR data," *Journal of Applied Geophysics*, vol. 106, pp. 154–163, 2014.

[24] E. Rashed, "GPR background removal using a directional total variation minimisation approach," *Journal of Geophysics and Engineering*, vol. 12, no. 6, pp. 897–908, 2015.

[25] "Sandmeier geophysical research, reflexw software," 2016.

[26] De Domenico, D., Campo D. and Teramo, A., "Fdtd modelling in high-resolution 2d and 3d gpr surveys on a reinforced concrete column in a double wall of hollow bricks," *Near Surface Geophysics*, vol. 11, pp. 29–40, 2013.

[27] “Mala geoscience,” 2016.